Experimental Study of Tandem Mirror Plasmas Controlled by ICRF Waves and DC Fields

Osamu Sakai

1995

Experimental Study of Tandem Mirror Plasmas Controlled by ICRF Waves and DC Fields

Osamu Sakai

1995

Contents

Chapter 1

Introduction

1.1 Fusion-oriented plasma physics

Fusion-oriented plasma physics is a promoter for realization of a fusion reactor to obtain an environmentally-safe energy source. For these four decades a great number of experimental studies have been performed in many magnetic confinement devices as well as theoretical researches [1]. In order to obtain a burning condition, a high-density, high-temperature, and well-confined plasma is necessary, and many aspects of research such as transport, heating, and stability have been investigated. Optimization of device configuration is also a key issue for a fusion reactor; various kinds of devices such as tokamaks, stellarators, reversed field pinches, field reverse configurations, tandem mirrors, and so forth, have been examined so far. One of the main results from the researches in magnetic confinement devices is significant amount of energy output from Deuterium-Tritium (D-T) reactions in the Joint European Tokamak (JET) and the Tokamak Fusion Test Reactor (TFTR) [2, 3].

Because of prediction and discovery of its good properties, experimental and theoretical studies of a high-density and high-temperature magnetized plasma have been concentrated on researches of a tokamak. However, a tokamak is inherently operated in a pulse discharge, and scenario of its steady state operation has not been well established.

A fusion reactor in other types is another candidate to avoid such inevitable disadvantages of tokamaks. Among them a mirror device has a linear configuration with its simple structure, which leads to its promising properties such as sustainment of a high-beta plasma and steady state operation in a future reactor [4]. Neutrons from thermonuclear reactions were detected in the previous mirror experiments [5, 6] as well as in tokamaks. They need only a linear-shaped chamber and a set of magnetic coils for construction of a machine itself, which is a great advantage from the engineering point of view. Experimentally a high-beta plasma was successfully confined in the central cell [4]. Energy output from fusion reaction is readily available using a direct energy convertor at one end of a machine if it is carried by charged particles such as protons. However, such a configuration also results in difficulties in magnetohydrodynamic stabilization and enhancement of axial confinement, and not only these problems but also other fundamental plasma behavior have not been well resolved. A mirror device, which has such a significant potential for a fusion reactor, can be a good target of fundamental researches of a completely-ionized plasma.

These researches in mirrors are also connected to phenomena in other types of machines. For instance, axial confinement in mirrors has a number of common features to scrape-off layer (SOL) transport in divertor configuration in a tokamak [7–9]. A experimental mirror device has an end plate with tangential injection of the static magnetic field lines. This configuration resembles the situation of a divertor plate in a torus device. There has been a proposal that end plugging in a magnetic cusp device is applicable to control of heat flux to a divertor plate [8]. Another method for that control is "thermal dike", in which radiofrequency (RF) waves play a role on reduction of heat transport towards a divertor plate [10]. This concept is now investigated in the GAMMA 10 tandem mirror using the region in front of the end plate [9].

Another good example of the research in which collaboration with other types of machines will be important is transport study across the magnetic field lines. Particularly reduction of anomalous losses is an inevitable factor for realization of any kinds of magnetic fusion, i.e., not only tokamaks but also stellarators, tandem mirrors, and other torus and linear devices, since radial confinement time in such machines is by one or two orders smaller than a value predicted from the classical theory [11]. From this point of view the discovery of high confinement mode (H mode) in the Axially Symmetric Divertor Experiment (ASDEX) tokamak [12] was a significant trigger for promotion of researches on radial energy and particle confinement. Unfortunately there has been a misunderstanding for almost one decade that H mode is a phenomenon that can be realized only in tokamaks, although related results from other types of machines have been reported so far. Study on H-mode physics in a non-tokamak device may contribute to its understanding rather than that in a tokamak in order to extract an essential point. Plasma physics for fusion is such a huge science that organized collection of experimental and theoretical results in all kinds of machines will lead to a smoother progress for the fusion research.

Besides the prospects as an alternative fusion reactor, there has been a proposal to use a mirror device as a neutron source for material testing [4, 13]. Materials on the first wall and of the divertor plate in a D-T reactor will be exposed to a large number of high-energy neutrons, and a compact and efficient neutron source is desirable for development of a new material that can be stable in such a severe environment. A mirror device is suitable to this usage due to its simple configuration and its inherent high-beta operation. That is, the research on mirror devices has an urgent driving force to realization of a neutron source, which will be the first step of its development. After construction and data accumulation as a neutron source for the first generation reactor, which may be a D-T tokamak reactor, a mirror device will become one of the closest systems to the second generation reactor,

which will utilize a deuterium-deuterium (D-D) or deuterium-^{3}He (D-^{3}He) reaction that can be realized only in a high-beta machine.

Another important contribution of this kind of research is a driving force of progress in studies on weakly-ionized plasmas [14]. That kind of plasma has been widely used in material science such as thin film deposition and dry etching process. A number of techniques developed in fusion-oriented plasma physics have been already and successfully adapted; plasma production by electron cyclotron resonance (ECR) [14] and helicon wave propagation [15, 16], and various kinds of measurement methods for plasma parameters [17]. In order to get more understanding of general plasma physics, researches of completely-ionized plasmas for fusion are of importance because of its long history and its potential on application to other fields.

1.2 Overview of researches in mirror devices

As mentioned in Sec. 1.1, mirror devices have disadvantages as well as advantages due to its linear configuration. One of the well-known disadvantages is its inherently poor axial confinement as a result of open field lines. A simple mirror device confines a plasma due to its inhomogeneity of the strength of magnetic field, although its ability of confinement is quite low since there is a loss region in the velocity space, which is called "loss cone" Concept of tandem mirror with axial potential formation was proposed by Dimov *et al.* [18] and Baldwin *et al.* [19], and potential formation by neutral beam injection (NBI) and electron cyclotron resonance heating (ECRH) was experimentally investigated in the TMX-U and GAMMA 10 tandem mirrors [20, 21]. Sloshing ion distribution for ion-confining potential with thermal barrier was examined, and plug ECRH experiment with high input power indicated that plateau distribution in the plug electron velocity space was essential to form the observed ion-confining potential [22], which was predicted from

the strong ECRH theory [23]. On the other hand, potential formation along the magnetic field lines was performed in the Phaedrus, TARA, and HIEI tandem mirrors, by ion cyclotron range of frequencies (ICRF) waves [24–28], which is more convenient in terms of accessibility towards a reactor with remote transmission, with simple system of power generation, and with confirmed techniques for high power supply. Hershkowitz *et al.* revealed in the Phaedrus experiments that ion confining potential was created by the RF axial electric field in the near-field region of the ICRH antenna [24], and that magnetic moment conservation in the presence of gradient of the magnetic field strength led to potential dips like a thermal barrier [25]. In TARA the electron bounce resonance modified the electron distribution function and created the ion-confining potential [26]. In HIEI, effects of ICRF injection in the plug cell were investigated, and the ion-confining potential with a thermal barrier was successfully formed [27]. The formation of the ion-confining potential was due to electron acceleration by Landau damping of an electrostatic wave generated directly from the antenna, and thermal barrier formation and sustainment was attributed to ICRF ponderomotive potential [24] with axial ion pumping. In the recent experiment in HIEI, local electron heating by ICRF waves which encountered the ion-ion hybrid resonance from the high-field side resulted in a potential hill in the plug cell [28]. That formation mechanism has been clarified in the sequential experiment in HIEI by experimental evidence and theoretical analysis on interaction between a mode-converted electrostatic wave and electrons [29]. The common point of the potential formation by ICRF waves in these three machines is that ion-confining potential cannot be explained with the modified Boltzmann relation [30] with observed electron temperature in the plug cells, and modification of electron velocity space distribution is considered to play an essential role rather than plug electron temperature. Its scaling law with the theoretical prediction has been confirmed in the experiment in HIEI [29]. Efficient plug electron

heating by ICRF waves and incidental potential formation will be discussed in Chap. 3 and Chap. 5, respectively.

Another disadvantage of mirror is the difficulty in magnetohydrodynamic stabilization. Magnetohydrodynamic stability is necessary to be held against the flute mode, which is inherent due to bad curvature of the static magnetic field lines in the central cell of a tandem mirror. Conventional way to remove its instability is to set anchor cells with baseball coils [31]. Inutake *et al.* showed stability criteria of the flute mode experimentally by changing beta ratio between in the central cell and in the anchor cell, and its criteria was in good agreement with the theoretical prediction [32]. However, additional heating is necessary to keep a relatively high beta value in the anchor cells, and its nonaxisymmetry produces neoclassical radial transport. Another way is to utilize RF ponderomotive force by mode control [33–35]. RF stabilization was found to be effective in the frequencies of both the helicon wave propagation [33, 34] and the Alfvén wave propagation [35]. Yasaka *et al.* controlled radial profile of RF electric field using the mode-control technique, which could make it possible to excite a favorable eigenmode to control radial profile of the RF electric field. Such a method induces no additional radial loss, and the scaling law in a small simple mirror showed its possibility for a future mirror reactor [36]. Further experimental verification in a tandem mirror with relatively high beta values [37] has been confirmed in HIEI in the regime of enhanced axial and radial confinement [29], which will be mentioned in Chap. 5.

Central cell ion heating is another problem in a mirror device. NBI heating will break axisymmetry in the central cell plasma and make it less stable. Another method for ion heating is ion cyclotron resonance heating (ICRH). Unlike tokamaks, magnetic field strength changes mainly along magnetic field lines and the accessibility of ICRF waves is different. Slow wave beach heating is readily applicable [38–40], but the slow wave

cannot penetrate into a high-density plasma because of its cut-off density. Roberts *et al.* showed one possibility of its utilization with suggestion that the slow wave was possible to access into a relatively high-density multi-ion-species plasma [41]. Another way to overcome this problem is mode conversion from the fast magnetosonic to the slow ion-cyclotron wave in the longitudinal inhomogeneity, which was theoretically predicted by White *et al.* [42] and by Lashmore-Davies [43]. There have been other theoretical studies dealing with this mode conversion [44–46]. Experimentally change of radial profiles of the RF fields were measured near the mode-conversion point in Phaedrus, although no ion heating was detected [47]. Ion heating via the mode conversion examined in part in the HIEI simple mirror device [48]. In the HIEI tandem mirror, specific wave propagation has been measured, which shows clear feature of mode conversion into the slow wave, and simultaneously minority heating was observed [31, 49]. Such recent results on the mode conversions will be reported in Chap. 3. If a nonaxisymmetric elliptical flux tube is present in a machine, another mode conversion will take place [50], although it is not applicable in an axisymmetric tandem mirror.

As mentioned in Sec. 1.1, once axial confinement is enhanced, improvement of radial confinement in a mirror is an inevitable task as well as in a tokamak and other magnetic confinement systems. One of the good suggestions to solve this problem is understanding of high confinement mode (H mode) phenomena. In H-mode discharges in tokamaks, the following sequential events are observed in general; Auxiliary heating beyond the threshold power produces transition to the phase in which outward particle and heat flux decreases with reduction of edge fluctuations, and consequently particle and energy confinement time increases by a factor of 2–3. The accumulation of experimental results in tokamaks and the extensive efforts on theoretical progress revealed the part of the physics of H mode. Itoh and Itoh [51] predicted the essential role of radial electric field on

H mode, and it was extended by Shaing *et al.* theoretically [52]. In the experiment in the DIII-D tokamak, sheared poloidal rotation and related radial electric field were observed in *H*-mode discharges by auxiliary heating [53], and in the Continuous Current Tokamak (CCT), radial electric field and radial current imposed by an inserted electrode successfully created a *H*-mode-like discharge [54]. Reduction of edge turbulence and sheared radial electric field were linked with theoretical work by Biglari *et al.* [55]

These results on *H*-mode phenomena remind us of the previous experimental observations in other types of devices. In the Heliotron-E device, roles of radial electric field on confinement were examined [56]. The radial electric field changes significantly according to electron density, although no clear relation to the change of confinement predicted from the neoclassical theory was observed. In linear machines, radial electric field was successfully controlled by multi end ring biasing. The end plate biasing experiments in the Q_T-Upgrade machine [57], the GAMMA 10 [58] and Phaedrus [59] tandem mirrors, and the PISCES-A linear plasma device [60] represented that radial electric field with rigid rotation in the quasi-steady state affects micro instabilities and magnetohydrodynamic stability. Drift wave instability in the edge was suppressed in either sigh of radial electric field [58], which was possibly related to tokamak situations in *H* mode. In PISCES-A effects of sheared electric field was examined [60], although no observation of transition phenomenon was reported. Recently *H*-mode-like transition was observed in the W 7-AS [61], the Compact Helical System (CHS) [62], and HIEI [6, 63–65]. These experimental results emphasize that a *H*-mode-like discharge is possible in a currentless torus plasma or in a mirror (linear machine) plasma if a significant sheared rotation to suppress edge turbulence is created by any means. We note that this discharge observed in HIEI, in which a limiter in the central cell is DC-biased, differs from the previous results in other mirror or linear machine in the following points: (1) the observation of bifurcated states

between high and low confinement regimes, and (2) the presence of sheared rotation. Such results will be discussed in detail in Chap. 4.

Conventional concept of a tandem mirror was realized in GAMMA 10 and TMX-U; they are equipped with baseball coils for magnetohydrodynamic stabilization, NBI for formation of sloshing ion distribution, and ECRH for plug electron heating. Their necessities result from the physical demands for the operation of a mirror device. From the engineering point of view, however, they make the whole system rather complicated. Here an alternative scheme is taken into consideration: "ICRF tandem mirror", which is the main focusing point in this study. With elaborate combinations of each ICRF wave, a tandem mirror sustained by ICRF waves may be operated, preserving its simplicity in both configuration and system. That is, when we take a look at the above problems in a tandem mirror, it is readily found that ICRF wave can play quite large roles in mirror operation, i.e., magnetohydrodynamic stabilization, axial confinement, and ion heating. Plasma production in the upper side of ICRF wave, i.e., the helicon wave [15, 16, 66], is also possible in a mirror device. Furthermore, sheared rotation for trigger of *H*-mode-like behavior might be induced by ICRF waves [67, 68]. (However this will be verified in experiments in the future since mechanism of radial transport itself has not been confirmed in its fundamental physics and DC biasing on metal exposed to a plasma is still reliable to control a radial potential profile.) Such schemes of plasma control are possible because of the specific features of an ICRF wave; It is resonant with ions by cyclotron resonance, it can be also resonant with electrons in the condition of their thermal velocity comparable to the wave phase speed, and it has a wave length comparable to or less than device characteristic length. The whole system of a tandem mirror becomes quite simple due to usage of only one kind of RF without anchor cells. More experimental verification of ICRF tandem mirror is expected to measure the feasibility of its reactor. At the same time,

such an experimental study will contribute to more understanding of general magnetic confinement system, especially on radial transport, which is also the important focusing point of this study.

1.3 Goal of this study

The following subjects will be discussed from the next chapter. The goal of this study is summarized by the word of "driving force to a further progress on ICRF mirror confinement system as well as on related general plasma phenomena" Properties of ICRF-interacted and DC-biased plasmas are investigated in the HIEI tandem mirror. In the physical phenomenology, this study deals with a magnetoplasma with longitudinal inhomogeneity and with controlled two-dimensional potential profiles.

In Chap. 2, theoretical background for heating and confinement with propagation of ICRF waves is reviewed. First, dispersion relation of ICRF waves is presented, and various kinds of interaction with ions and electrons are introduced. Second, in addition to radial confinement, which includes a common physics to other magnetic confinement systems, axial confinement, which is a main loss channel in a linear device with open field lines, is discussed in terms of utilization of ICRF-induced potential. The scenario of an axisymmetric mirror operation by ICRF waves and DC fields is presented.

From Chap. 3, experimental results of this study are demonstrated with theoretical analysis. Chapter 3 represents mode conversions of ICRF waves with incidental ion and electron heating [28, 31, 49]. Axial inhomogeneity of the strength of the static magnetic field causes mode conversions in a two-ion-species plasma. In the case of the low-field side launching, the fast magnetosonic wave, which can propagate in a high-density plasma, converts into the slow ion-cyclotron wave at the ion-ion hybrid resonance layer. This mode conversion provides efficient minority ion heating in the central cell of a mirror

device. On the other hand, the high-field side incidence of the fast wave results in mode conversion to an electrostatic wave with incidental electron heating and velocity space diffusion.

Chapter 4 deals with improvement of radial confinement through *H*-mode-like transition [6, 63–65]. DC limiter biasing produces high radial confinement mode with reduction of edge turbulence and with formation of sheared plasma rotation. The high confinement mode emerges from bifurcated transition represented by sudden drop of atomic line emission and hysteresis in edge plasma parameters. Mechanism of transition is discussed with a model from azimuthal momentum balance affected by shear stabilization in the radial edge region.

In Chap. 5, concept of "ICRF tandem mirror" is expressed with experimental verification [6, 29, 37]. Axial confinement by ICRF-induced potential is investigated and possible mechanism of electron heating in the plug cell is discussed in the case of the high-field side incidence of the fast wave. Simultaneous application of DC limiter biasing and two mode conversions for ion heating and axial potential formation leads to high-beta operation, in which stability high-beta plasma is within the criteria supported by RF ponderomotive force. Estimation of simultaneous enhancement axial and radial confinement is shown, where it includes the effects of two-dimensional potential profiles.

Finally, in Chap. 6, this work will be summarized as a conclusion.

References

[1] For example, Anniversary Issue in Nucl. Fusion **30** (1990) Vol. 9.

[2] JET Team, Nucl. Fusion **32** (1992) 187.

[3] J. D. Strachan *et al.* (TFTR Team), Phys. Rev. Lett. **72** (1994) 3526, R. J. Hawryluk *et al.* (TFTR Team), Phys. Rev. Lett. **72** (1994) 3530.

[4] N. Hershkowitz, S. Miyoshi, and D. D. Ryutov, Nucl. Fusion **30** (1990) 1761.

[5] F. H. Coensgen, W. F Cummins, B. G. Logan, A. W. Molvik, W. E. Nexsen, T. C. Simonen, B. W. Stallard, and W. C. Turner, Phys. Rev. Lett **35** (1975) 1501.

[6] T. Tamano, T. Cho, M. Hirata, H. Hojo, M. Ichimura, M. Inutake, K. Ishii, A. Itakura, I. Katanuma, R. Katsumata, K. Kiwamoto, A. Mase, Y Nagayama, Y. Nakashima, T. Saito, M. Shoji, E. Takahashi, Y Tatematsu, K. Tsuchiya, N. Yamaguchi, K. Yatsu, Y. Yasaka, O. Sakai, K. Iwami, and Y. Ohe, *Plasma Physics and Controlled Nuclear Fusion Research* (IAEA, Vienna, 1995) IAEA-CN-60/C-I-1.

[7] P C. Stangeby and G. M. McCracken, Nucl. Fusion **30** (1990) 1225.

[8] T. Watari, R. Kumazawa, T. Mutoh, T. Seki, K. Nishimura, and F Shimpo, Nucl. Fusion **33** (1993) 1635.

[9] Y Kiwamoto, Y. Tatematsu, T. Saito, I. Katanuma, Y Yoshimura, and T. Tamano, Phys. Plasmas **1** (1994) 3986.

[10] T. Ohkawa, J. Plasma Fusion Res. **64** (1990) 305.

[11] P. C. Liewer, Nucl. Fusion **25** (1985) 543.

[12] F Wagner *et al.* (ASDEX Team), Phys. Rev. Lett. **49** (1982) 1408.

[13] R. F Post and D. D. Ryutov, UCRL-JC-119341 (1995).

[14] R. Wilhelm, Plasma Phys. Control. Fusion **35** (1993) A199.

[15] R. Boswell, Plasma Phys. Control. Fusion **26** (1984) 1147.

[16] Y. Yasaka and Y. Hara, Jpn. J. Appl. Phys. **33** (1994) 5950.

[17] O. Auciello and D. L. Flamm (ed.), *Plasma Diagnostics* (Academic Press, San Diego, 1989).

[18] G. I. Dimov, V V Zakaidakov, and M. E. Kishinevskii, Sov. J. Plasma Phys. **2** (1976) 326.

[19] D. E. Baldwin and B. G. Logan, Phys. Rev. Lett. **43** (1979) 1318.

[20] M. Inutake, T. Cho, M. Ichimura, K. Ishii, A. Itakura, I. Katanuma, Y Kiwamoto, Y. Kusama, A. Mase, S. Miyoshi, Y. Nakashima, T. Saito, A. Sakasai, K. Sawada, I. Wakaida, N. Yamaguchi, and K. Yatsu, Phys. Rev. Lett. **55** (1985) 939.

[21] D. P. Grubb *et al.* (TMX-U Team), Phys. Rev. Lett. **53** (1984) 783.

[22] T. Cho, M. Hirata, K. Ogura, E. Takahashi, T. Kondoh, N. Yamaguchi, K. Masai, K. Hayashi, I. Katanuma, K. Ishii, T. Saito, Y. Kiwamoto, K. Yatsu, and S. Miyoshi, Phys. Rev. Lett. **64** (1990) 1373.

[23] R. H. Cohen, Phys. Fluids **26** (1983) 2774.

[24] N. Hershkowitz, B. A. Nelson, J. Johnson, J. R. Ferron, H. Persing, C. Chan, S. N. Golovato, and J. D. Callen, Phys. Rev. Lett. **55** (1985) 947.

[25] N. Hershkowitz, B. A. Nelson, J. R. Ferron, R. H. Goulding, and E. Wang, Nucl. Fusion **28** (1988) 1333.

[26] D. K. Smith, K. Brau, P Goodrich, J. Irby, M. E. Mauel, B. D. McVey, R. S. Post, E. Sevillano, and J. Sullivan, Phys. Fluids **29** (1986) 902.

[27] Y Yasaka, M. Miyakita, S. Kimoto, H. Takeno, and R. Itatani, *Plasma Physics and Controlled Nuclear Fusion Research* (IAEA, Vienna, 1991) Vol. 2, p. 725.

[28] Y. Yasaka, O. Sakai, H. Takeno, and H. Hojo, Nucl. Fusion **34** (1994) 1263.

[29] O. Sakai, K. Iwami, and Y. Yasaka, submitted to Jpn. J. Appl. Phys.

[30] R. Cohen and I. Bernstein, Nucl. Fusion **20** (1980) 1421.

[31] M. Inutake, T. Tamano, T. Cho, M. Hirata, H. Hojo, M. Ichimura, K. Ishii, A. Itakura, I. Katanuma, K. Kiwamoto, A. Mase, S. Miyoshi, Y. Nakashima, T. Saito, N. Yamaguchi, K. Yatsu, Y. Yasaka, O. Sakai, M. Shima, H. Yoshida, and R. Itatani, *Plasma Physics and Controlled Nuclear Fusion Research* (IAEA, Vienna, 1993) (Proc. 13th Int'l Conf. (Wurzburg, 1992)) Vol. 2, p. 651.

[32] H. Hojo, M. Inutake, M. Ichimura, R. Katsumata, and T. Watanabe, Jpn. J. Appl. Phys. **32** (1993) 2116.

[33] K. Adachi *et al.* (RFC-XX Team), and R. Itatani and Y. Yasaka *Plasma Physics and Controlled Nuclear Fusion Research* (IAEA, Vienna, 1981) Vol. 1, p. 143. M. Inutake *et al.* (GAMMA 6 Team), and R. Itatani and Y. Yasaka *Plasma Physics and Controlled Nuclear Fusion Research* (IAEA, Vienna, 1983) Vol. 1, p. 545.

[34] Y. Yasaka and R. Itatani, Phys. Rev. Lett. **56** (1986) 2811.

[35] J. R. Ferron, N. Hershkowitz, R. A. Breun, S. N. Golovato, and R. Goulding, Phys. Rev. Lett. **51** (1983) 1955.

[36] Y. Yasaka and R. Itatani, Nucl. Fusion **24** (1984) 445, Y Yasaka and R. Itatani, Nucl. Fusion **25** (1985) 29.

[37] O. Sakai, K. Noda, Y. Ohe, and Y Yasaka, Trans. Fusion Technol. (Proc. Int'l Toki Conf. on Plasma Physics and Nuclear Fusion Research (Toki, 1994)) **27** (1995) 417.

[38] J. C. Hosea and R. M. Sinclair, Phys. Fluids **13** (1975) 701.

[39] T. Watari, K. Adati, T. Aoki, S. Hidekuma, K. Hattori, S. Hiroe, M. Ichimura, T. Kawamoto, R. Kumazawa, Y. Ukobo, S. Okamura, T. Sato, C. M. Singh, and M. Sugawara, Nucl. Fusion **22**, 1359.

[40] M. Ichimura, M. Inutake, S. Adachi, D. Sato, F Tsuboi, Y. Nakashima, I. Katanuma, A. Itakura, A. Mase, and S. Miyoshi, Nucl. Fusion **28** (1988) 799.

[41] D. R. Roberts and N. Hershkowitz, Phys. Fluids B **4** (1992) 1475.

[42] R. B. White, S. Yoshikawa, and C. Oberman, Phys. Fluids **25** (1982) 384.

[43] C. N. Lashmore-Davies, V. Fuchs, and R. A. Cairns, Phys. Fluids **28** (1985) 1791.

[44] H. Akiyama, M. O. Hagler, IEEE Trans. Plasma Sci. **PS-13** (1985) 125.

[45] V E. Moiseenko, V. V Pilipenko, G. G. Zukakishvili, and A. M. Borozenets, Nucl. Fusion **33** (1993) 565.

[46] J. R. Johnson, T. Chang, and G. B. Crew, Phys. Plasmas **2** (1995) 1274.

[47] D. R. Roberts, N. Hershkowitz, and J. A. Tataronis, Phys. Fluids **2** (1990) 787.

[48] Y. Yasaka, H. Takeno, A. Fukuyama, T. Toyoda, M. Miyakita, and R. Itatani, Phys. Fluids B **4** (1992) 1486.

[49] O. Sakai and Y. Yasaka, Phys. Plasmas **1** (1994) 3896.

[50] M. Inutake, M. Ichimura, H. Hojo, Y Kimura, R. Katsumata, S. Adachi, Y. Nakashima, A. Itakura, A. Mase, and S. Miyoshi, Phys. Rev. Lett. **65** (1990) 3397

[51] S. -I. Itoh and K. Itoh, Phys. Rev. Lett. **60** (1988) 2276.

[52] K. C. Shaing and E. C. Crume, Jr., Phys. Rev. Lett. **63** (1989) 2369.

[53] R. J. Groebner, K. H. Burrel, and R. P Seraydarian, Phys. Rev. Lett. **64** (1990) 3015.

[54] R. J. Taylor, M. L. Brown, B. D. Fried, H. Grote, J. R. Liberati, G. J. Morales, and P. Pribyl, Phys. Rev. Lett. **63** (1989) 2365.

[55] H. Biglari, P. H. Diamond, and P W. Terry, Phys. Fluids B **2** (1990) 1.

[56] T. Ohbiki *et al.* (Heliotron-E Team) *Plasma Physics and Controlled Nuclear Fusion Research* (IAEA, Vienna, 1989) Vol. 2, p. 337.

[57] A. Tsushima, T. Mieno, M. Oertl, R. Hatakeyama, and N. Sato, Phys. Rev. Lett. **56** (1986) 1815.

[58] A. Mase, J. H. Jeong, A. Itakura, K. Ishii, M. Inutake, and S. Miyoshi, Phys. Rev. Lett. **64** (1990) 2281, A. Mase, A. Itakura, M. Inutake, K. Ishii, J. H. Jeong, K. Hattori, and S. Miyoshi, Nucl. Fusion **31** (1991) 1725.

[59] G. D. Severn, N. Hershkowitz, R. A. Breun, and J. R. Ferron, Phys. Fluids B **3** (1991) 114.

[60] R. J. Taylor, R. W Conn, B. D. Fried, R. D. Lehmer, J. R. Liberati, P. A. Pribyl, L. Schmitz, G. R. Tynan, B. C. Wells, D. S. Darrow, and M. Ono, *Plasma Physics and Controlled Nuclear Fusion Research* (IAEA, Vienna, 1991) Vol. 1, p. 463.

[61] V. Erckmann *et al.* (Wendelstein-X Team), Phys. Rev. Lett. **70** (1993) 2086.

[62] K. Toi *et al.* (CHS Team), *Plasma Physics and Controlled Nuclear Fusion Research* (IAEA, Vienna, 1993) Vol. 2, p. 461.

[63] O. Sakai, Y Yasaka, and R. Itatani, Phys. Rev. Lett. **70** (1993) 4071.

[64] O. Sakai, R. Itatani, and Y. Yasaka, Proc. Int'l. Conf. on Open Plasma Confinement Systems for Fusion (Novosibirsk, 1993) (World Scientific, Singapore, 1994), p. 197.

[65] O. Sakai and Y. Yasaka, Phys. Plasmas **2** (1994) 3249.

[66] H. Takeno, Y. Yasaka, O. Sakai, and R. Itatani, Nucl. Fusion **35** (1995) 75.

[67] T. H. Jensen and A. W Leonard, Phys. Fluids B **3** (1991) 3422.

[68] D. A. D'Ippolito, J. R. Myra, J. Jacquinot, and M. Bures, Phys. Fluids B **5** (1993) 3603.

Chapter 2

"ICRF Tandem Mirror" with Controlled Potential Profiles

2.1 Introduction

A mirror device has inherently a different magnetic field configuration to torus devices; Axial magnetic field lines are open to an end metal plate in an experimental device or will be open to an energy convertor in a future reactor, and the strength of magnetic field changes mainly parallel to its field lines. Assumed that a mirror plasma is sustained magnetohydrodynamically, confinement property strongly depends on axial transport (parallel to the magnetic field lines), although main loss channel will be *across* the magnetic field lines in the case of enhanced axial confinement.

In order to keep its simplicity, a tandem mirror can be operated by ICRF waves, as mentioned in Sec. 1. In such a machine ICRF propagation parallel to the field lines is the main path along its dispersion curve. Dispersion relation of ICRF wave is associated with not only ion heating but also potential formation for confinement through electron heating in an ICRF tandem mirror. Another feature of ICRF waves is that the scale length of the gradient of the radiofrequency (RF) field amplitude is comparable or less than machine characteristic length, which plays an important role on RF stabilization.

Another important subject in this chapter is theoretical review of radial confinement determined by micro instabilities. One of the causes of radial anomalous transport, which is present throughout magnetoplasmas, is considered to be due to micro instabilities in the edge of a plasma. Recent researches on H-mode physics revealed that radial potential profile affects micro instabilities that causes fluctuation-driven transport.

Section 2.1 describes dispersion relation of ICRF waves and its contributions to plasma production, ion and electron heating, and RF stabilization. Section 2.2 represents confinement properties based on propagation of ICRF waves and control of radial electric field. Subsection 2.2.1 shows property of axial confinement in an ICRF tandem mirror, subsection 2.2.2 describes magnetohydrodynamic stability affected by ICRF waves, and subsection 2.2.3 reviews radial transport caused by micro instabilities that can be affected by radial electric field.

2.2 Dispersion relation in ICRF waves and their contributions to plasma production, heating, and stabilization

Our starting point for description of ICRF propagation is the general dispersion relation in a cold and infinite plasma, expressed as

$$k_\perp{}^4 - [-k_{||}{}^2(\frac{P}{S}+1) + k_0{}^2(P+\frac{RL}{S})]k_\perp{}^2 + \frac{P}{S}(-k_{||}{}^2 + k_0{}^2R)(-k_{||}{}^2 + k_0{}^2L) = 0. \quad (2.1)$$

Here $k_\perp$ and $k_{||}$ are wavenumbers perpendicular and parallel to the static magnetic field, respectively, $k_0 = \omega/c$ with the applied RF frequency $\omega/2\pi$ and the light velocity c, and P, S, R, and L are dielectric tensor elements, defined in the Stix notation [1]. The dispersion relation written by $\omega - k_{||}$ diagram is useful to investigate propagation of the ICRF waves in a mirror device since waves propagating in the axial direction are dominant and the strength of the magnetic field B_0 changes mainly in the parallel direction. In the cylindrical plasma geometry with the surrounding vacuum layer and the conducting wall

[2], $k_\perp$ is determined from the boundary conditions with continuity of tangential electric and magnetic fields at the plasma-vacuum interface and zero of tangential electric field on the wall. The configuration of the cylindrical plasma also makes it possible to deal with the ICRF waves with a specific azimuthal mode number m, where RF field is assumed to vary as $\exp[j(m\theta - k_{||}z + \omega t)]$. When B_0 changes with the fixed RF frequency, the dispersion relation of a two-ion-species (He-H) plasma in the uniform profile of B_0 is derived as in Fig. 2.1. Here m is set to -1, which indicates that right-rotating propagation, and electron mass m_e is retained in the calculation. The calculation reveals that in this range of frequency and density only the $m = -1$ mode can propagate except the region near $\omega = \Omega_H$, minority (H) cyclotron resonance. Figure 2.1 shows that the fast wave mode propagates in the whole range of frequencies with some modification.

First, let us take a look of the range above the minority (H) cyclotron frequency ($\omega > \Omega_H$). The propagating wave, which is on the continuous branch of the fast magnetosonic wave ("F" in fig. 2.2), is called helicon wave ("H"), and its propagation has been investigated in terms of efficient plasma production with electron density $n_e > 10^{13}$ cm^{-3} [3–5]. One of the reasonable descriptions of production mechanism is RF power absorption via electron Landau damping. Equivalent collision frequency of electron Landau damping of the helicon wave is derived by Chen [4] as

$$\nu = 2\sqrt{\pi} y^3 \exp(-y^2), \tag{2.2}$$

where $y = \omega/k_{||}\ (m_e/2T_e)^{1/2}$ with electron temperature T_e. Takeno *et al.*[5] showed that the efficient damping takes place for the range of $k_{||} = 9 - 30$ m^{-1} with $T_e = 20$ eV, which is coincident with the range of the helicon wave propagation in Fig. 2.1. However, the production mechanism are now discussed in a number of different points of view, which is beyond the scope of this study. This production is more efficient than the slow wave production utilized in the GAMMA 10 tandem mirror [6]. The plasma production by

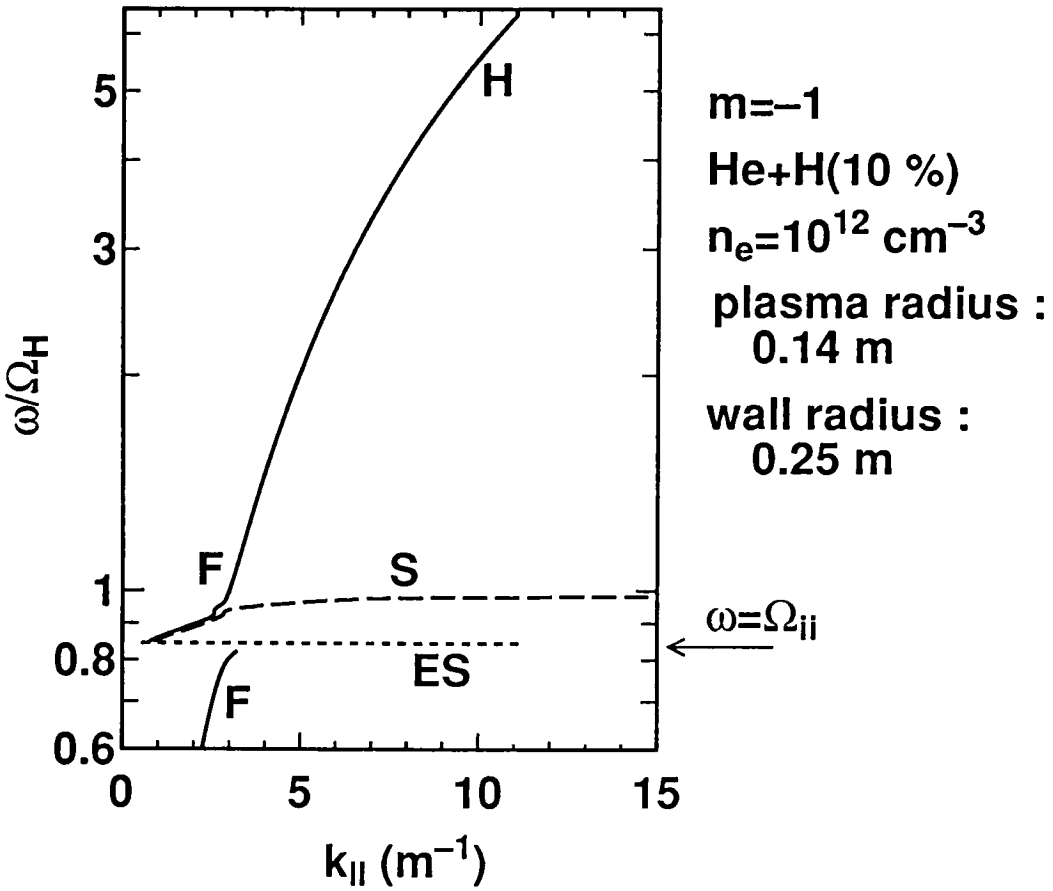

FIG. 2.1. Dispersion relation of ICRF waves near and above the minority ion cyclotron frequency ($\omega = \Omega_H$). The parameters used in the calculation are shown in the figure. Label "H"(solid line), "F"(solid line), "S"(dashed line) and "ES"(dotted line) denote the branches of the helicon wave, the fast magnetosonic wave, the slow ion-cyclotron wave with the lowest radial order, and the electrostatic wave near the ion-ion hybrid resonance ($\omega = \Omega_{ii}$).

the slow wave takes place in the magnetic beach configuration with the ion cyclotron resonance. In that case plasma with high ion temperature can be produced. However there exists density limit of the slow wave propagation, which will be discussed in the next paragraph.

Second, propagation near and below Ω_H is focused on its contributions to ion and electron heating. In a one-ion-species plasma, mirror magnetic beach heating has been investigated [6–8], and its efficiency to ion heating in a relatively low-density plasma was clarified. However, the slow wave has a poor accessibility to a high-density plasma. Considering refractive index perpendicular to the static magnetic field as a function of plasma density, the fast wave mode has no upper limit for its propagation [9], and the slow wave launched directly from an antenna propagates only below the density limit of $n_e \sim 2 \times 10^{12}$ cm^{-3} with $B = 0.6$ T and $k_{||} = 5$ m^{-1} On the other hand, with the presence of the minority ion, mode conversion from the fast magnetosonic to the slow ion-cyclotron wave can be expected. The cut-off point is present on the fast wave branch at the ion-ion hybrid resonance layer ($\omega = \Omega_{ii}$), and the slow wave branch emerges for $\Omega_{ii} \leq \omega \leq \Omega_H$ ("S", which in fig. 2.1 is the one with the lowest radial order). The slow ion-cyclotron wave is resonant at $\omega = \Omega_H$ with the minority (H) ion. There is a close pair of the cut-off and the resonance layers and the wave encountering this region is transmitted, reflected or absorbed. The mode conversion in the case of the low-field side ($\omega > \Omega_H$) launching takes place in the following sequence: the fast wave propagation, its reflection at $\omega = \Omega_{ii}$, mode conversion into the slow wave, and its propagation to the $\omega = \Omega_H$ layer [10]. As mentioned above, the fast wave is excited without a density limit, and the mode conversion into the slow wave results in the core ion heating of a high-density plasma like that in a fusion reactor through the ion cyclotron damping. This process is completely different from the case in a tokamak [11]. where the launched fast wave in the low field side converts into the

ion-Bernstein mode near $\omega = \Omega_{ii}$ with the *perpendicular* wave propagation and a thermal effect from the finite Larmour radius.

In the case of the high-field side launching ($\Omega_{He} < \omega < \Omega_{ii}$, where Ω_{He} is the majority ion cyclotron frequency), wave propagation is totally different from that of the low-field side launching. The fast wave branch just below $\omega = \Omega_{ii}$ ("F") shows a slight change to the higher $k_{||}$. As the wave gets close to $\omega = \Omega_{ii}$, Eq. 2.1 reduces to the cold electrostatic dispersion as

$$k_{\perp}{}^2 S + k_{||}{}^2 P = 0. \tag{2.3}$$

Ono [12] showed theoretically and experimentally that the slow ion-cyclotron wave converts into the cold electrostatic ion-cyclotron wave as approaching to the $\omega = \Omega_{ii}$ layer ("ES"). Besides transmitting wave to the fast wave branch above $\omega = \Omega_{ii}$, the wave through the narrow tunneling region for $\omega \leq \Omega_{ii}$ encounters this electrostatic branch, which may resonates with electron via Landau damping. On the other hand, Lashmore-Davies *et al.* predicted ion heating by 100 % energy conversion to the slow wave using a simple model equation, in which that electrostatic wave might be dropped in their approximation. Such a mode conversion process also completely differs from the case in a tokamak; In experiments of the fast wave excitation in tokamaks, the mode conversion to the ion Bernstein wave takes place, as mentioned above [11]. In the case of the high-field-side excitation this electrostatic wave gives its energy mainly to electrons (roughly 70 % [13]).

Another feature of ICRF waves is that wave length is comparable to or less than the characteristic length of a device, resulting in axial and radial gradient of RF electric fields. In the range of the helicon wave not only $m = -1$ but also $m = 0$, $+1$, and ± 2 modes can propagate. A radial profile of the RF fields is expressed by linear summation of mth order of Bessel function and its derivative with the azimuthal dependence of $\exp(jm\theta)$.

When a wave with adequate azimuthal mode number is excited, favorably-localized RF ponderomotive force affects flute mode stabilization [14], control of radial convection [34], and ponderomotive potential [16]. For instance, right-rotating polarization is dominant in the propagation of the $m = -1$ fast wave and the $m = -1$ helicon wave. The profile of the right-rotating field is peaking at the center of the plasma column, and that of the left-rotating field has a smaller peak in the periphery with zero amplitude at the center in a certain frequency range. Such profiles stabilizes flute mode, as discussed in Subsec. 2.3.2.

We note here that the helicon wave for plasma production and RF stabilization and the fast magnetosonic wave for ion and electron heating are on the same branch with different strength of the static magnetic field. If an ICRF wave is in the range of the helicon wave in the midplane of the central cell, it contributes to plasma production and RF stabilization. The same RF wave propagating towards the mirror point encounters the mode conversion region, which gives rise to ion and electron heating. That is, one ICRF wave can play a number of roles simultaneously in an ICRF tandem mirror.

2.3 Confinement properties in an ICRF tandem mirror

Confinement property in a magnetic confined device is basically characterized by its magnetic field configuration, and classical theory for each kind of device has been developed. However, many of such theories didn't explain experimental results [17]. Another important factor for confinement has been recently recognized, and it is plasma potential. Potential formation in a mirror device has been studied since the 70's for reduction of energy and particle loss along its open magnetic field lines. Furthermore, recent studies related to H-mode physics revealed that radial potential profile plays an essential role on radial confinement, i.e., transport across the magnetic field lines. That is, two- or

three-dimensional potential profile determines the global confinement in a mirror.

2.3.1 Axial confinement with potential formation along the field lines

In a simple mirror configuration, plasma is confined via reflection near the mirror point according to the conservation law of the magnetic moment. However, there exists the so-called "loss cone" which is displayed in the velocity space and in which plasma particles escape though the mirror point. Thus confinement time is not enough to realize an efficient reactor. For instance, $\tau_{p\|} = 0.20$ msec for the plasma with $n_e = 5 \times 10^{12}$ cm^{-3}, ion temperature $T_i = 60$ eV and mirror ratio $R_m = 7.1$, which is estimated from the rate of pitch angle scattering into the loss cone [18].

In order to enhance axial confinement, tandem mirror configuration with axial potential formation was proposed by Dimov *et al.* [19] and Baldwin *et al.* [20], shown in Fig. 2.2 with definition of ion-confining potential ϕ_c and thermal barrier depth ϕ_b. The first idea of a tandem mirror is that the plug cell with higher density than in the central cell creates the confining potential according to the Boltzmann relation, but in such a case the energy amplification factor of a reactor Q is estimated to remain low. Ion-confining potential with thermal barrier was thus proposed. In this case electron heating in the plug cell gives rise to formation of ion-confining potential with assistance of thermal barrier which avoids exchange of electrons in the central and plug cells with different T_e.

In general plasma potential is determined by a local difference from the condition of charge neutrality, or external and internal forces of expelling one kind of charged particles, i.e., ions or electrons. In order to create ϕ_c, hill-shaped potential in the plug cell, control of plasma parameters in the plug cell is necessary, which have been predicted by theories shown in the following. The most fundamental equation for expression of plasma potential difference along the magnetic field lines is the Boltzmann relation, and

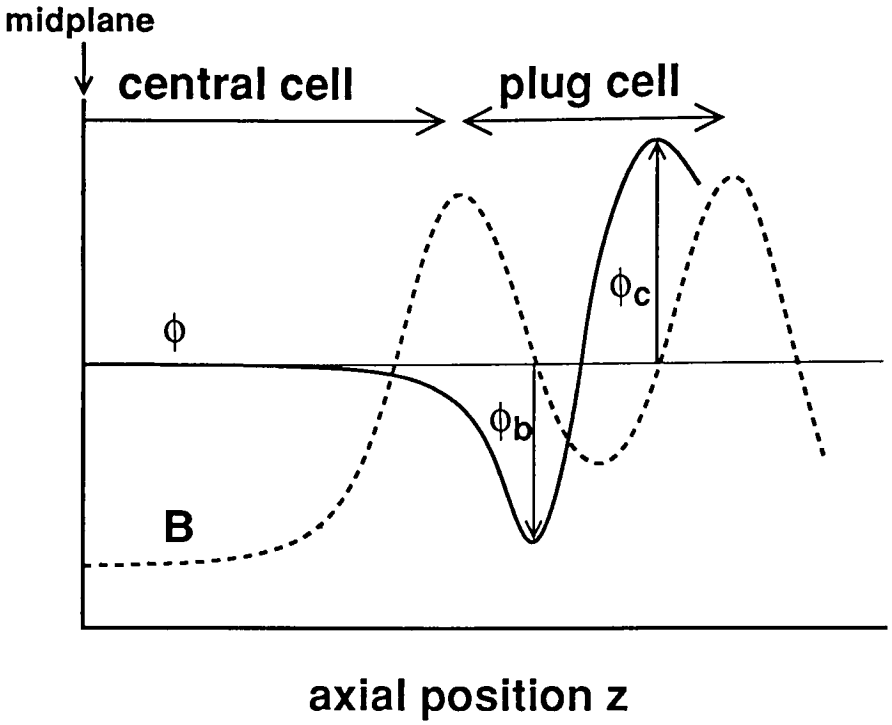

FIG. 2.2. Axisymmetric tandem mirror configuration expressed by the strength of static magnetic field ("B", dotted line) and the axial potential profile ("ϕ", solid line).

it reduces in the case of a tandem mirror to $e\phi_c = T_e \ln(n_{ep}/n_{ec})$ with electron density in the plug cell n_{ep} and that in the central cell n_{ec}. It shows that, with constant T_e throughout a tandem mirror device, higher density in the plug cell than in the central cell gives rise to ion-confining potential. However, this is an unrealistic situation in combined three simple mirrors, as mentioned previously. With the idea of thermal barrier, the modified Boltzmann relation was developed by Cohen *et al.* [21], which is

$$e(\phi_c + \phi_b) = T_{ep} \ln \left[\frac{n_{ep}}{n_{eb}} \left(\frac{T_{ec}}{T_{ep}} \right) \right], \tag{2.6}$$

where n_{eb} is electron density in the thermal barrier region, and T_{ep} and T_{ec} are electron temperature in the plug cell and that in the central cell, respectively. In other words, n_{eb} is density of the electrons passing from the central cell to the plug cell with temperature T_{ec}. According to Eq. 2.6, even if n_{ep} is less than n_{ec}, increase of T_{ep} by electron heating in the plug cell results in formation of ϕ_c, and there is no dependence on heating method such as electron cyclotron heating (ECH) and heating by ICRF waves (ICH).

In the modified Boltzmann relation electron energy distribution is assumed to be Maxwellian. If the distribution changes from Maxwellian towards plateau shape, that makes enhancement of potential formation. The influence of electron velocity space diffusion parallel to the magnetic field by RF fields was investigated theoretically by Hojo *et al.* [22] Starting from the Fokker-Plank equation with quasi-linear RF diffusion term, the derived expression for potential difference enhanced by RF fields is

$$e(\phi_c + \phi_b) = \frac{T_{ep}}{\lambda} \left\{ \left[\frac{n_{ep}}{n_{eb}} \left(\frac{T_{ec}}{T_{ep}} \right)^{1/2} \right]^{\lambda} - 1 \right\}, \tag{2.7}$$

where $\lambda = D_{RF}/D_{CL}$ is the ratio of the RF-induced to collisional diffusion coefficients in the electron velocity space. D_{RF} is estimated as $\pi e^2 {E_{||}}^2 / 8 {m_e}^2 \omega$ and $D_{CL} = (eT_{ep}/m_e)$ $/2(\sqrt{m_e} {T_{ep}}^{3/2} / 3\sqrt{2}\pi n_{ep} e^4 \ln \Lambda)$ with the Coulomb logarithm $\ln \Lambda$, so that λ is a function of the parallel RF (electrostatic) field $E_{||}$, T_{ep}, n_{ep}, and ω. Boundary conditions for dis-

tribution function are given by n_{ep}, T_{ep}, n_{eb}, and T_{ec}, and quasi-static approximation [23] is used to derive Eq. 2.7. Hojo also mentioned to the effect of radial particle diffusion on potential formation, and it was concluded that radial particle loss enhances ion-confining potential. We note that this radial loss in the plug cells is in the level of usual anomalous transport and make no degradation of particle confinement in the central cell. In the ultimate scheme of velocity space diffusion, i.e., "strong ICH" scheme, the electron distribution function becomes flat, and $e(\phi_c + \phi_b)$ is derived as $(\pi/4)T_{ec}(n_{ep}/n_{eb})^2$ Figure 2.3 displays enhancement of ion-confining potential by RF-induced velocity space diffusion. In this case validity of Eq. 2.7 is kept for $\lambda \leq 2.6$.

Figure 2.2 shows that thermal barrier between the central cell and the plug cell electrons enables efficient electron heating in the plug cell. Formation of such a potential depth by ICRF waves were investigated by Hershkowitz *et al.* [24] and Yasaka *et al.* [25] Yasaka *et al.* showed that thermal barrier formation and its sustainment were caused by ponderomotive potential of near fields of injected plug ICRF in the experiment in HIEI. Ponderomotive potential for ions by RF waves ϕ_{RF} is expressed as [26]

$$\phi_{RF} = \frac{q_i}{4m_i\omega}\left(\frac{{E_+}^2}{\omega - \Omega_i} + \frac{{E_-}^2}{\omega + \Omega_i} - \frac{{E_z}^2}{\omega}\right), \tag{1}$$

where m_i, q_i, and Ω_i are ion mass, ion charge, and ion cyclotron frequency, respectively. ω is the applied RF frequency, and E_+, E_-, and E_z are the RF electric fields of left-circularly-polarized, right-circularly-polarized, and axial components, respectively. In the experiment of Yasaka *et al.* E_z of the near fields is considered to be quite large, and potential well is formed with its width owing to axial profile of $|E_z|$. In another experiment in HIEI [27], thermal barrier formation was not controlled and spontaneous formation was utilized. Observation of this phenomenon on the boundary of two plasmas with different T_e was first reported by Hatakeyama *et al.* [28] The potential dip is enhanced with the presence of a mirror point on their boundary. In the case of HIEI, such a situation can

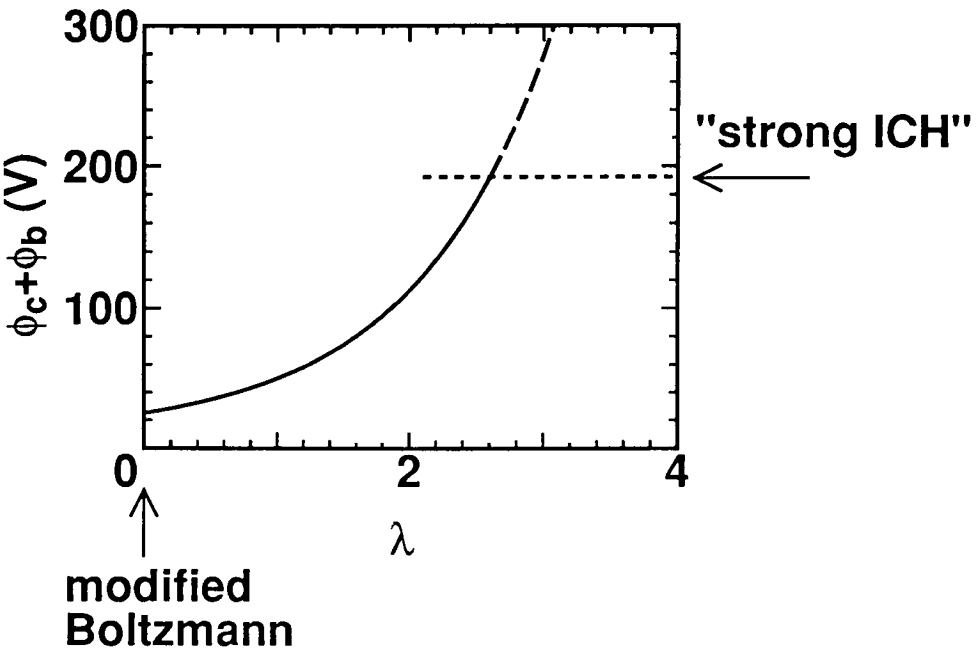

FIG. 2.3. Enhancement of ion-confining potential by RF-induced velocity space diffusion [22]. $n_{ep}/n_{eb}(T_{ec}/T_{ep})^{1/2} = 3.5$ and $T_{ep} = 20$ eV The case of $\lambda = 0$ indicates the modified Boltzmann relation, and dotted line indicates the scheme of "strong ICH"

occur at the mirror point between the central and the plug cells where the plasmas with T_{ec} and with T_{ep} encounter each other. Assumed that an electron flux flowing into the mirror point is simply expressed as $n_e \sin^{-1}(1/\sqrt{R_m})\sqrt{eT_e/m_e}$ with the mirror ratio R_m in the central cell 7.1 and that in the plug cell 2.6, the electron fluxes are equal with $n_{ec}/n_{ep} = 2.5$ and $T_{ep}/T_{ec} = 2.0$. If T_{ep} increases from this condition, the electron flux from the plug cell exceeds to that from the central cell and potential dip is formed in the central cell near the mirror point to make the electron current to be zero at the dip. Specific values of the potential dip and its location depends on magnetic field configuration near the mirror point and electron energy distribution functions in both cells. One related calculation of thermal barrier and reduction of electron heat flux was performed by Ohkawa *et al.* in the case of a scrape-off layer (SOL) plasma of divertor configuration [29].

In the configuration shown in Fig. 2.2, axial particle confinement time is estimated. According to the theoretical studies [23, 30, 31], particle confinement time in a collisionless regime $\tau_{p||a}$ is

$$\tau_{p||a} = \tau_{ii}\frac{\sqrt{\pi}}{2}\sqrt{\frac{R_m+2}{R_m}}\ln\left[\frac{\sqrt{\frac{R_m+2}{R_m}}+1}{\sqrt{\frac{R_m+2}{R_m}}-1}\right]\exp\left(\frac{e\phi_c}{T_{ic}}\right)\frac{\left(\frac{e\phi_c}{T_{ic}}\right)^2+\frac{1}{4}}{\frac{e\phi_c}{T_{ic}}+\frac{1}{2}}, \tag{2.4}$$

where τ_{ii} is ion collision time, and T_{ic} is ion temperature in the central cell. Particle confinement in a collisional regime $\tau_{p||b}$ is

$$\tau_{p||b} = \sqrt{\pi}R_m L\exp\left(\frac{e\phi_c}{T_{ic}}\right)/\sqrt{\frac{eT_{ic}}{m_i}}, \tag{2.5}$$

where L is length of the central cell, and m_i is ion mass. Particle confinement time of intermediate regime between collisional and collisionless cases $\tau_{p||}$ are simply expressed as $\tau_{p||} = \tau_{p||a} + \tau_{p||b}$. For instance, $\tau_{p||} = 4.5$ msec for the plasma with $n_e = 5 \times 10^{12}$ cm^{-3}, $T_{ic} = 60$ eV, $L = 1.9$ m, and $\phi_c = 70$ V, which is enhanced by more than one order from the value in a simple mirror (0.20 msec).

2.3.2 Stability of magnetohydrodynamic modes

In the central cell of a tandem mirror the region with bad curvature for the flute interchange mode spreads around the midplane, whereas good curvature region is around the mirror points. Plasma pressure is distributed mainly according to the mirror magnetic confinement in the central cell, so that the flute mode usually becomes unstable with the central cell alone. In a conventional tandem mirror, minimum-B configuration by baseball coils stabilizes a plasma magnetohydrodynamically. However, additional heating source is required to keep plasma pressure high in the minimum-B region, and such a nonaxisymmetric configuration enhances ion neoclassical transport [32, 33]. In order to avoid these inconveniences, another method for stabilization of the flute mode in a mirror was proposed, utilizing RF ponderomotive force in axisymmetric configuration [34, 35]. Yasaka *et al.* investigated RF stabilization in the frequency range of the helicon wave [34], while Ferron *et al.* examined it using the Alfvén wave. Here we review its effects in the helicon wave regime in the following part.

Stability criteria against the flute interchange mode with the effects of RF fields is determined by both two-dimensional (radial and axial) profiles of plasma pressure and RF fields. The effects of the radial profiles were investigated in the range of $2.3 \leq \omega/\Omega_i \leq 2.6$ by Yasaka *et al.* [34, 36] RF ponderomotive force F_p is written as

$$F_p = \sum_{\alpha=e,i} -\frac{{q_\alpha}^2}{4m_\alpha\omega}\left(\frac{\nabla {E_+}^2}{\omega-\Omega_\alpha}+\frac{\nabla {E_-}^2}{\omega+\Omega_\alpha}+\frac{\nabla {E_z}^2}{\omega}\right), \tag{2.8}$$

where E_+, E_-, and E_z are the RF components of the left-circularly-polarized, right-circularly-polarized, and axial field, respectively, and q_α, m_α, and Ω_α are the charge, mass, and cyclotron frequency of α species (electron or ion). Condition of $F_p \geq e(T_i + T_e)/R_c$ is required for stabilization, where R_c is the curvature radius of the magnetic field lines. Radial gradient of amplitude profile of RF fields was successfully controlled by mode-controlled RF excitation. Profile of RF wave with $m = \pm 2$ has a smaller radial scale

length ($\sim$ 4 cm) than that with $m = \pm 1$ ($\sim$ 14 cm). As a result, the stabilization effect was observed in the case of $m = \pm 2$ due to larger $\nabla {E_\perp}^2$ and not observed in the case of $m = \pm 1$ [34]. In another report stabilization criteria was examined using maximum value of F_p and R_c to see the effect of radial dependence [36]. Takeno *et al.* [37] showed that influence of side band waves could not be ignored in the range of $\omega/\Omega_i = 14 - 34$ and $n_e \leq 3 \times 10^{12}\mathrm{cm}^{-3}$ in which side band waves can propagate. The effect of the side band cancels 60 % of RF stabilization of direct ponderomotive force (Eq. 2.8). It can be concluded that favorable mode excitation of RF waves and suppression of side band effect by parameter control create a RF stabilized mirror plasma.

Another important aspect of RF stabilization is an effect of axial profiles of plasma pressure and RF field amplitude. Stability criteria with such effects against the flute mode is written as [38, 39]

$$\int_{-l}^{l} \frac{dz}{B} \kappa_\psi P \geq 0, \tag{2.9}$$

where l is the length from the midplane to the mirror point of the central cell, $\boldsymbol{\kappa} = (\boldsymbol{b} \cdot \boldsymbol{\nabla})\boldsymbol{b} = \kappa_\psi \boldsymbol{\nabla}\psi + \kappa_\theta \boldsymbol{\nabla}\theta$, magnetic field vector $\boldsymbol{B} = B\boldsymbol{b}\nabla\psi \times \boldsymbol{\nabla}\theta$, and P is the plasma pressure. In the presence of RF waves, it is more convenient to express κ_ψ as $\kappa_{\psi 0} + \kappa_{\psi F_p}$, where $\kappa_{\psi 0}$ is defined by the above expression and $\kappa_{\psi F_p}$ is the equivalent term from contribution of F_p using the relation $F_p = e(T_i + T_e)/R_{cF_p} = e(T_i + T_e)\sin^{-1}(\kappa_{\psi F_p})$.

2.3.3 Radial confinement with suppression of micro instabilities

Even if magnetohydrodynamic mode is stable, radial confinement in a magnetic confined plasma is much smaller than that predicted by classical transport [17]. This anomalous transport across the magnetic field lines is partly due to micro instabilities in the edge. Fluctuation-driven transport is written in general as

$$\Gamma_t = < \tilde{n}\tilde{v}_r > \cong \int_{-\infty}^{\infty} d\omega \tilde{n}^*(\omega)\tilde{v}_r(\omega), \tag{2.10}$$

where the right hand side is convolution of fluctuations of density n and radial velocity v_r. If the microturbulence is electrostatic, $\tilde{v_r} = \boldsymbol{E_\theta} \times \boldsymbol{B}/B^2 \rightarrow ik_\theta \tilde{\phi}/B$, where $k_\theta (= m/r)$ and ϕ indicate azimuthal wavenumber and plasma potential, respectively. Fluctuation-driven transport is outward when $\tilde{n}$ and $\tilde{v_r}$ are in phase, so that suppression of micro instabilities driving such turbulence is a key issue for enhancement of radial confinement.

One of the micro instabilities driving anomalous losses is the drift wave mode. Observations of $\hat{\text{H}}$ mode correlate improved confinement with reduction in the drift wave turbulence [40]. The dispersion relation of the drift and drift-Alfvén waves in a cylindrical plasma was derived by Fredrickson *et al.* [41], shown in Fig. 2.4. The drift mode rotates in the direction of electron diamagnetic drift and its rotational frequency is near the electron diamagnetic frequency for large $k_{||}$. The dispersion of the low-frequency edge fluctuations observed in the HIEI tandem mirror is also plotted in Fig. 2.4 as vertical and horizontal bars. The detected fluctuations are in good agreement with the branch of the drift mode. Several theoretical studies suggested suppression of drift wave turbulence by radial potential profiles with rigid plasma rotation. Sanuki [42] and Chaudhry *et al.* [43] assumed a parabolic ambipolar potential and investigated the growth rate of the drift wave as a function of potential. The numerical result showed that a slightly negative (well-shaped) potential destabilizes the drift wave and that both further increase of negative potential and increase of positive potential lower its growth rate. Similar result was reported by Horton *et al.* using analytical study [44].

Another possible method for suppression of edge turbulence like the drift wave mode is creation of sheared plasma rotation, or large radial gradient of radial electric field. Biglari *et al.* proposed shear stabilization of edge turbulence in order to explain turbulence suppression in a *H*-mode discharge [45]. If sheared azimuthal rotation is present in the edge, azimuthal decorrelation of two fluids in different radial positions is enhanced by difference

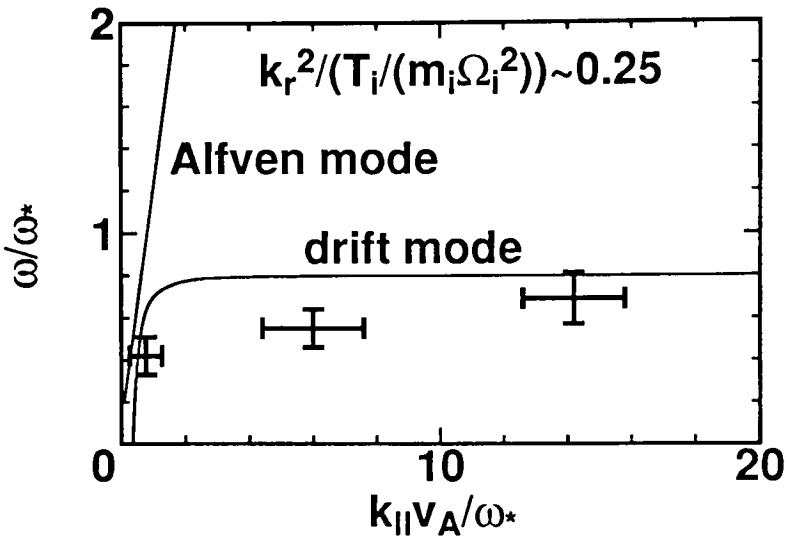

FIG. 2.4. Dispersion relation of the drift and drift-Alfvén waves in a cylindrical plasma [41]. k_r is defined as ${x_j}^m/a$, where ${x_j}^m$ is the jth order of the mth Bessel function and a is plasma radius. v_A is the Alfvén velocity, and ω_* is the electron diamagnetic drift frequency. Inset vertical and horizontal bars show edge fluctuations observed in the HIEI tandem mirror.

of azimuthal flow, so that edge turbulence quenches. Hinton proposed bifurcation theory for *L-H* transition using shear stabilization effect, in which radial diffusion coefficient was described as a function of rotational shear [46]. Staebler *et al.* developed Hinton's theory for more close configuration to tokamak experiments [47]. They define radial energy flux Q and particle flux Γ as

$$Q = -\left(\chi_H + \frac{\chi_L}{1+\alpha_Q|S_\perp|^\gamma}\right)\frac{1}{n}\frac{dP}{dr},\ \Gamma = -\left(D_H + \frac{D_L}{1+\alpha_\Gamma|S_\perp|^\gamma}\right)\frac{1}{n}\frac{dn}{dr} \tag{2.11}$$

Here thermal conductivity χ and diffusion coefficient D, expressed in the large brackets in Eq. 2.11, have dimensions of conductivity. $S_\perp$ represents the $E \times B$ rotational shear, and α_Q, α_Γ, and γ are constants. D expressed in Eq. 2.11 indicates that $D = D_H + D_L$ in the case of $S_\perp = 0$ and $D \to D_H$ for $S_\perp \to \infty$. New operator f is defined as $(c/eB)(Q\Gamma/\chi_H D_H)$ for expression of energy input by additional heating assumed that $S_\perp$ simply depends on radial gradient of the ion diamagnetic drift and that fueling rate (Γ) is constant. That is,

$$f \equiv \frac{c}{eB}\frac{Q\Gamma}{\chi_H D_H} = \left(1+\frac{\chi_L/\chi_H}{1+\alpha_Q|S_\perp|^\gamma}\right)\left(1+\frac{D_L/D_H}{1+\alpha_\Gamma|S_\perp|^\gamma}\right)S_\perp \tag{2.12}$$

Figure 2.5 displays that bifurcation of $S_\perp$ and therefore that of radial diffusion and thermal conductivity as a function of f As f is increased, which corresponds to increase of additional heating power, low (L) confinement phase ($S_\perp < 1.5$) jumps to high (H) confinement phase at $f \sim 19$. In the case of decreasing f, transition from L phase to H phase takes place at $f \sim 12$, which indicates that hysteresis phenomenon is inherent in *L-H* transition. This analysis is based on a cylindrical geometry, so that this is applicable to mirror configuration.

However some additional conditions should be under consideration in order to analyze radial confinement in a mirror. A mirror device has two paths of energy and particle loss: axial direction and radial direction. When radial confinement itself or any factors

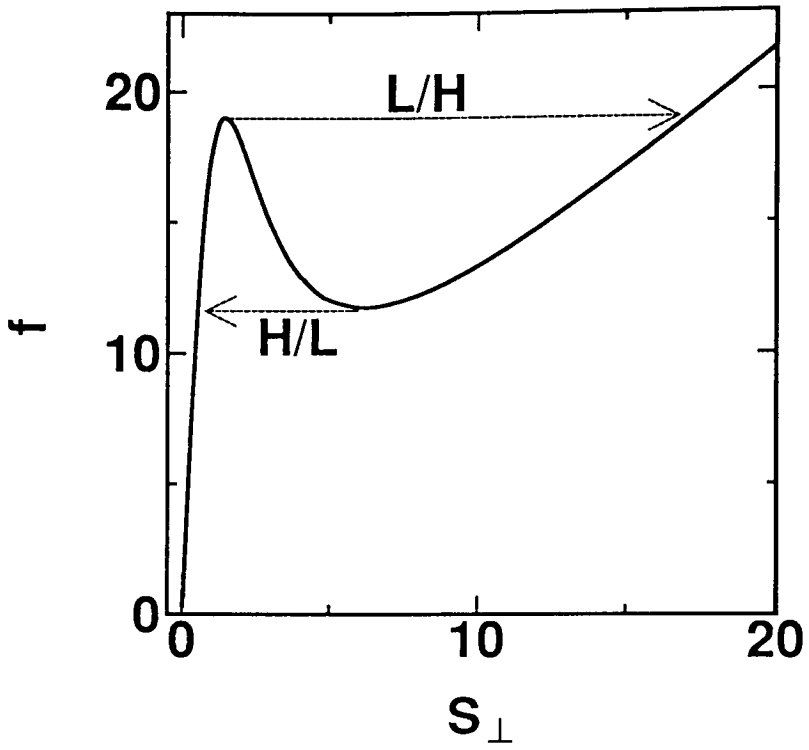

FIG. 2.5. Model of bifurcation of $S_\perp$ as a function of f [47]. $\chi_L/\chi_H = D_L/D_H = 4$, $\alpha_Q = \alpha_\Gamma = 0.25$, and $\gamma = 2$.

affecting radial confinement changes, such changes may affect axial confinement. The first proposal for explanation of *L-H* transition by Ohkawa *et al.* [29] dealt with energy transport along the magnetic field lines in SOL influenced by radial energy flux across separatrix in divertor configurations. By additional heating in a diverter tokamak, ions in the periphery are heated and have larger Larmour radius, so that plasma potential becomes more positive just outside the separatrix. On the other hand, larger heat flux to outer divertor plates enhances cold plasma production due to higher neutral density. Hot electrons just outside the separatrix and cold dense electrons in front of the divertor plates are connected through an accretion region near X-point, where a mirror point exists. In order for electron current to be zero, thermal barrier to separate each electron group to a certain extent is spontaneously formed, and electron heat flux from SOL to the divertor plates is reduced, which means that energy transport across the field lines is reduced, leading to enhancement of the whole energy confinement. Another principle of relation between axial and radial confinement was recently proposed by Hojo in terms of axial potential formation [48]. Axial ion-confining potential is assumed to affect radial diffusion coefficient through sheared $E \times B$ rotation like expression in Eq. 2.11. Then both radial and axial confinement times change with bifurcated solutions in some parameter range. Such studies remain in the primary level, and more development is expected.

2.4 Overview of ICRF tandem mirror with controlled two- dimensional potential profiles

The above sections are summarized as follows: (i) Although axial inhomogeneity in a mirror makes the magnetohydrodynamical mode unstable, it also provides mirror confinement and propagation and resonance phenomena of variety of ICRF waves, one of which contributes to plasma production and stabilization of the unstable mode, and another of

which contributes heating and improvement of axial confinement. (ii) Confinement both along and across the magnetic field lines in a mirror device is determined by electrostatic potential profiles which can be controlled by resonance of ICRF waves resulting from axial inhomogeneity and by external input of additional power. In this study, in order to accomplish operation of a high-density, high-temperature, and well-confined mirror plasma, such features in a mirror are utilized and the above hypothesis is examined.

Figure 2.6 shows the operation scenario of an axisymmetric mirror by ICRF waves and DC electric fields. First, plasma is produced in the propagation of the helicon wave, and stabilized simultaneously against the flute interchange mode. Second, the fast wave is launched in the central cell and resonates with ions in the central cell and with electrons in the plug cell through sequential mode conversions. As a result, ion heating takes place in the central cell, and electron heating and velocity space diffusion in the plug cell cause enhancement of ion-confining potential. Finally, DC electric fields are imposed on the central cell plasma near the radial edge by limiter biasing in the central cell. Such a localized radial electric field E_r induces sheared $EtimesB$ rotation, which suppresses edge turbulence and reduces fluctuation-induced transport. Note that in this scenario inherent property of a mirror device ("axial inhomogeneity") is systematically linked to optimum confinement regime ("controlled two-dimensional potential profiles") through ICRF waves and DC electric fields.

References

[1] T. H. Stix, *The Theory of Plasma Waves* (McGraw-Hill, New York, 1962).

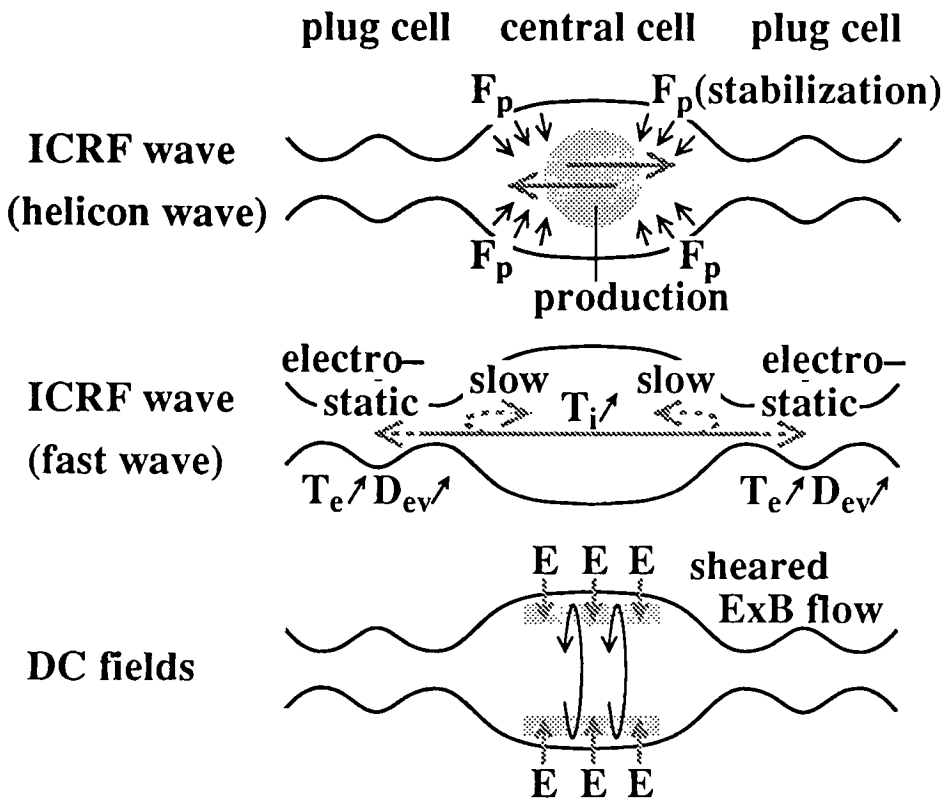

FIG. 2.6 Operation scenario of an axisymmetric mirror by ICRF waves and DC electric fields.

[2] W P Allis, S. J. Buchsbaum, and A. Bers, *Waves in Anisotropic Plasmas* (MIT Press, Cambridge, 1963).

[3] R. Boswell, Plasma Phys. Control. Fusion **26** (1984) 1147.

[4] F F. Chen, Plasma Phys. Control. Fusion **33** (1991) 339

[5] H. Takeno, Y. Yasaka, O. Sakai, and R. Itatani, Nucl. Fusion **35** (1995) 75.

[6] M. Ichimura, M. Inutake, S. Adachi, D. Sato, F Tsuboi, Y. Nakashima, I. Katanuma, A. Itakura, A. Mase, and S. Miyoshi, Nucl. Fusion **28** (1988) 799.

[7] J. C. Hosea and R. M. Sinclair, Phys. Fluids **13** (1975) 701.

[8] T. Watari, K. Adati, T. Aoki, S. Hidekuma, K. Hattori, S. Hiroe, M. Ichimura, T. Kawamoto, R. Kumazawa, Y. Ukobo, S. Okamura, T. Sato, C. M. Singh, and M. Sugawara, Nucl. Fusion **22**, 1359.

[9] F. J. Paoloni, Phys. Fluids **18** (1975) 640.

[10] C. N. Lashmore-Davies, V Fuchs, and R. A. Cairns, Phys. Fluids **28** (1985) 1791.

[11] J. Hosea, S. Bernabei, P Colestock, S. L. Davis, P Efthimion, R. J. Goldston, D. Hwang, S. S. Medley, D. Mueller, J. Strachan, and H. Thompson, Phys. Rev. Lett. **43** (1979) 1802.

[12] M. Ono, Phys. Rev. Lett. **42** (1979) 1267.

[13] S. -I. Itoh, A. Fukuyama, A. Goto, K. Itoh, K. Sakai, S. Takeuchi, M. Matsumoto, R. Sugihara, in 10th Int. Conf. on Plasma Physics and Controlled Nuclear Fusion Research London(1984) (IAEA, Vienna, 1985) Vol. 1, p. 541.

[14] Y. Yasaka and R. Itatani, Phys. Rev. Lett. **56** (1986) 2811.

[15] Y. Yasaka and R. Itatani, Phys. Rev. Lett. **44** (1980) 1763.

[16] N. Hershkowitz, B. A. Nelson, J. Johnson, J. R. Ferron, H. Persing, C. Chan, S. N. Golovato, and J. D. Callen, Phys. Rev. Lett. **55** (1985) 947.

[17] P C. Liewer, Nucl. Fusion **25** (1985) 543.

[18] D. V Sivukhin, *Review of plasma physics* (Consultants Bureau, New York, 1966).

[19] G. I. Dimov, V V Zakaidakov, and M. E. Kishinevskii, Sov. J. Plasma Phys. **2** (1976) 326.

[20] D. E. Baldwin and B. G. Logan, Phys. Rev. Lett. **43** (1979) 1318.

[21] R. H. Cohen, I. B. Bernstein, J. J. Dorning, and G. Rowlands, Nucl. Fusion **20** (1980) 1421.

[22] H. Hojo, T. Hatori, and S. Miyoshi, J. Phys. Soc. Jpn. **59** (1990) 789, H. Hojo, J. Phys. Soc. Jpn. **62** (1993) 4148.

[23] V. P. Pastukhov, Nucl. Fusion **14** (1974) 3.

[24] N. Hershkowitz, B. A. Nelson, J. R. Ferron, R. H. Goulding, and E. Wang, Nucl. Fusion **28** (1988) 1333.

[25] Y. Yasaka, M. Miyakita, S. Kimoto, H. Takeno, and R. Itatani, in *Plasma Physics and Controlled Nuclear Fusion Research* (IAEA, Vienna, 1991) Vol. 2, p. 725.

[26] N. Hershkowitz, B. A. Nelson, J. Johnson, J. R. Ferron, H. Persing, C. Chan, S. N. Golovato, and J. D. Callen, Phys. Rev. Lett. **55** (1985) 947.

[27] Y Yasaka, O. Sakai, H. Takeno, and H. Hojo, Nucl. Fusion **34** (1994) 1263.

[28] R. Hatakeyama, Y. Suzuki, and N. Sato, Phys. Rev. Lett. **50** (1983) 1203.

[29] T. Ohkawa, M. S. Chu, F. L. Hinton, C. S. Liu, and Y. C. Lee, Phys. Rev. Lett. **51** (1983) 2101.

[30] R. H. Cohen, M. E. Rensink, T. A. Cutler, and A. A. Mirin, Nucl. Fusion **18** (1978) 1229.

[31] T. D. Rognlien and T. A. Cutler, **20** (1980) 1003.

[32] D. D. Ryutov and G. V. Stupakov, Sov. J. Plasma Phys. **4** (1978) 278.

[33] I. Katanuma, Y Kiwamoto, S. Adachi, M. Inutake, K. Ishii, K. Yatsu, K. Sawada, and S. Miyoshi, Nucl. Fusion **27** (1987) 2041.

[34] Y. Yasaka and R. Itatani, Phys. Rev. Lett. **56** (1986) 2811.

[35] J. R. Ferron, N. Hershkowitz, R. A. Breun, S. N. Golovato, and R. Goulding, Phys. Rev. Lett. **51** (1983) 1955.

[36] Y. Yasaka and R. Itatani, Nucl. Fusion **24** (1984) 445, Y Yasaka and R. Itatani, Nucl. Fusion **25** (1985) 29.

[37] H. Takeno, Y Yasaka, and R. Itatani, Phys. Fluids B **4** (1992) 1255.

[38] W. A. Newcomb, J. Plasma Phys. **26** (1981) 529.

[39] H. Hojo, M. Inutake, M. Ichimura, R. Katsumata, and T. Watanabe, Jpn. J. Appl. Phys. **32** (1993) 2116.

[40] C. P. Ritz, H. Lin, T. L. Rhodes, and A. J. Wooton, Phys. Rev. Lett. **59** (1990) 2543.

[41] E. D. Fredrickson and P M. Bellan, Phys. Fluids **28** (1985) 1866.

[42] H. Sanuki, Phys. Fluids **27** (1984) 2500.

[43] M. B. Chaudhry, H. Hojo, T. Watanabe, and K. Nishikawa, J. Phys. Soc. Jpn. **57** (1988) 3043.

[44] W. Horton and J. Liu, Phys. Fluids **27** (1984) 2067.

[45] H. Biglari, P. H. Diamond, and P. W. Terry, Phys. Fluids B **2** (1990) 1.

[46] F L. Hinton, Phys. Fluids B **3** (1991) 696.

[47] G. M. Staebler, F. L. Hinton, J. C. Wiley, R. R. Dominguez, C. M. Greenfield, P Gohil, T. K. Kurki-Suonio, and T. H. Osborne, Phys. Plasmas **1** (1994) 909.

[48] H. Hojo, NIFS-PROC-22 (1995) 33.

Chapter 3

Mode Conversions of Fast Magnetosonic Waves with Selective Minority Ion and Electron Heating in a Longitudinally Inhomogeneous Magnetic Field

3.1 Introduction

Several schemes of ion heating via ICRF (Ion Cyclotron Range of Frequencies) waves have been proposed for a magnetoplasma [1]. Several modes propagating in a magnetoplasma are present in ICRF, and the contribution of each mode to ion heating depends on its own dispersion relation. The slow ion-cyclotron wave resonates directly with ions immersed in a magnetic field, but has poor accessibility to a high-density plasma like the one in a future reactor. On the other hand, the fast magnetosonic wave can propagate in a high-density plasma but it is less capable of accelerating plasma particles. From this point of view, mode conversion plays an important role. In tokamaks where the main magnetic field gradient is perpendicular to a static magnetic field, fast wave heating via mode conversion has been extensively explored, both in experiments [2] and theories [1, 3]. In this operation, the fast wave is launched in a two-ion-species plasma and converts

into the ion Bernstein wave near the ion-ion hybrid resonance layer.

In mirror machines, ICRF has been studied as a scheme for heating ions as well as for potential formation [4–6] and for plasma production [4, 7]. Magnetic beach heating was investigated in Phaedrus experiments [8], in which the addition of a second ion species changes excitation of the wave eigenmodes, leading to improvement on the accessibility to the high-density plasma. In GAMMA 10, mode conversion from the fast to the slow wave took place through the spatial modulation of magnetic field lines in the quadrupole field region [7]. In our configuration described in this paper, variance of the magnetic field strength parallel to the field line, which is inherent in mirrors, plays an essential role on mode conversion. According to the theoretical works [9, 10], the fast magnetosonic wave that is launched in a two-ion-species plasma from the low-field side converts into the slow ion-cyclotron wave in the vicinity of the close pair of the ion-ion hybrid and minority ion cyclotron resonance layers, and resonates with minority lighter ions at the minority ion cyclotron resonance. However, the experimental studies which have been done so far are not sufficient for understanding of the specific feature of this mode conversion process.

In single mirror operation [11], enhancement of radio frequency (RF) fields of the slow wave mode and associated ion heating were observed in the presence of the ion-ion hybrid resonance with appropriate minority ion concentration (5 %–10 %). These experimental results on radial profiles of RF fields and on ion heating were in qualitative agreement with the one-dimensional (1-D) mode conversion theory [10] and two-dimensional (2-D) calculation. Another report [4] demonstrated that the maximum heating efficiency was obtained by excitation of the right-rotating field, which is favorable for launching of the fast wave, which will convert into the slow wave mode. Roberts *et al.* [12] revealed the change of the propagating mode from the fast wave to the slow wave across the Alfvén resonance layer by calculating the dispersion relation in a two-ion-species plasma. Such

change was identified experimentally by various radial profiles of the wave fields. However, no direct measurement of the longitudinal dispersion relation of the mode-converted slow wave mode was reported. They predicted theoretically the presence of the slow wave with higher radial orders, which can contribute to minority ion heating, although no experimental result was shown on ion heating, such as an increase in ion temperature.

In the case of the high-field-side launching of the fast wave, one theoretical study by Davies [10] showed that the whole energy of the fast wave converted into the slow wave which gives rise to the minority ion heating. However the calculation by Roberts [12] suggested that the branch of the fast wave was not connected to the slow wave mode and showed some resonance near the ion-ion hybrid resonance layer. No experimental result has been available so far.

The present chapter deals with mode conversion phenomena of ICRF waves in the HIEI tandem mirror. ICRF wave propagation revealed by direct measurements of longitudinal dispersion relation is demonstrated. In the case of the $m = -1$ (right-rotating propagation) fast magnetosonic wave launching, the $m = -1$ slow ion-cyclotron wave is detected between the resonance (the minority ion cyclotron resonance) and cut-off (the ion-ion hybrid resonance) layers in the central cell, and an electrostatic wave is possibly present in the vicinity of the ion-ion hybrid resonance layer in the plug cell, where m is the azimuthal mode number. 1-D and 2-D theoretical analyses of the dispersion relation in a cylindrical plasma are described, which yields calculated wave numbers in reasonable agreement with measured wave numbers parallel to the static magnetic field $k_{||}$. Increases in minority ion temperature with the presence of the slow wave and electron temperature in the plug cell are also shown.

We start from review of dispersion relation of ICRF waves in a cylindrical plasma immersed in a longitudinally inhomogeneous magnetic field in Sec. 3.2. The experimental

setup is described in Sec. 3.3, where the measurement technique of $k_{||}$ for each rotating wave field is mentioned. The experimental results on measurements of propagating waves are presented in Subsec. 3.4.1, which are followed by observation of minority ion heating in Subsec. 3.4.2 and electron heating in Subsec. 3.4.3. In Sec. 3.5 the experimental results on $k_{||}$ are compared with the theoretical dispersion relation described in Sec. 3.2. The conclusion follows in Sec. 3.6.

3.2 Review of mode conversion features due to axial inhomogeneity

In this section we review the dispersion relation of ICRF waves in a longitudinally inhomogeneous magnetic field. White *et al.* predicted theoretically that the fast magnetosonic and slow ion-cyclotron waves are coupled for a finite perpendicular wave number $k_\perp$ in the presence of a second ion species [9]. Lashmore-Davies *et al.* developed this theory and derived the transmission, reflection, and mode conversion coefficients in a simpler manner [10]. Their theories remain within 1-D calculations with infinite plasma approximation.

We examine the dispersion relation with the effects of radial boundary conditions. The derivation is based on the work by Allis *et al.* [13], including the effect of the presence of a second lighter ion species. We assume that a cold, cylindrical and uniform plasma is enclosed by a vacuum layer and a perfectly conducting vessel in a constant magnetic field B_0 in the z direction. We take into account the boundary conditions that the azimuthal and axial components of RF electric and magnetic fields ($\boldsymbol{E}$ and $\boldsymbol{B}$, respectively) in the vacuum layer and the plasma region are continuous at the plasma surface, and the azimuthal and axial components of $\boldsymbol{E}$ are zero on the surface of the conducting wall. Such boundary conditions are used to derive the values of $k_\perp$ so that $k_\perp$ is neither zero nor

constant. The calculated parallel dispersion relation is shown in Fig. 3.1, where $\omega/2\pi$, Ω_H and Ω_{He} are the applied wave, minority (H) ion cyclotron and majority (He) ion cyclotron frequencies, respectively. ω/Ω_H in Fig. 3.1 in dielectric tensor elements (R, L, S, and D in Stix's notation [14]) is swept in the calculation by changing a value of B_0 with a fixed $\omega/2\pi = 8$ MHz. We set the similar plasma parameters to those in the experiments : $m = -1$, density $n_e = 1 \times 10^{12}$ cm^{-3}, minority ion concentration $\nu_H = 10$ % with majority (He) ion concentration $\nu_{He} = 90$ %, plasma radius $r_p = 5.5$ cm, and wall radius $r_w = 7.0$ cm. It is of considerable importance that the inertial effects of electrons are not ignored in R and L.

The sketched dispersion relation in Fig. 3.1 shows the mode-conversion feature in a longitudinally inhomogeneous magnetic field. The fast wave mode (shown as branch F) incident from the low-field side (the upper side in Fig. 3.1) encounters the Alfvén resonance layer $S = (k_\parallel c/\omega)^2$ ($\omega/\Omega_H \sim 0.92$ in Fig. 3.1), where c is the light velocity. Here the energy of the fast wave converts into the slow wave mode, with the lowest radial order (S_1). It is reflected on the cut-off layer at the ion-ion hybrid resonance, expressed as

$$\omega = \Omega_{ii} \equiv \left(\Omega_H \Omega_{He} \frac{\nu_H \Omega_{He} + \nu_{He} \Omega_H}{\nu_{He} \Omega_{He} + \nu_H \Omega_H} \right)^{1/2}, \tag{3.1}$$

which comes from $S = 0$ and corresponds to $\omega/\Omega_H \sim 0.84$ in Fig. 3.1. A part of reflected waves which will not go back to branch F proceeds along the slow wave branches with higher radial orders (S_2, S_3, ...) into the resonance condition near the minority ion cyclotron resonance layer ($\omega = \Omega_H$). The hatched region in Fig. 3.1 represents the slow wave branches with higher radial orders. On the other hand, propagation of the fast wave from the high-field side is completely different from that from the low-field side. The fast wave branch below the ion-ion hybrid resonance shows a slight change in the vicinity of $\omega = \Omega_{ii}$. It appears to experience some resonance through another mode conversion,

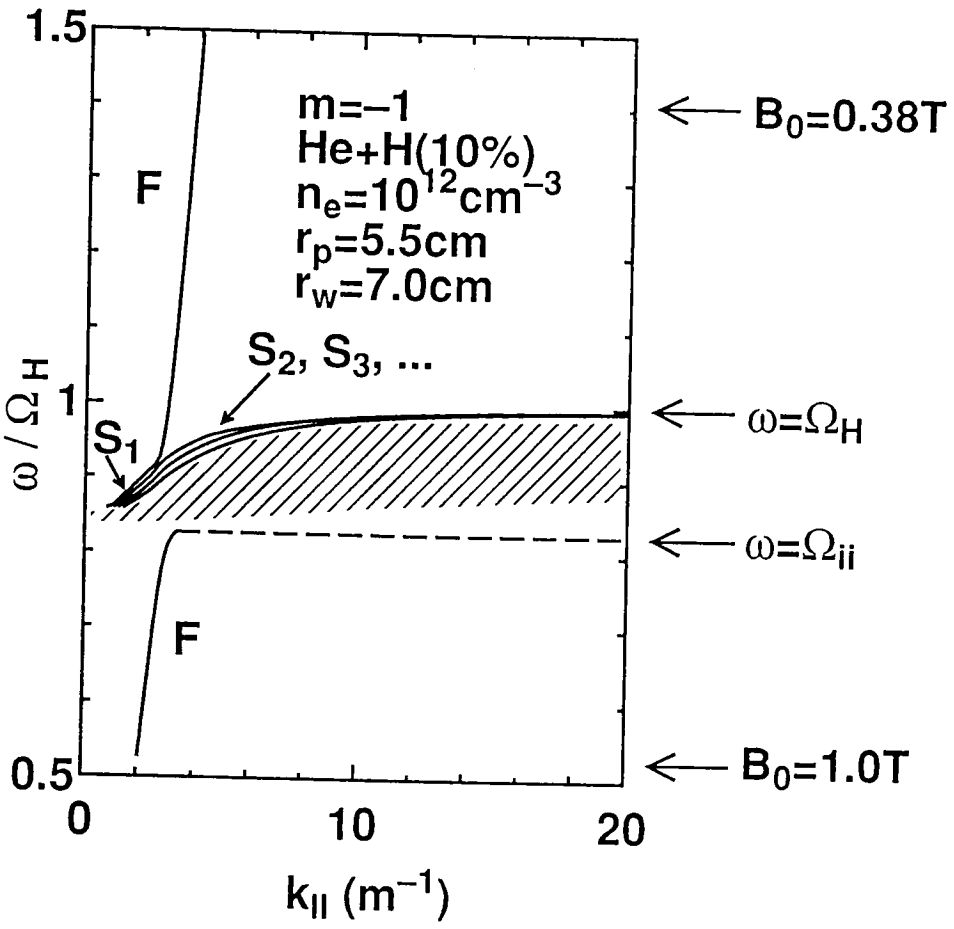

FIG. 3.1. Dispersion relation in a cylindrical plasma in the normalized frequency range of the mode conversion. F denotes the branch of the fast wave mode. S_1 denotes the branch of the slow wave mode with the lowest radial order ($0.84 \leq \omega/\Omega_H \leq 0.90$). The branches of the slow wave mode with higher radial orders are shown as S_2, S_3, ... and the hatched region between the ion-ion hybrid resonance ($\omega = \Omega_{ii}$) and the minority (H) ion cyclotron resonance ($\omega = \Omega_H$). The used parameters for the calculation is shown in the figure, where r_p and r_w denote the plasma radius and the wall radius, respectively.

shown as a dashed line in Fig. 3.1. Since this resonance layer is located apart from the minority ion cyclotron resonance, it may give rise to electron heating. The high-field side launching of the fast wave corresponds to the case in the plug cell, where the transmitted fast wave propagates from the mirror point. Electron heating in the plug cell is favorable for formation of ion-confining potential for enhancement of the axial confinement.

When we distinguish the slow wave from the fast wave experimentally, polarization of the wave field is an important aspect. Figure 3.2 shows the power component of the left-circularly polarized wave fields, obtained with the same parameters as Fig. 3.1. Wave polarization is readily obtained by $jE_x/E_y = (n^2 - S)/(-D)$, where n is the refractive index ($n = (c/\omega)k$), $jE_x/E_y = -1$ in the case of right-circular polarization and $jE_x/E_y = 1$ in the case of left-circular polarization [14]. We note that wave fields are assumed to vary as $\exp[j(\omega t - \boldsymbol{k}\cdot\boldsymbol{r})]$. The fast wave is right-circularly polarized and the slow wave is left-elliptically-polarized at $\omega \sim \Omega_H$. Without minority ions (shown as a dotted line) the propagating mode is restricted to the fast wave in this frequency region, which consists of left-circularly polarized field (E_+) component $\sim$ 2 % and right-circularly polarized field (E_-) component $\sim$ 98 %. With ν_H = 10 %, E_+ component is enhanced drastically by the presence of the slow wave modes (S_1, S_2, S_3, ...) for $\Omega_{ii} \leq \omega \leq \Omega_H$, whereas E_+ component has 0 %$-$2 % of the wave energy for $\omega < \Omega_{ii}$ and $\omega > \Omega_H$, which is the region of the fast wave propagation. That is, the characteristics of the slow wave modes with higher radial orders shown in Figs. 3.1 and 3.2 are as follows : reflection and going backward from the ion-ion hybrid resonance layer, enhancement of a left-polarized field E_+, and approaching to the minority ion cyclotron resonance layer.

In the above description of polarization dependence, we neglect two aspects which affect enhancement of E_+ of the fast wave. The first one is the presence of the surface mode. The derivation of the dispersion relation of the fast wave provides two existing

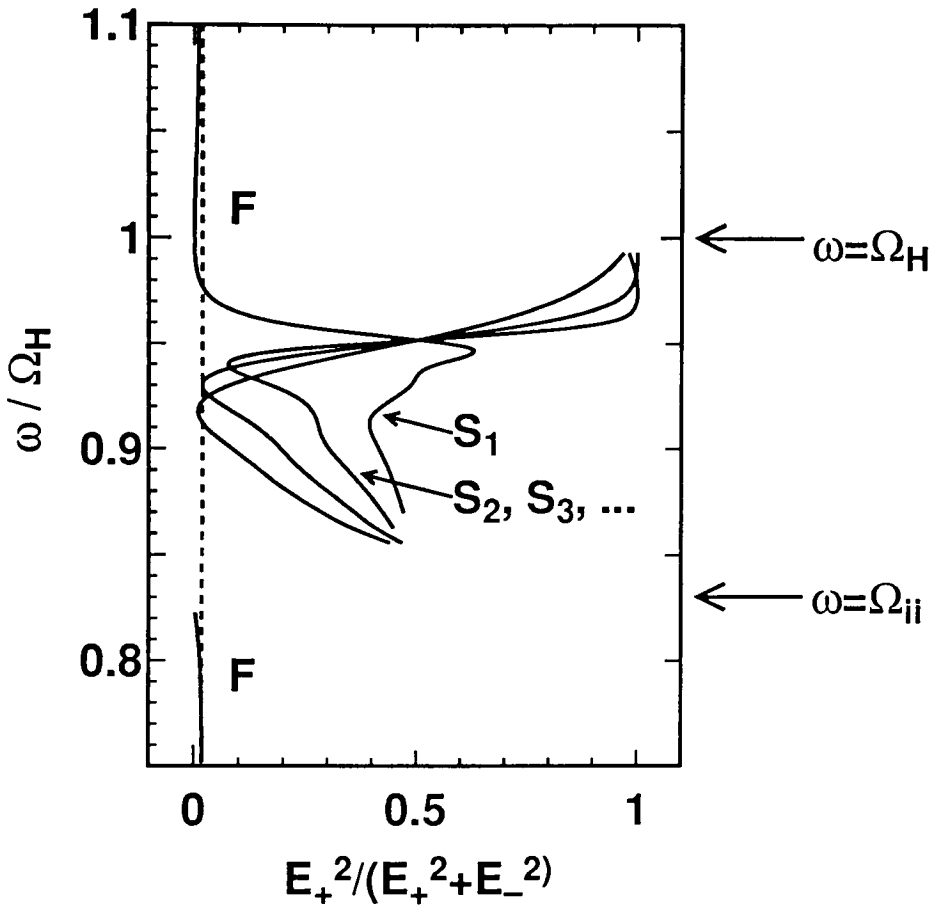

FIG. 3.2. Left-circularly polarized component of the propagating modes in the center of the cylindrical plasma. The used parameters for the plot of the solid lines are the same as in Fig. 3.1. The dashed line denotes the case without minority ions.

modes with different values of $k_\perp$, body mode and surface mode. Here we denote the corresponding $k_\perp$ as $k_{\perp 1}({k_{\perp 1}}^2 \sim 10\ \mathrm{m}^{-2})$ for the body mode and $k_{\perp 2}({k_{\perp 2}}^2 < -10^4\ \mathrm{m}^{-2})$ for the surface mode [12]. We take in Fig. 3.2, $n^2 = (c^2/\omega^2)({k_\parallel}^2 + {k_{\perp 1}}^2)$ to see the wave propagation near the center, where wave fields resonating with ions contribute to main plasma heating. When we take $n^2 = (c^2/\omega^2)({k_\parallel}^2 + {k_{\perp 2}}^2)$, the result will show that a wave field is linearly polarized, so that even for the fast wave propagation, a significant component ($\sim$ 50 %) of E_+ is involved in the edge region. The other aspect is enhancement of E_+ by the parallel thermal motion of ions [1]. We can introduce the effect of the parallel thermal motion of ions into the dielectric tensor, such as

$$S \rightarrow \sum_{\alpha=\mathrm{H,\ He}} \omega_{p\alpha}^2 \int \frac{f(v_\parallel)dv_\parallel}{{\Omega_\alpha}^2 - (\omega + j\epsilon - k_\parallel v_\parallel)^2}, \tag{3.2}$$

where ω_p is the plasma frequency, $v_\parallel$ the parallel velocity of ions, and ϵ is introduced in order to make the integral valid at $\Omega_\alpha - \omega + k_\parallel v_\parallel = 0$. For the first approximation, we obtain

$$\frac{{E_+}^2}{{E_+}^2 + {E_-}^2} = \frac{16}{16 + 25(\nu_H \Omega_H Z - \frac{4}{3})^2}, \tag{3.3}$$

where

$$Z = \int \frac{f(v_\parallel)dv_\parallel}{\Omega_\alpha - (\omega + j\epsilon - k_\parallel v_\parallel)}.$$

In our case, however, $k_\parallel v_\parallel$ is so small(by one or two orders) compared to ω and Ω_H that this effect is not influential on the result in Fig. 3.2.

3.3 Experimental setup

The HIEI tandem mirror is so-called "ICRF tandem mirror" experimental machine, that is, the tandem mirror operated only by mode-controlled ICRF. The configuration is purely axisymmetric with three cells, shown in Fig. 3.3. The central cell is 1.9 m in length and 0.25 m in radius, with a plug cell 0.5 m in length on both sides of the central

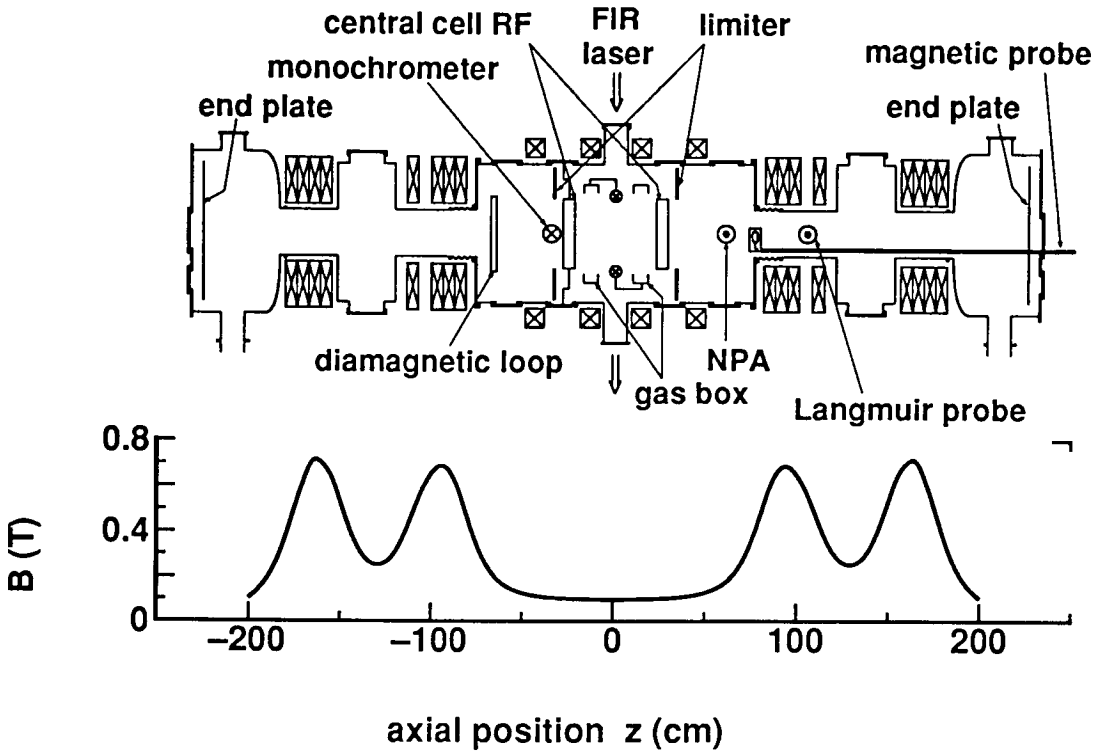

FIG. 3.3. Schematic view of the HIEI tandem mirror with its configuration of the magnetic field strength.

cell. Four limiters aligned axially in the central cell constrict the size of the plasma as large as 0.14 m in radius in the midplane. The magnetic field strength in the standard operation is 0.1-0.7-0.25-0.7 T (from the midplane of the central cell to the outer plug mirror point along the axis). The ponderomotive force produced by RF fields stabilizes the flute instability [15]. Axial confinement is improved by ion confining potential enhanced by RF in the presence of thermal barrier resulting from ponderomotive potential [4].

To initiate the plasma, mixed gas, including He (majority) and H (minority) with some ratios is stored in a gas tank in advance, and it is puffed into a gas box located in the midplane of the central cell. Pulsed ECH (Electron Cyclotron Heating) for 3 msec at 2.45 GHz follows immediately to ionize a part of the puffed gas up to $n_e \sim 10^{11}$ cm^{-3} After the start-up by ECH the central cell RF is injected from two antenna elements without Faraday shields. The set of the antenna elements, which is called a dual double half-turn antenna, is driven at a frequency $\omega/2\pi = 8$ MHz by two 250 kW amplifiers. The two antenna elements are located at $z = \pm 24$ cm, where z is distance from the midplane of the central cell along the magnetic axis. Rotating RF electromagnetic fields with a specific m number can be launched by mode control, i.e., by varying phase difference between two antenna currents [16]. The field rotation of $m = -1$ is favorable for the $m = -1$ fast wave launching, which is used in the experiments described later. In the region of $\omega/\Omega_{He} \sim 20$ the central cell RF propagates as the helicon wave, where efficient plasma production up to $n_e \sim 1 \times 10^{13}$cm^{-3} is realized. The launched wave goes on toward the mirror point, and, as B_0 increases along the magnetic axis, it encounters the ICRF region as the fast wave.

RF magnetic fields are measured using a magnetic probe, which consists of two small one-turn coils with 4 mm in diameter shielded electrostatically. Output RF signals provide the amplitude and phase of the radial and azimuthal components of RF magnetic fields

(B_r and B_θ, respectively) in cylindrical coordinates. Both the fast and slow wave modes have axial field components B_z. However, usually measurement of B_z is skipped, since measurements of B_r and B_θ reveal polarization of the wave fields, which gives us important information of propagating modes. In our case, since the experimental results indicate that $|B_z|$ is less than 20 % of $|B_\perp|$ in $r/r_p < 0.7$, $\boldsymbol{B}_+$ and $\boldsymbol{B}_-$ approximately reflect $\boldsymbol{E}_+$ and $\boldsymbol{E}_-$ electric fields, respectively. The magnetic probe is inserted from the end plate of the vessel, and it is movable axially and radially. Thus 2-D profiles of RF wave propagation are obtained, in particular, in the region of mode conversion.

Using this magnetic probe, we identify $k_{||}$ of a propagating wave, as mentioned below. The circularly polarized components of a propagating RF magnetic field take the forms

$$B_+ = B_r + jB_\theta, \; B_- = B_r - jB_\theta. \tag{3.4}$$

Here B_i varies with $\exp(j\phi_i)$, and the subscript i denotes $+$, $-$, r, or θ. The phase angle ϕ_i is expressed as $\phi_i = m\theta - k_{||i}z + \omega t$. We note here that "+" and "−" indicate the left-circularly polarized and right-circularly polarized components of a RF field, respectively, with respect to the direction of B_0. We divide Eq. 3.4 into real and imaginary parts, and obtain

$$B_\pm \cos\phi_+ = B_r \cos\phi_r \mp B_\theta \sin\phi_\theta \tag{3.5}$$

and

$$B_\pm \sin\phi_+ = B_r \sin\phi_r \pm B_\theta \cos\phi_\theta. \tag{3.6}$$

Using Eq. 3.6 divided by Eq. 3.5, we obtain the expressions for phase angles as

$$\tan\phi_\pm = \frac{\sin\phi_\pm}{\cos\phi_\pm} = \frac{B_r \sin\phi_r \pm B_\theta \cos\phi_\theta}{B_r \cos\phi_r \mp B_\theta \sin\phi_\theta}, \tag{3.7}$$

where B_i in Eqs. 3.4-3.7 indicates the wave field amplitude. If we choose one fixed radial and azimuthal position (which is determined by one pair of r and θ) and investigate

a wave field at a time t_0, then the phase angle of a detected RF field ϕ_i reflects $k_{||i}z$ component, where $k_{||i}$ is the parallel wave number of B_i. The fixed time t_0 is determined by the relative comparison with the phase of one antenna current, which produces RF electromagnetic fields detected by the magnetic probe. We finally derive $k_{||i}$ as a gradient of the axial profile of $k_{||i}z$. As complex scaler, the detected wave fields take the forms $B_r = 1/2(B_+ + B_-)$ and $B_\theta = 1/2j(B_+ - B_-)$, and the B_r loop gives us direct information on $k_{||}z$ as a sum, $B_+ + B_-$. In the region of fast wave propagation the B_+ component is detected with small amplitude, compared with the B_- component (e.g., $|B_+|/|B_-| \leq 0.2$), and $k_{||}z$ measured by the B_r loop approximately reflects that of B_-. In the region of mode conversion, however, B_+ component has significant amplitude and the measurements of $k_{||}z$ are made using both B_r and B_θ loops to obtain the values of $k_{||+}$ and $k_{||-}$ separately by Eq. 3.7.

A charge-exchange neutral particle energy analyzer (NPA) is used for the measurement of ion energy distribution and ion temperature. NPA in HIEI can determine ion temperature for each ion species separately, using electromagnetic and electrostatic deflection. It is located at $z = +60$ cm and measures the energy spectrum of ions which is in the midplane ($z = 0$), with the pitch angle around 45 °

3.4 Experimental results

3.4.1 Wave propagation in the regions of mode conversion

A stable and lower-density plasma is produced for observation of propagating modes. $k_{||}$ in the dispersion relation sensitively depends on plasma density, and smaller density fluctuations realize more rigorous $k_{||}$ measurements. The plasma parameters are as follows : $n_e \sim 1 \times 10^{12}\text{cm}^{-3}$ (measured by the far infrared (FIR) laser interferometer at $z = 0$),

density fluctuation level $\tilde{n}_e/n_e \leq 0.2$, ion temperature $T_i \sim 0.2$ keV, electron temperature $T_e = 15 - 25$ eV, and the mirror ratio R_m is set to be 7. Because of this low value of T_e, He is ionized as He^+ and the presence of He^{2+} is negligible. The net loading resistance of the plasma during the ICRF launching is approximately 0.3 Ω, and coupled RF power into the plasma P_{net} is 60−70 kW.

The experiments for investigation of mode conversion are performed in the condition with or without the resonance layers, i.e., the minority ion cyclotron resonance layer ($\omega = \Omega_H$) and the ion-ion hybrid resonance layer ($\omega = \Omega_{ii}$). The magnetic field strength B_m >0.53 T is required for the presence of the minority ion cyclotron resonance at $\omega/2\pi$ = 8 MHz, and $B_m > 0.60$ T for the ion-ion hybrid resonance in the case with $\nu_H = 7$ %, where B_m indicates the strength of the static magnetic field at the mirror point ($z = 95$ cm).

The concentration of the minority ion species ν_H is monitored through measurement of relative intensities of two atomic emission lines (HeI:587.6 nm, H_α:656.2 nm) in the central cell as ionization rates. Based upon the measured intensities of HeI and H_α in a one-ion-species plasma of He and H as a function of density, we can derive ν_H of the two-ion-species plasma for a partial pressure of H in the puffed gas ν_{puff}. In the range of our experimental parameters, ν_H is found to be larger than ν_{puff} by a factor of ~ 1.3 for $\nu_{puff} \geq 3$ %, whereas minority ions are always involved with $\nu_H = 1-4$ % for $\nu_{puff} \leq 3$ % due to the recycling H particles from the wall.

Wave propagation is investigated in the mode-conversion regions, where r_p is ~ 5.5 cm with $r_w = 7.0$ cm and the gradient of the magnetic field strength is relatively steep (~ 0.02 T/cm). The magnetic probe is scanned axially at $r/r_p = 0.16$ to observe wave propagation near the center of the plasma.

In the case of the low-field side launching wave measurement is performed in the central

cell region. In Figure 3.4(a) the axial profile of $k_{||}z$ is displayed in the case with neither the minority ion cyclotron nor ion-ion hybrid resonance layer in the whole region of the central cell. Note that the central cell RF is launched from the left side of this figure and that the mirror point is located at $z = 95$ cm. Thus the RF wave is incident from the low-field side for $z < 95$ cm. The spatial region of the measurement corresponds to $2.1 \leq \omega/\Omega_H \leq 3.3$. The profile shows a slightly positive gradient, indicating that $k_{||} > 0$ and the direction of the wave propagation is from the left to the right. The value of $k_{||}$ remains constant around 9 m^{-1}, obtained as a gradient in Figure 3.4(a). The dispersion relation of the fast wave in the cylindrical plasma model is derived theoretically as described in Sec. 3.2, and the calculated curve with the same plasma parameters as those of this experiment is plotted as the inset line for comparison. The measured profile roughly agrees with the theoretical one. The measurement of wave amplitude shows that B_- is 3-5 times larger than B_+. The wave propagation observed in this region is consistent with the fast wave feature.

Figure 3.4(b) shows the axial profile of $k_{||}z$ in the case with the minority ion cyclotron resonance but without the ion-ion hybrid resonance. The spatial region of this measurement corresponds to $0.94 \leq \omega/\Omega_H \leq 1.5$. The profile with a monotonic positive gradient is again obtained and the theoretical curve for the fast wave branch in the same condition is also given by the inset line. The monotonic profile is obtained even in the vicinity of the minority ion cyclotron resonance layer. The gradient of the experimental data suggests $k_{||} \sim 3$ m^{-1} The propagating mode observed in this case is the fast wave only and no resonance occurs, which yields the fact that effective minority ion heating is not expected in this regime.

Figure 3.4(c) demonstrates the wave propagation with both the minority ion cyclotron resonance and ion-ion hybrid resonance layers. The axial profiles of $k_{||+}z$ ($k_{||}z$ of B_+) and

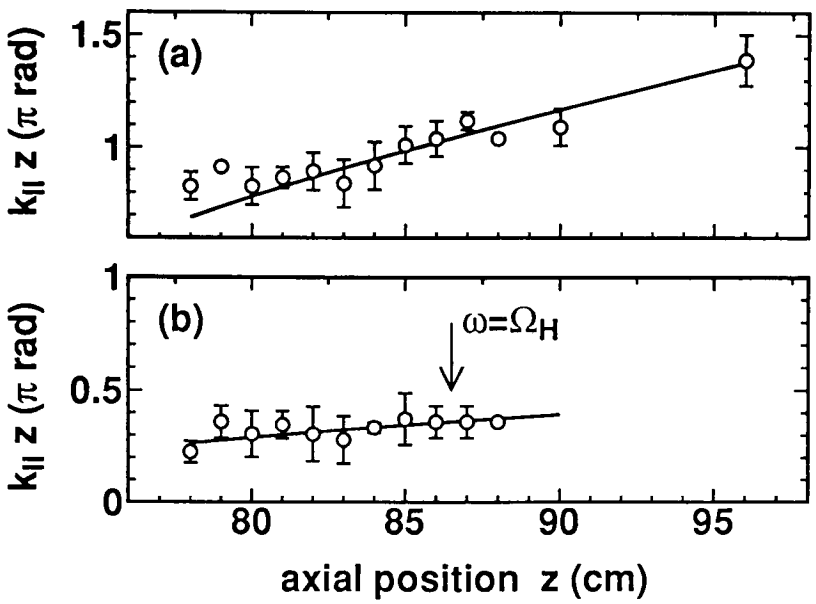

FIG. 3.4. (a) Axial profile of $k_{||}z$ in the central cell region without the ion-ion hybrid resonance and the minority ion cyclotron resonance. The maximum magnetic field strength B_m is set to 0.26 T with minority concentration $\nu_H = 13$ %, and RF signals are monitored at $r = 1$ cm. The solid line results from theoretical analysis using the dispersion relation of the fast wave in a cylindrical plasma with the same parameters as those in the experiment. (b) Axial profile of $k_{||}z$ with the minority cyclotron resonance only. $B_m = 0.58$ T, $\nu_H = 14$ %, and monitored at $r = 1$ cm. The solid line is the theoretical prediction for the fast wave branch in this condition.

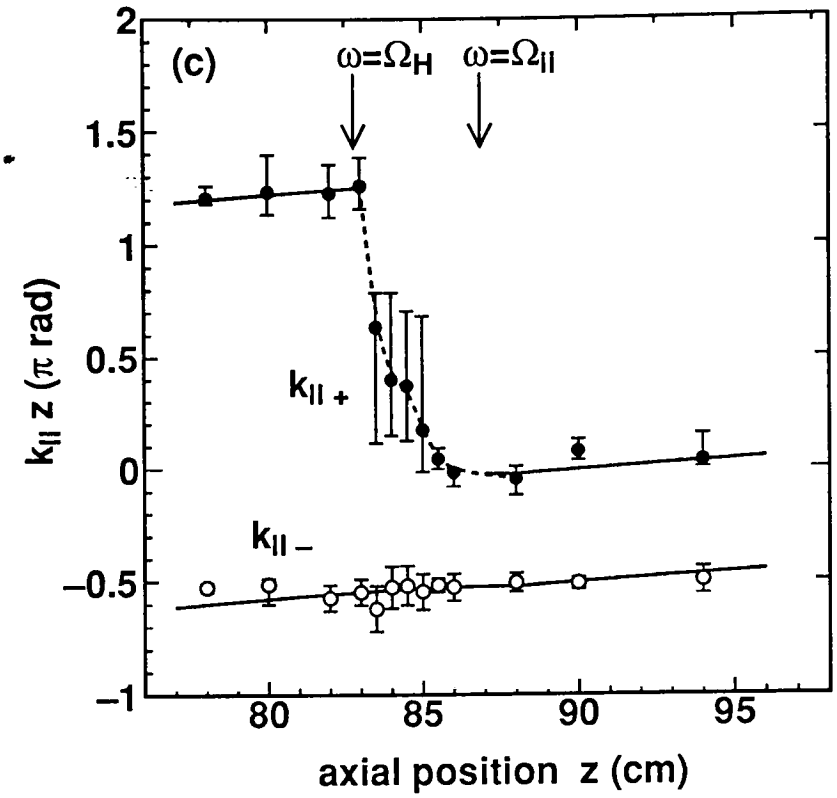

FIG. 3.4. (c) Axial profile of $k_{||}z$ of B_+ ($k_{||+}z$) and $k_{||}z$ of B_- ($k_{||-}z$) with the ion-ion hybrid resonance and the minority cyclotron resonance. B_m = 0.69 T, ν_H = 9.0 %, and monitored at r = 1 cm. The solid line shows the theoretical prediction for the fast wave branch in this condition, and the dashed line indicates the region where reflected waves are present propagating in the opposite direction.

$k_{\|-}z$ ($k_{\|}z$ of B_-) are displayed separately. The profile of $k_{\|-}z$ shows that $k_{\|-}$ ($\sim$ 2.0 m^{-1}) remains in a small positive value, and this right-polarized wave is a right going one, which is in the direction of the RF injection. This quantitatively agrees with the feature of the fast wave mode in this region which is predicted theoretically in Fig. 3.1. The profile of the $k_{\|+}z$ demonstrates a drastic difference from that of $k_{\|-}z$. In the region between the minority ion cyclotron resonance layer ($z \sim 82.5$ cm) and the ion-ion hybrid resonance layer ($z \sim 87$ cm) the gradient of the profile is negative, which indicates that the left-polarized wave propagates in the direction against the RF injection. This reveals the existence of reflected waves and the presence of cut-off layer near the ion-ion hybrid resonance layer. $|k_{\|+}|$ is found to be quite large in comparison with $|k_{\|-}|$ and, furthermore, $|k_{\|+}|$ increases with approach to the minority ion cyclotron resonance layer, which suggests some resonance phenomenon. These measured axial $|k_{\|}|$ profiles will be discussed in great details in Sec. 3.5 with the theoretical dispersion relation.

The role of the ion-ion hybrid resonance on wave propagation is examined by changing ν_H and moving the axial position of the ion-ion hybrid resonance layer. Horizontal bars in Fig. 3.5 show the axial regions of reflected wave propagation against the RF injection as a function of ν_H with corresponding positions of the minority ion cyclotron and ion-ion hybrid resonance layers. As ν_H is increased the ion-ion hybrid resonance layer becomes apart from the minority ion cyclotron resonance layer. The region of the reflected wave becomes broader up to $\nu_H = 14$ %, and it is consistent with the hatched region of the slow wave propagation predicted in Fig. 3.1.

Wave propagation in the case of the high-field side launching is investigated in the plug cell, where the central cell RF comes through the mirror point. Figure 3.6 displays the axial profile of $k_{\|}z$ in the case with both the ion-ion hybrid resonance and the minority cyclotron resonance layers. Except the region near the ion-ion hybrid resonance, the profile

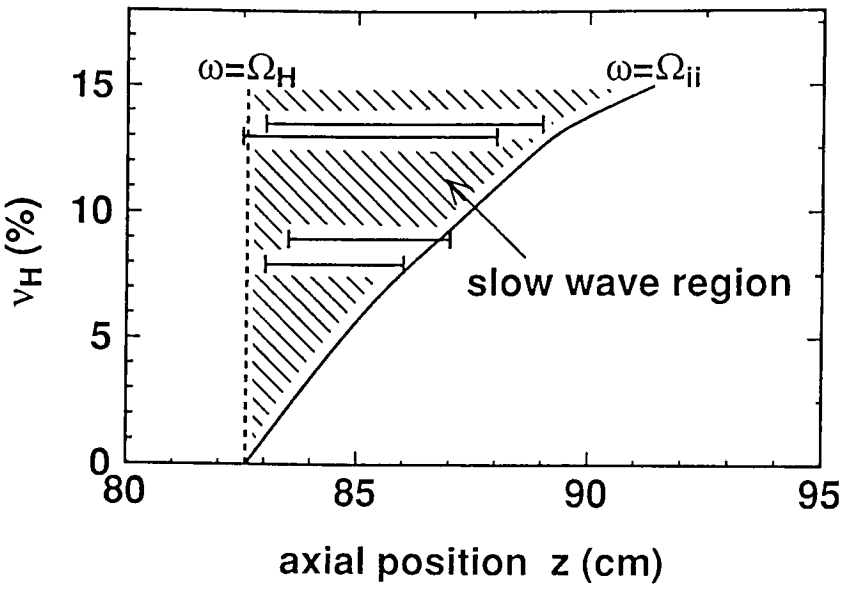

FIG. 3.5. Regions of the reflected wave (horizontal bars) as a function of ν_H with the positions of the corresponding minority ion cyclotron (dotted line) and the ion-ion hybrid (solid curve) resonance layers. $B_m = 0.69$ T and monitored at $r = 1$ cm. The hatched region indicates the predicted region of the slow wave propagation in the calculation of Fig. 3.1.

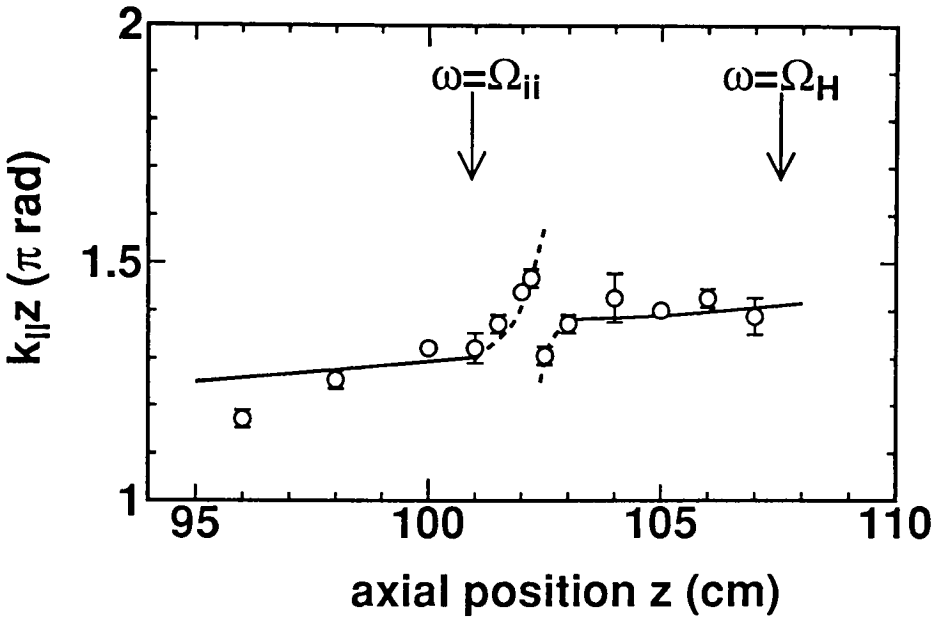

FIG. 3.6. Axial profile of $k_{||}z$ with the ion-ion hybrid resonance in the plug cell. B_m = 0.69 T, ν_H = 13 %, and monitored at r = 1 cm. The solid line is the theoretical prediction for the fast wave branch in this condition.

shows a slightly positive gradient, which is in good agreement of theoretical dispersion of the fast wave branch shown as an inset solid line. However, change of the profile is observed near the ion-ion hybrid resonance layer, where discontinuity of the profile with large $k_{||}$ is observed.

The axial shift of the region with large $k_{||}$ is examined by changing ν_H, shown in Fig. 3.7 as a hatched region, where the inset solid line indicates axial position of the ion-ion hybrid resonance layer. The axial shift observed experimentally agrees with change of the position of the ion-ion hybrid resonance layer up to $\nu_H = 15$ %. The region with large $k_{||}$ tends to emerge for $\omega \geq \Omega_{ii}$, which means that this wave resonance takes place just on or slightly beyond the ion-ion hybrid resonance layer. Figure 3.8 shows the change of the radial profile of B_z as a function of B_m. The ion-ion hybrid resonance layer is located near $z = 103$ cm in the case with $B_m = 0.69$ T and $\nu_H = 10$ %, as shown in Fig. 3.7. When the ion-ion hybrid resonance layer is apart from $z = 103$ cm (shown as open circles or closed squares), the profile shows a peak for $0.45 < r/r_p < 0.55$, while B_z becomes small below the noise level for the magnetic probe measurement in the bulk region for $r/r_p < 0.70$. This experimental fact indicates that the wave energy of the electromagnetic wave converts into another wave energy, which might be carried by an electrostatic wave.

3.4.2 Ion heating via mode conversion

As described so far, left-polarized waves were observed which propagate in the direction opposite to the launched wave, and it vanishes near the minority ion cyclotron resonance layer. The value of $|k_{||+}|$ was found to be quite large and the polarization is in the same sense as the ions, which suggests that the wave is resonant with the minority ions. In this subsection we demonstrate minority ion heating due to the change of the wave propagation between the minority ion cyclotron and ion-ion hybrid resonance layers.

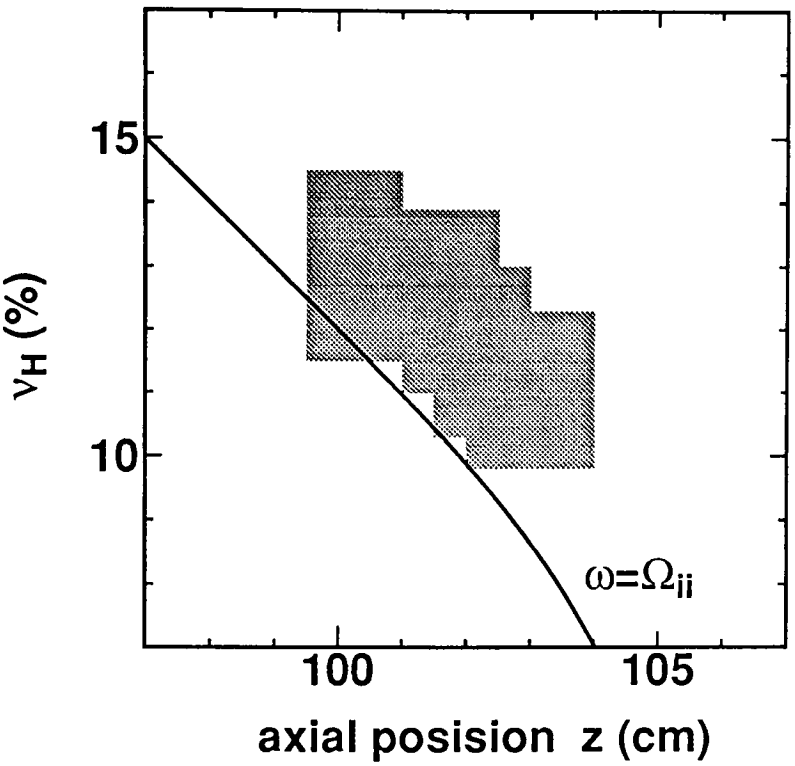

FIG. 3.7. The position where $k_{||}$ of the wave becomes a maximum in the plug cell versus ν_H (hatched region). The solid line gives the position of the ion-ion hybrid resonance layer calculated for a given ν_H.

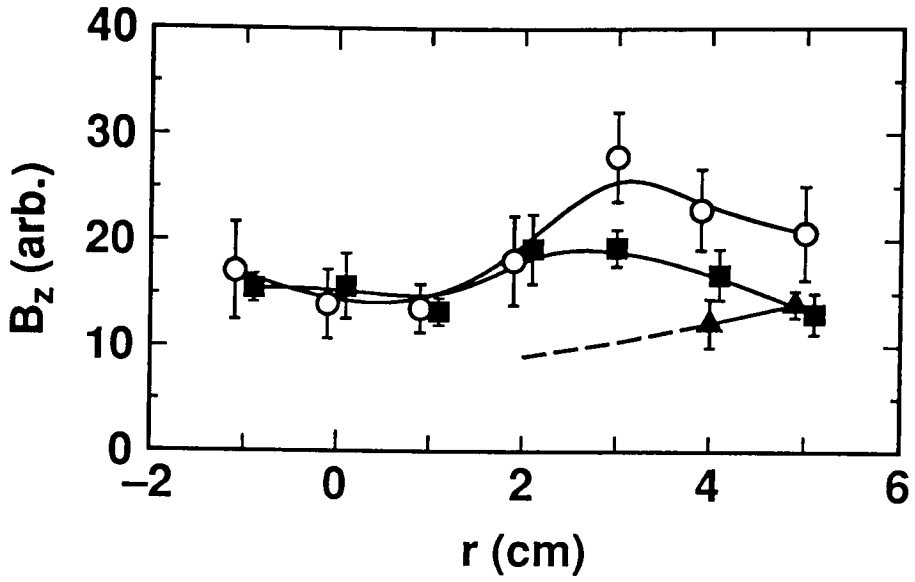

FIG. 3.8. Radial profiles of the wave magnetic field B_z at $z = 103$ cm for $B_m = 0.69$ T and $\nu_H = 1.1$ % (open circles), $B_m = 0.47$ T and $\nu_H = 13$ % (closed squares), and $B_m = 0.69$ T and $\nu_H = 13$ % (closed triangles). The noise level of B_z is ~ 10 in arbitrary units in the figure.

As the mirror ratio is increased over 7, the plasma turns into higher-density and relatively less stable mode. A higher beta plasma is expected in this operation. The plasma parameters are as follows : $n_e = 2 - 3 \times 10^{12}\mathrm{cm}^{-3}, \tilde{n}_e/n_e \leq 0.5, T_i \geq 0.2$ keV (depending on several parameters mentioned later), $T_e = 20 - 25$ eV, and the mirror ratio is 7−10. There is no apparent increase in T_e in the presence of the resonance layers, leading to the fact that electron heating by the ICRF waves can be negligible in the central cell. Possibility of electron heating will be discussed in Sec. 3.5.

Figure 3.9 shows the energy distributions of the minority (H) ions measured by NPA. In Fig. 3.9(a), displayed distributions are obtained for different values of the magnetic field strength. The signal in the case with the minority ion cyclotron resonance and without the ion-ion hybrid resonance shows the perpendicular ion temperature at $z = +60$ cm $T_{i\perp}$ remains around 0.13 keV The efflux in high energy regions (≥ 0.9 keV) is so small that scattering of the experimental points is present. The signal in the case with both the minority ion cyclotron and ion-ion hybrid resonance layers exhibits significant minority ion heating, and $T_{i\perp}$ rises by a factor of 2 from the case with the minority ion cyclotron resonance only. The high energy efflux of minority particles is quite large. When neither the ion-ion hybrid resonance nor the minority ion cyclotron resonance are present, $T_{i\perp}$ remains around 0.10 keV or less. As for the energy spectrum of majority (He) ions in the case with both the minority ion cyclotron resonance and ion-ion hybrid resonance layers, we obtain an approximate value of $T_{i\perp} = 0.10$−0.13 keV. This ambiguity of $T_{i\perp}$ of He^+ results from the poor stripping efficiency of He fast neutrals in NPA. Figure 3.9(b) shows the energy distributions of minority (H) ions with and without puffing of the minority ions. In the case with $\nu_{puff} = 0$ %, minority ions are provided as recycling particles from the vessel wall with $\nu_H \sim 1$ %. No significant heating is found in the energy spectrum. In the case with $\nu_{puff} = 4.5$ % ($\nu_H \sim 5.7$ %), $T_{i\perp}$ rises significantly in comparison with the

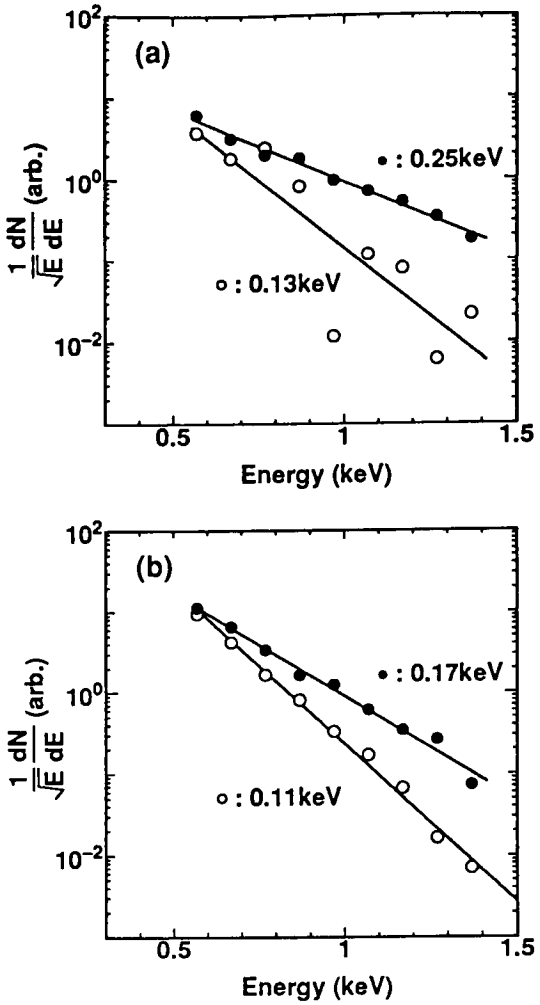

FIG. 3.9. (a) Energy distributions of minority (H) ions monitored by NPA. The solid circles represent the case with the ion-ion hybrid resonance and the minority ion cyclotron resonance (B_m = 0.69 T, $n_e = 2.3 \times 10^{12}\text{cm}^{-3}$). The open circles represent the case with the minority ion cyclotron resonance only (B_m = 0.60 T, $n_e = 2.7 \times 10^{12}\text{cm}^{-3}$). ν_H = 7.9 %, P_{net} = 80–90 kW, and R_m = 7.1. (b) Energy distributions of minority ions monitored by NPA. The open circles represent the case for ν_{puff} = 0 % (ν_H = 1.1 %, R_m = 7.1, $n_e = 2.7 \times 10^{12}\text{cm}^{-3}$). The closed circles represent the case for ν_{puff} = 4.5 % (ν_H = 5.7 %, R_m = 10.4, $n_e = 2.7 \times 10^{12}\text{cm}^{-3}$). P_{net} = 60–70 kW and B_m = 0.69 T.

case of no minority puffing. As the ratio of minority in puffing gas is increased further up to 30 %, $T_{i\perp}$ gradually decreases below 0.13 keV. This result shows that the efficiency of mode conversion depends on minority concentration. In other words, there is the most efficient distance between the ion-ion hybrid resonance and minority ion cyclotron resonance layers. The numerical result of a 2-D ICRF code [11, 17] shows that the rate of the mode conversion is maximized at $\nu_H = 4-6$ %. The experimental condition which yields the highest $T_{i\perp}$ value agrees with the optimum minority concentration predicted by the numerical result.

Figure 3.10 shows the dependence of $T_{i\perp}$, the central cell beta $\beta_\perp$, and the heating quality factor on P_{net}. Heating quality factor is defined as $n_e \ T_{i\perp}/P_{net}$. In the case of the maximum input power ($P_{net} \sim 80$ kW) $T_{i\perp}$ is 0.26 keV with $n_e \sim 2.7 \times 10^{12}\mathrm{cm}^{-3}$ As P_{net} is increased, $\beta_\perp$ increases up to 1.7 % and heating quality factor is slightly enhanced without degradation.

3.4.3 Electron heating via mode conversion

Wave propagation suggests occurrence of some resonance near the ion-ion hybrid resonance layer in the plug cell. The ion-ion hybrid resonance layer is apart from the minority ion cyclotron resonance layer in the presence of sufficient fraction of minority ions, so that this resonance is not associated with ion heating.

Figure 3.11 shows $k_{||}$ and T_{ep} near the ion-ion hybrid resonance layer as open circles. $k_{||}$ is derived from the profile of $k_{||}z$ by the magnetic probe measurement. The region with large $k_{||}$ is localized in the vicinity of the layer. T_{ep} with the ion-ion hybrid resonance increases near the layer than that without it, which shows constant profile through the region of the measurement.

Figure 3.12 displays T_{ep} and T_{ec} as a function of ν_H. In the presence of the minority

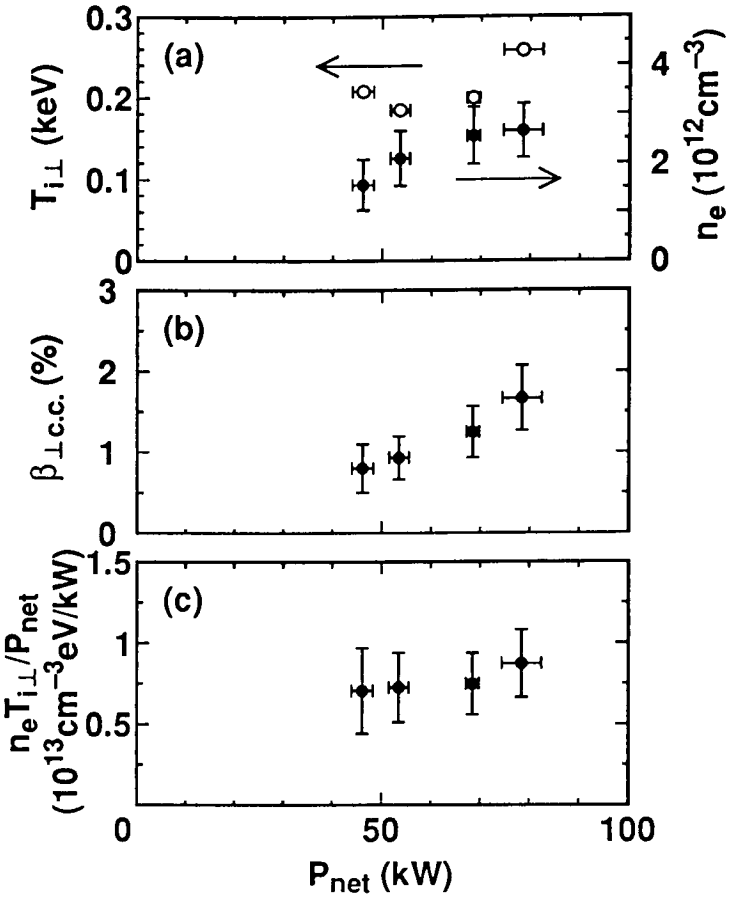

FIG. 3.10. Variation of $T_{i\perp}$, $\beta_\perp$ in the central cell, and heating quality factor with P_{net}. $B_m = 0.69$ T, $R_m = 9.4$, and $\nu_H = 8.7$ %.

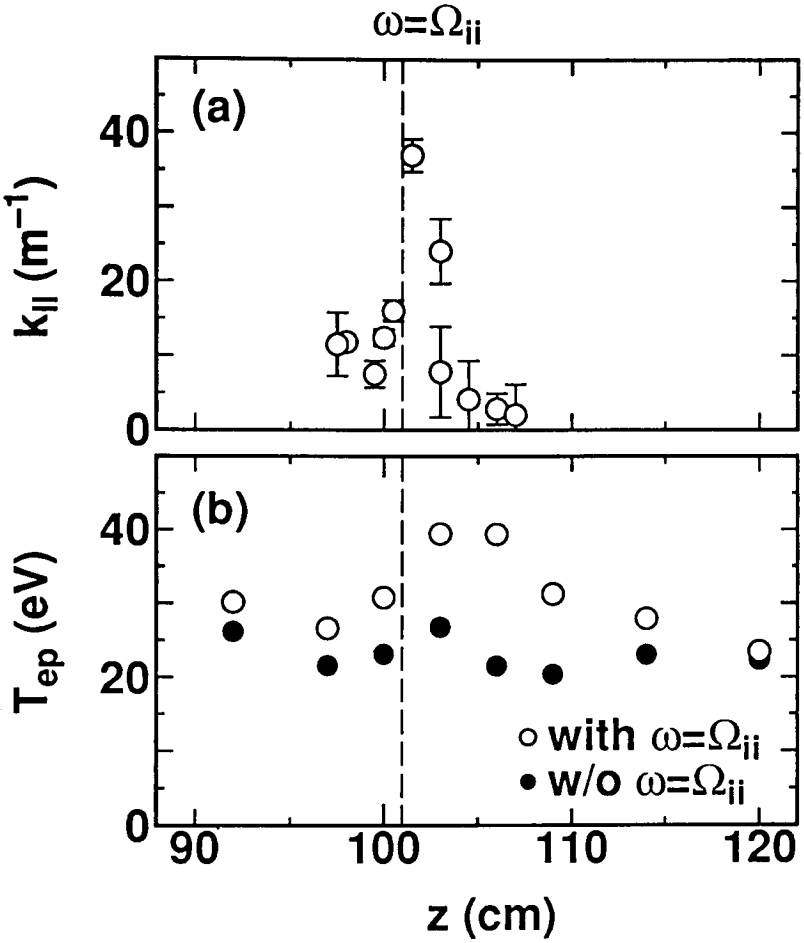

FIG. 3.11. (a) $k_{||}$ of the wave near the ion-ion hybrid resonance layer in the plug cell versus z for $B_m = 0.72$ and $\nu_H = 12$ %. (b) Plug electron temperature T_{ep} versus z for $B_m = 0.72$ T (with the ion-ion hybrid resonance, open circles) and for $B_m = 0.47$ T (without the ion-ion hybrid resonance, closed circles).

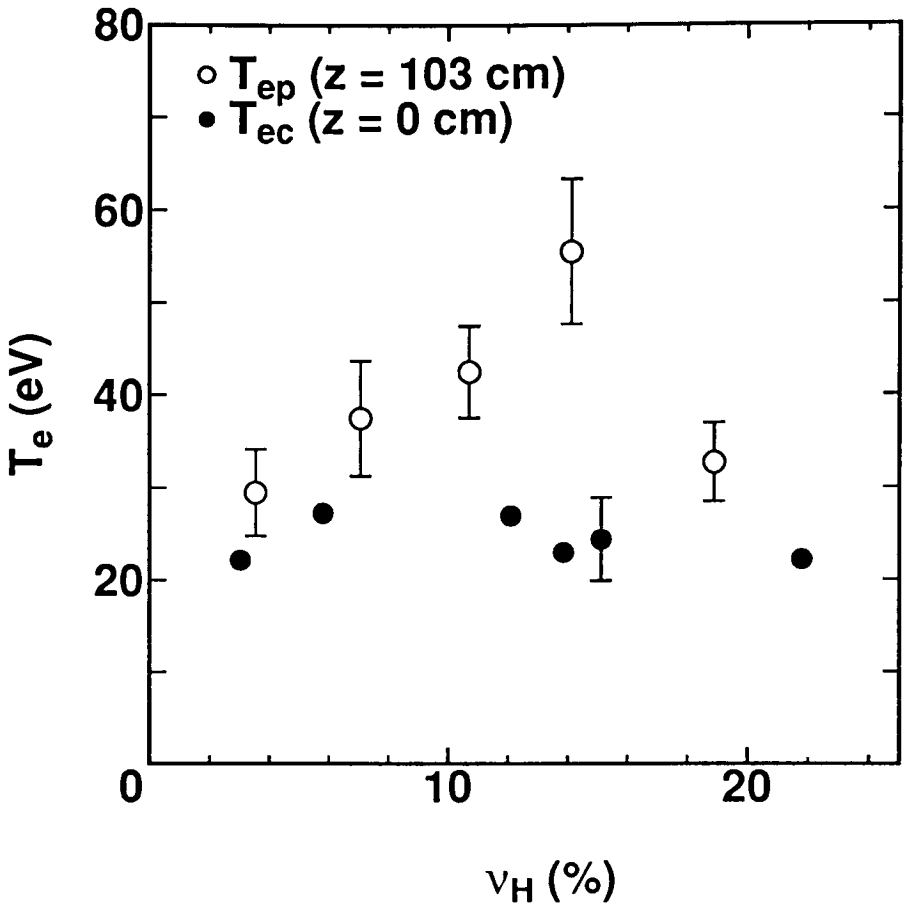

FIG. 3.12. Electron temperature in the plug cell T_{ep} at $z = 103$ cm and in the central cell T_{ec} at $z = 0$ cm as a function of ν_H.

ion, T_{ep} increases, whereas T_{ec} remains constant. T_{ep} is more than 40 eV for $10 < \nu_H < 15$ %, where measuring point $z = 103$ cm is located in the downstream from the ion-ion hybrid resonance to the plug cell midplane. For $\nu_H > 15$ % rise of T_{ep} is not observed since the ion-ion hybrid resonance layer is not present in the plug cell. The increase of T_{ep} with ν_H up to 15 % suggests the importance of some distance between the ion-ion hybrid resonance and the minority ion hybrid resonance layers for electron heating.

3.5 Discussions

The dispersion relation of a cylindrical homogeneous plasma shown in Fig. 3.1 describes the process of ion heating via mode conversion. We note that the wave propagating into the region of the close pair of cut-off and resonance layers may be transmitted, reflected or absorbed and contribute to minority ion heating. Such flow of the wave energy is as follows : excitation in the low-field side $\rightarrow$ F $\rightarrow$ S_1 $\rightarrow$ the ion-ion hybrid resonance layer $\rightarrow$ S_2, S_3, ... $\rightarrow$ the minority ion cyclotron resonance layer. The measurements of wave propagation reveal the features of the propagating modes. Figure 3.4(c) shows directly the propagating modes in the mode conversion region and the values of $k_{||}$ obtained as gradients of the experimental data are shown in Fig. 3.13(a) with the dispersion relation of Fig. 3.1 with $\nu_H = 9$ %. Here, open triangles represent $k_{||-}$, and open and closed circles represent $k_{||+}$ of the transmitted waves and $k_{||+}$ of the reflected waves, respectively. The fast wave branch in Fig. 3.1 is shown as a solid curve, and the hatched region indicates propagation of the slow wave modes. The experimental points of $k_{||-}$, which show the propagation of the right-circularly polarized field in the direction of the incident RF with a small value of $|k_{||}|$, is well consistent with the propagation of the fast wave mode predicted in the cylindrical plasma model. The axial profile of $k_{||+}$ shows the propagation of the left-circularly polarized wave in the direction opposite to the

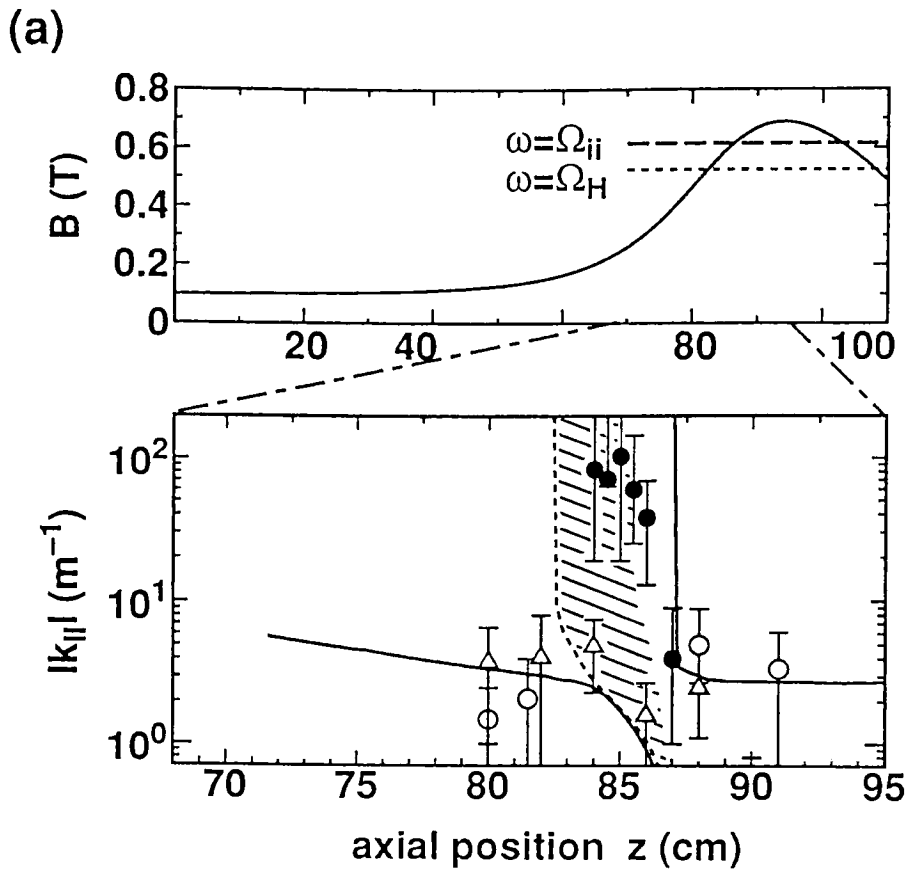

FIG. 3.13. (a) Axial dependence of measured $k_{||}$ in Figure 3.4(c) and theoretical mode branches with the profile of the static magnetic field strength. The open triangles indicate $k_{||}$ of transmitted right-circularly polarized wave (B_-), and the open and the closed circles indicate $k_{||}$ of transmitted and reflected left-circularly polarized wave (B_+), respectively. The solid lines denote theoretical branches of F and S_1 in Fig. 3.1. The hatched region corresponds to the slow wave modes (S_2, S_3, ...). Note that the ICRF wave (the m = -1 fast wave) is launched at $z = \pm 24$.

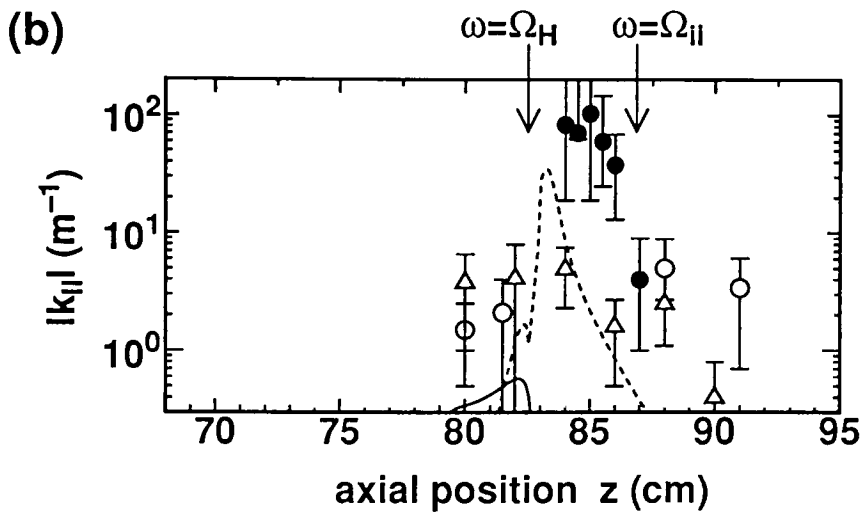

FIG. 3.13. (b) Axial dependence of measured $k_{||}$ and mode branches at $r = 0.9$ cm obtained by 2-D ICRF code [17]. The solid curve indicates the right-circularly polarized wave (E_-) propagating to the right side, and the dashed curve indicates the left-circularly polarized wave (E_+) going to the left side. The used parameters in the code calculation are as follows : $m = -1$, $B_m = 0.7$ T, $R_m = 1.7$, $\nu_H = 10$ %, $n_e = 5 \times 10^{12}\text{cm}^{-3}$, plasma radius = 5.5−6.5 cm in the mode conversion region, and the wall radius = 10 cm.

incident RF, with a large value of $|k_{||}|$ increasing as the wave approaches to the minority ion cyclotron resonance.

This feature qualitatively agrees with the dispersion relation of the slow wave shown in Figs. 3.1 and 3.2. From the values of $|k_{||+}|$ the detected waves are found to be the slow wave modes with higher radial orders. Outside the mode conversion region relatively small fraction of signals is detected as a left-circularly polarized field. It is probably a small part of the energy of the fast wave mode. $k_{||-}$ and $k_{||+}$ for $\omega < \Omega_{ii}$ and $\omega > \Omega_H$ represent $k_{||}$ of the fast wave.

In the plug cell region, the fast wave propagates from the high-field side of the ion-ion hybrid resonance, and electron heating is observed with different wave propagation from the case in the central cell. The region with large $k_{||}$ is localized in the narrow region in the vicinity of the ion-ion hybrid resonance layer. Furthermore, electromagnetic component of the propagating wave almost diminishes in that region, which suggests mode conversion into an electrostatic mode. An electrostatic wave with large $k_{||}$ and possibly with large $E_{||}$ is likely to resonate with electrons through Landau damping. The observation strongly indicates the close relationship between change of wave propagation and electron heating. Detailed mechanism of mode conversion into the electrostatic wave and effects of electron heating on ion-confining potential will be discussed in Chap. 5.

While there are gradients of B_0 and n_e in the actual experimental conditions, the calculated dispersion relation in Fig. 3.13(a) includes no effects of the longitudinal inhomogeneity. The Wentzel, Kramers, Brillouin (WKB) approximation might break down for waves with small $k_{||}$. In terms of energy flow into another mode via mode conversion, more explicit analysis is required rather than the WKB approximation. Furthermore, a slab model is used as a radial density profile in the previous model, which is different from a diffuse density profile observed in the experiment. We use a 2-D ICRF code [17]

to obtain the dispersion curves in a bounded inhomogeneous plasma so as to estimate the effects resulting from such discrepancies. In this numerical code a cold plasma bounded by conducting walls in cylindrical geometry is assumed and calculation is performed by the finite element method. It can deal with the inhomogeneity in both radial and axial directions and the power absorption by introducing collisional effects in the dielectric tensor. The configuration of magnetic fields is set to a simple mirror so that obtained results represent the wave propagation in the central cell. The results of the calculation are shown in Fig. 3.13(b), where the solid line shows $k_{||-}$ of the transmitted wave, and the dashed line shows $k_{||+}$ of the reflected waves. In this calculation we assume a smaller mirror ratio (= 1.7) than those in the experiments, since a larger number of lattices ($\sim$ 40) in the region of close resonance-cutoff pair would make it possible to simulate the mode-conversion phenomena rigorously with higher spatial resolution. The plasma radius is set to 5.5–6.5 cm in the mode-conversion region with r_w = 10 cm. The radial profile of the right-polarized wave is approximately consistent with the feature of the measured B_- profile. The resolution of $k_{||}$ measurement is $\sim$ 1 m^{-1}, and it is difficult to compare the measured $k_{||}$ values with the calculated ones (0.3–0.6 m^{-1}) for the right-polarized wave. These calculated small values reflect the presence of the standing wave which consists of the transmitted and reflected fast waves. The profile of the left-polarized wave, which shows propagation of a reflected wave, indicates a qualitative agreement with the measured B_+ within several factors. The presence of the reflected wave coincides with an increase in the power absorption in the calculations. That is, in the case of a one-ion-species (He) plasma, we find no propagation of reflected waves from the vicinity of the ion-ion hybrid resonance and the power absorption is low by one order from the case of a two-ion-species plasma with $\nu_H = 10 - 20$ %. We find some discrepancy between the theoretical curve and the experimental points in the axial direction. It could be due to

the difference between the actual and calculated values of the static magnetic field. For instance, 5−10 % decrease of the calculated values will cause the shift of the theoretical curves to the right by 1−2 cm, and in such a case we could find a better qualitative agreement. The above results of the 2-D calculation support the derivation of the dispersion relation in the homogeneous cylindrical plasma model so as to explain the experimental results.

Here additional description on connection between physical and mathematical points of view follows in order to reinforce the mode conversion phenomena predicted in the WKB model (Fig. 3.1 and Fig. 3.13(a)) and displayed in the numerical result of the 2-D ICRF code (Fig. 3.13(b)). In general, linear mode conversion takes place where two or more different modes coalesce at a certain set of wavenumber and frequency values. Wave energy of each wave, which oscillates a plasma at that point, may be transferred into another wave that is excited by the oscillated plasma. In a mathematical point of view, a linear differential equation is probably the best analytical expression to describe the whole process of mode conversion in an inhomogeneous plasma. Some typical types of the equations are known such as the Standard Equation and the Tunneling Equation which have a characteristic of preserving wave energy throughout the process [18], and dispersion relations in some simple cases are reduced to one of these differential equations through the inverse Fourier transform ($k \rightarrow -jd/dz$). An asymptotic solution for each mode can be obtained apart from the mode conversion point, and they corresponds to the branches of the dispersion relation in the WKB approximation (like the ones expressed in Fig. 3.1 and Fig. 3.13(a)). In the vicinity of the mode conversion point, where usually singularity is present, such a differential equation is frequently solved via the matched asymptotic expansion or other alternative techniques. However some complicated dispersion relations, among which a case in a hot plasma with thermal effects is well known, cannot be

converted into such differential equations, so that it is impossible to obtain an analytical solution. In our case, analysis with reduced differential equations have been skipped and more rigorous calculation has been performed numerically by the 2-D ICRF code that can deal with inhomogeneity which cannot be dealt with an analytical differential equation.

We should mention the possibility of mode conversion into the ion Bernstein wave like in tokamaks. Thermal effects give rise to a possible branch of the ion Bernstein wave near the ion-ion hybrid resonance. If some energy of the fast wave converts into that of the ion Bernstein wave, it might heat ions to some extent. However, conversion into this electrostatic mode could be neglected since $k_\perp \rho$ is less than 0.11 ($\ll 1$) in our experimental condition ($k_\perp \sim 40$ m^{-1} and the H-ion Larmour radius $\rho \sim 0.25$ cm at the ion-ion hybrid resonance).

When the ion-ion hybrid resonance is present and the mode conversion into the slow wave mode occurs, significant minority ion heating is observed, as shown in Fig. 3.9 and Fig. 3.10. Effects of energy transfer from the other heated ions (He^+ or some impurity ions) should be ruled out by the longer energy relaxation times with He and other impurities than the energy confinement time ($\sim 0.5-1$ msec).

As mentioned in Sec. 3.2, E_+ component of the fast wave is so small in the center. On the edge, however, a significant fraction of the wave energy is present as left-circularly polarized fields, which could transfer their energy to the ions. We apply the well known condition for the cyclotron resonance $\omega - k_{||} v_{||} = \omega_{ci}$ to our case, where $v_{||}$ is the parallel thermal velocity of the ions. $k_{||}$ is assumed to be 3 m^{-1} for the fast wave, and bulk minority ions have $v_{||} \leq 1.3 \times 10^5$ m/sec, which corresponds to parallel ion energy ≤ 0.1 keV The resonance condition becomes $\omega - \Omega_H \leq 3.3 \times 10^5$ sec^{-1}, which corresponds to the axial resonant width ~ 0.13 cm. In comparison, in the case of the slow wave ($k_{||} \sim 20$ m^{-1}), the resonant width is found to be ~ 0.8 cm. Energy absorption from the fast

wave is much smaller due to low thermal velocity of ions in our experiments. Fig. 3.9(b) indicates such tendency clearly. In the case of $\nu_H = 1.1$ %, damping of the fast wave would be the dominant term due to the poor efficiency of the mode conversion, and no effective heating is observed. In the case of $\nu_H = 5.7$ %, damping of the mode-converted slow wave would be dominant [11] and significant minority heating is observed.

It is found that $k_{||}$ of the detected slow wave is so large that it could possibly resonate with electrons with $T_e = 20 - 25$ eV through electron Landau damping (ELD) or electron transit-time damping (ETTD) [3]. However no significant electron heating is observed in the experiment. Stix dealt with ELD and ETTD of the fast wave [3], and a simple method for evaluation of wave damping was derived. Wave damping rate γ is defined as the power absorption P_{abs} divided by the wave energy density W We modify the form of W for the case of the slow wave, such as

$$W \sim \frac{5}{2\pi} \frac{4\pi n_i m_i c^2}{B^2} |E_y|^2, \tag{3.8}$$

where n_i is the ion density, m_i the ion mass, and B the static magnetic field. Using the form of P_{abs} given as a total absorption of ELD and ETTD [3], wave damping rate is obtained as $\gamma = P_{abs}/W \sim 25$ sec^{-1}. $\gamma^{-1}(\sim 40$ msec) is longer than the particle confinement time ($\tau_p \sim 1$ msec) in our case by more than one order. τ_p is not enough to observe such kinds of electron heating.

As for heating efficiency, the heating quality factor is $0.5-1.0 \times 10^{13}$ cm^{-3} eV/ kW up to $P_{net} = 80$ kW. The dependence on P_{net} indicates the further increase in the heating efficiency with P_{net}. This result suggests the possibility that more RF input power could give rise to further minority heating attained by this heating configuration in larger mirror machines. Unlike tokamaks, incident power of ICRF waves is used in plasma production and magnetohydrodynamic stabilization as well as ion heating in our experiments, and heating efficiency of this configuration will be satisfactory for practical use in the future.

3.6 Conclusion

In conclusion, we have shown the direct measurement of mode-converted waves in a longitudinally inhomogeneous magnetic field and ion heating via mode conversion which can provide good efficiency as a heating method in a dense two-ion-species plasma.

In the case of the low-field-side launching of the fast wave in a two-ion-species plasma, two propagating modes have been observed. One is the fast wave, which propagates in the whole range of the magnetic field strength. The other one is the slow wave, which is present between the minority ion cyclotron resonance and ion-ion hybrid resonance layers, and propagates in the direction opposite to the fast wave. According to the $k_{||}$ measurement, $|k_{||}|$ of the slow wave increases as it approaches to the minority ion cyclotron resonance, which indicates that the slow wave modes are close to the resonance condition. This shows that the m = -1 fast magnetosonic wave propagating from the low-field side converts into the m = -1 slow ion-cyclotron wave via reflection near the ion-ion hybrid resonance layer. Then the slow wave propagates toward the low-field side, approaching to the minority ion cyclotron resonance. These experimental results are both qualitatively and quantitatively consistent with the theory of the cylindrical uniform plasma model and with 2-D calculation based on a mirror geometry.

In the case of the high-field-side launching, the fast wave converts into an electrostatic wave, which is verified by the diminishing of the electromagnetic component, and resonates with electrons in the plug cell with observed large $k_{||}$. The change of the wave propagation is localized in the vicinity of the ion-ion hybrid resonance, so that there might be some new branch of the electrostatic mode near the ion-ion hybrid resonance. Significant minority ion heating and electron heating incidental to the mode conversions have been observed. In the presence of the slow wave mode, ion temperature measured by NPA increases up

to 0.26 keV by a factor of 2 with respect to the case without the ion-ion hybrid resonance. The absence of the ion-ion hybrid resonance produces no significant increase in minority ion temperature, which strongly suggests that the ion-ion hybrid resonance layer plays an critical role on mode conversion process. The condition of the efficient ion heating corresponds to the presence of the slow wave, which is the evidence of ion heating via mode conversion. In the plug cell electron heating occurs with the change of the wave propagation near the ion-ion hybrid resonance. These discrete mode conversions are quite favorable for simultaneous ion heating in the central cell and electron heating for formation of ion-confining potential by one excitation of the fast wave in the central cell.

References

[1] A. Bers (ed.), IEEE Trans. Plasma Sci. PS-**12** (1984) no.2 (Special issue on RF Heating and Current Generation).

[2] J. Hosea, S. Bernabei, P Colestock, S. L. Davis, P. Efthimion, R. J. Goldston, D. Hwang, S. S. Medley, D. Mueller, J. Strachan, and H. Thompson, Phys. Rev. Lett. **43** (1979) 1802.

[3] T. H. Stix, Nucl. Fusion **15** (1975) 737.

[4] Y. Yasaka, M. Miyakita, S. Kimoto, H. Takeno, and R. Itatani, in *Plasma Physics and Controlled Nuclear Fusion Research,* (IAEA, Vienna, 1991), Vol.2, p.725.

[5] N. Hershkowitz, B. A. Nelson, J. Johnson, J. R. Ferron, H. Persing, C. Chan, S. N. Golovato, J. D. Callen, and J. Woo, Phys. Rev. Lett. **55** (1985) 947, J. R. Ferron, R.

Goulding, B. A. Nelson, T. I. Intrator, E. Y. Wang, G. Severn, N. Hershkowitz, D. Brouchous, J. Pew, R. A. Breun, and R. Majeski, Phys. Fluids **30** (1987) 2855.

[6] D. Smith, K. Brau, P Goodrich, J. Irby, M. E. Mauel, B. D. McVey, R. S. Post, E. Sevillano, and J. Sullivan, Phys. Fluids **29** (1986) 902.

[7] M. Inutake, M. Ichimura, H. Hojo, Y. Kimura, R. Katsumata, S. Adachi, Y. Nakashima, A. Itakura, A. Mase, and S. Miyoshi, Phys. Rev. Lett. **65** (1990) 3397.

[8] D. R. Roberts and N. Hershkowitz, Phys. Fluids B **4** (1992) 1475.

[9] R. B. White, S. Yoshikawa, and C. Oberman, Phys. Fluids **25** (1982) 348.

[10] C. N. Lashmore-Davies, V Fuchs, and R. A. Cairns, Phys. Fluids **28** (1985) 1791.

[11] Y. Yasaka, H. Takeno, A. Fukuyama, T. Toyoda, M. Miyakita, and R. Itatani, Phys. Fluids B **4** (1992) 1486.

[12] D. R. Roberts, N. Hershkowitz, and J. A. Tataronis, Phys. Fluids B **2** (1990) 787.

[13] W. P. Allis, S. J. Buchsbaum, and A. Bers, *Waves in Anisotropic Plasmas* (MIT Press. Cambridge, Mass., 1963).

[14] T. H. Stix, *The Theory of Plasma Waves* (McGraw-Hill, New York, 1962).

[15] Y. Yasaka and R. Itatani, Phys. Rev. Lett. **56** (1986) 2811.

[16] Y. Yasaka, R. Majeski, J. Browning, N. Hershkowitz, D. Roberts, Nucl. Fusion **28** (1988) 1765.

[17] A. Fukuyama, A. Goto, S. -I. Itoh, and K. Itoh, Jpn. J. Appl. Phys. **23** (1984) L613.

[18] A. A. Galeev and R. N. Sudan(ed.), *Basic Plasma Physics* (North-Holland, Amsterdam, 1989).

Chapter 4

High Confinement Mode Resulting from Bifurcated Transition in Radial Transport

4.1 Introduction

Since the axial particle confinement in tandem mirrors was greatly improved by forming confining potential with thermal barrier [1, 2], the radial particle transport has become of primary importance as in tokamaks. The discovery of an improved confinement regime [3], which is called H mode, has initiated extensive investigations for enhanced radial confinement in many tokamak devices. In H-mode discharges, which are generally generated by high power auxiliary heating, the following features are observed : Transition through bifurcation leads to the drops of H_α/D_α emission, density and energy rise, and density profile is steepened on the edge. Particle or energy confinement time is enhanced by a factor of 1.5−3 in comparison with low confinement mode (L-mode) plasmas. Change to the enhanced confinement phase takes place within several hundred microseconds, which indicates the presence of bifurcated states of edge plasma parameters. The understandings of the conditions leading to H mode and the physical mechanism of reduction of particle and energy loss are inevitable in order to produce a controlled improved confinement. Some

theoretical and experimental studies have shown that the radial currents/electric fields could trigger H mode through sheared plasma rotation [4–7]. Although no observation of H-mode-like behavior has been reported in tandem mirror devices, similar situation could be realized through the generation of radial electric field E_r and/or its shear.

Earlier works in mirror devices have shown the possibilities of control of radial electric fields and reduction of fluctuations of certain instabilities. In the experiment of Q_T-Upgrade machine [8], segmented plates located at both ends were biased with various voltage levels and radial potential profile was successfully controlled, although there is no description of biasing effects on the anomalous transport. In HIEI single mirror device flute mode instability was suppressed using RF stabilization method [9]. Stability of rotationally driven flute or interchange modes was investigated in Phaedrus by controlling E_r [10]. It was found in this experiment that the rigid $\boldsymbol{E} \times \boldsymbol{B}$ rotation was a dominant influence on the observed instability rather than shear in E_r. The experiments of GAMMA 10 [11] revealed that ambipolar potential controlled by biased end rings affected drift wave instability. Gradual change in fluctuation level and radial transport with the bias voltage was observed in correlation with a change in global radial potential profile. These experimental results in mirrors could be explained by a "soft" transition in stability due to a gradual change in rigid rotation of plasma column. Recently, radial transport in a sheared electric field was studied in the PISCES-A linear plasma device [12], and reduction of fluctuation-induced transport was observed. In this experiment, however, no observation of transition or bifurcated phenomenon was reported.

This chapter deals with the improvement on radial confinement using limiter biasing, which is the first observation of H-mode-like behavior in tandem mirrors. With positive limiter biasing, increase of bulk density and energy, reduction of edge fluctuation level, and steepening of edge density profile are observed. Simultaneous drop of neutral emission

and bifurcation of limiter current indicate "hard" transition phenomena. The suppression of edge turbulence may be attributed to the observed rotational shear in the edge. When a bias voltage applied on the limiter is changed gradually up and down, edge plasma parameters vary with hysteresis characteristics. Such characteristics could be explained by bifurcated solutions of azimuthal momentum balance equation with a radial current imposed by limiter biasing and with a diffusion coefficient affected by rotational shear.

Section 4.2 describes experimental set-up with configuration of limiter biased by DC power supply. In Sec. 4.3 experimental results are demonstrated, including typical time evolution of a *H*-mode-like discharge, bias voltage dependence, and change of edge plasma parameters. In Subsec. 4.4.1 enhancement factor of radial confinement is estimated from the experimental results, and a simple transition model based on azimuthal momentum balance is employed to clarify physics of the observed bifurcation in Subsec. 4.4.2.

4.2 Experimental setup

HIEI [1] is the so-called "ICRF tandem mirror" experimental machine, that is, the tandem mirror operated only by mode-controlled ICRF (Ion Cyclotron Range of Frequencies). HIEI has a completely axisymmetric configuration, and the central cell is 1.9 m in length and 25 cm in radius with plug cells 0.7 m in length on both sides of the central cell. The central cell ICRF($\omega/2\pi$ = 8 MHz) generates a helicon/fast wave to produce and heat the plasma simultaneously via mode conversion [13]. Ponderomotive force produced by RF field stabilizes the plasma macroscopically against the flute instability [9]. All the measurements described below are performed in the HIEI central cell. End plates located outside both plug cells are floating. The limiters are located at four axial positions(z = $\pm$ 18 cm and $\pm$ 34 cm, where z denotes axial position with respect to the midplane of the central cell). Each limiter has a radius a = 14 cm (projected to z = 0 cm plane)

and is segmented into 4 parts azimuthally. One limiter located at $z = -34$ cm is utilized for biasing by applying DC voltage to 4 segments in parallel, and the other limiters are floating. The DC power supply is a capacitor bank of $2.8 \times 10^4 \mu$F and the voltage between $-300-+300$ V with respect to the grounded vessel wall is used for biasing on the limiter in the experiments. A grounded gas box is located in the midplane($z \sim 0$ cm), which is axially separated from the biased limiter by a floating one($z = -18$ cm). Radial edge of the grounded gas box is approximately 1 cm inside the biased limiter. When a bias voltage V_{bias} is applied on the limiter, a bias current I_{bias} flows radially to the gas box and axially to the grounded throat wall($z = -75$ cm). Probe measurements indicate formation of radial electric field E_r near the biased limiter edge and ion sheaths on the limiter and the throat wall surface in the case of limiter biasing, which verifies the presence of both radial and axial currents.

The magnetic field strength at the midplane of the central cell is set to 0.035 T with the mirror ratio 7. Plasma is produced using the central cell ICRF(the net input power $= 50-70$ kW) with He gas puffing. Hydrogen atoms with a few percents are involved from the wall as recycling particles. The plasma parameters of typical discharges are : peak plasma density $n_e \sim 7 \times 10^{12}$ cm^{-3} in the case of no biasing on the limiter, $T_e = 10-30$ eV, and $T_i = 30-40$ eV. Plasma line density is measured by far-infrared (FIR) laser interferometer, and local density and density fluctuations in the edge are monitored by Langmuir probes calibrated by the FIR interferometer. T_e and T_i shows no significant change by the limiter biasing.

4.3 Experimental results

Figure 4.1 shows the time evolution of, from top to bottom, limiter bias voltage V_{bias}, limiter current I_{bias}, line density nl, stored energy as measured by diamagnetic loop W_{dia},

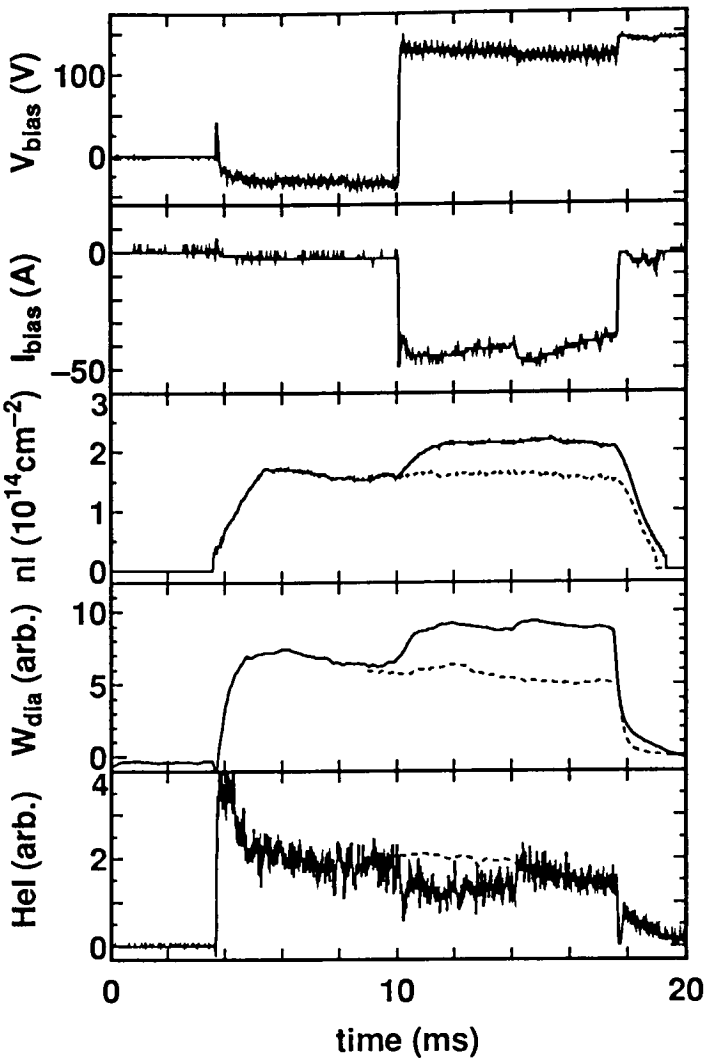

FIG. 4.1. Typical temporal evolutions of global plasma parameters of a positive bias shot(solid line) in comparison with a no-biasing shot (dotted line). From top to bottom : bias voltage on the limiter V_{bias}, limiter current I_{bias}, line density through the axis($z = 0$ cm) nl, stored energy(diamagnetism)($z = -60$ cm) W_{dia}, and HeI emission through the axis($z = -30$ cm).

and neutral line emission(HeI) with(solid line) and without(dotted line) the limiter biasing of ~130 V Before the limiter biasing for $t < 10$ msec, fluctuations with large amplitude are observed at 10 cm $< r <$ 13.5 cm ($0.71 < r/a < 0.96$), i.e., in the plasma periphery. The density and potential fluctuation levels $\tilde{n}/\langle n \rangle$ and $\widetilde{V_f}/\langle V_f \rangle$ at $r = 12$ cm are ~ 0.5 and ~ 0.2, respectively, where n is the local plasma density, V_f is the floating potential, tilde denotes the fluctuating part, and angular brackets denote a time average over a time-scale long compared to the frequency of the fluctuations. The value of $\tilde{n}/\langle n \rangle$ at $r = 12$ cm (~ 0.5) is larger by a factor of 5–10 than at $r = 0$ cm (< 0.1). The frequency of the fluctuations ranges from ~ 4 kHz to ~ 12 kHz with the azimuthal mode number 2–6. The fluctuations are inferred to be driven by drift mode instability as described in the following. The fluctuations are localized in the region of steep density gradient. Axial correlation measurement reveals that the instability has finite values of $k_{||}$. The propagating direction is inferred to be of the electron diamagnetic drift by a cross-correlation technique. After the onset of limiter biasing at $t = 10$ msec, edge fluctuations suddenly vanish within 0.2 msec. Simultaneously nl rises up to approximately 1.5 times of the initial value as well as W_{dia}, as shown in Fig. 4.1. The emission line intensity of HeI(5876Å) drops clearly for 4 msec from the onset of biasing. The dotted line of HeI in the case of no biasing indicates averaged value for clarity. It is found that H_α drops as well. Another significant change is found in I_{bias} in Fig. 4.1. At $t = 10$ msec, which corresponds to the starting point of HeI drop, I_{bias} decreases suddenly(we can recognize it as a small peak in I_{bias} at $t = 10$ msec). Then at $t = 14$ msec, which corresponds to the ending point of HeI drop, it jumps up to higher level again. From the estimation of time evolution of W_{dia}, radial energy loss flux decreases by a factor of ~2, and becomes approximately half of axial flux which is doubled by the biasing with unchanged axial confinement. Here the input power by the limiter biasing (<6kW) is considerably smaller than that by the ICRF injection

(~70 kW) which is almost constant through the discharge.

The voltage-current characteristic of the limiter is shown in Fig. 4.2. The floating potential of the limiter is around ~ -30 V I_{bias} shows a transition from ~ 60 A to ~ 49 A at $V_{bias} \sim 80$ V, which represents some bifurcation phenomenon. The transition point to lower current level varies with conditions such as amount of gas puffing or net power of the central cell ICRF, which are related to the content of neutral particles in the scrape-off layer(SOL). As shown in Fig. 4.1, density build-up and reduction of edge turbulence are observed in the lower current phase. Earlier studies of electrode biasing [5, 14, 15] showed the similar tendency, i.e., low currents in the H mode and high currents in the L mode.

Figure 4.3 shows the dependence of local density at $r = 0$ cm $n(0)$, W_{dia}, and $\tilde{n}/\langle n \rangle$ at $r = 12$ cm$(r/a = 0.86)$ $\tilde{n}/\langle n \rangle(12)$ on V_{bias}. As V_{bias} is raised above the floating potential level of the limiter $V_{fl}(V_{fl} \sim -35$ V in this case), $\tilde{n}/\langle n \rangle(12)$ decreases sharply, which is accompanied by the increase of $n(0)$ as well as W_{dia}. Since T_e is invariant on V_{bias}, the change of W_{dia} reflects that of the global density. nl through the axis rises with V_{bias} as well. $\widetilde{nl}/\langle nl \rangle$ at $r = 9$ cm and $\widetilde{V_f}/\langle V_f \rangle$ at $r = 12$ cm shows the similar variation to $\tilde{n}/\langle n \rangle(12)$ with V_{bias}. No significant change is found in all the signals when V_{bias} is varied below V_{fl}.

Figure 4.4 displays the radial profile of density in the edge. The increase of density is observed inside the limiter edge, and density in SOL ($r > 11.5$ cm in Fig. 4.4) shows abrupt reduction by a factor of 3–5 on the onset of biasing. E-folding length of radial density gradient in the periphery near the biased limiter changes from ~ 1.5 cm in the case of no biasing to ≤ 0.4 cm in the case of biasing. Such significant modifications of the density profile have not been reported in the DC biasing experiments in other linear devices [10–12].

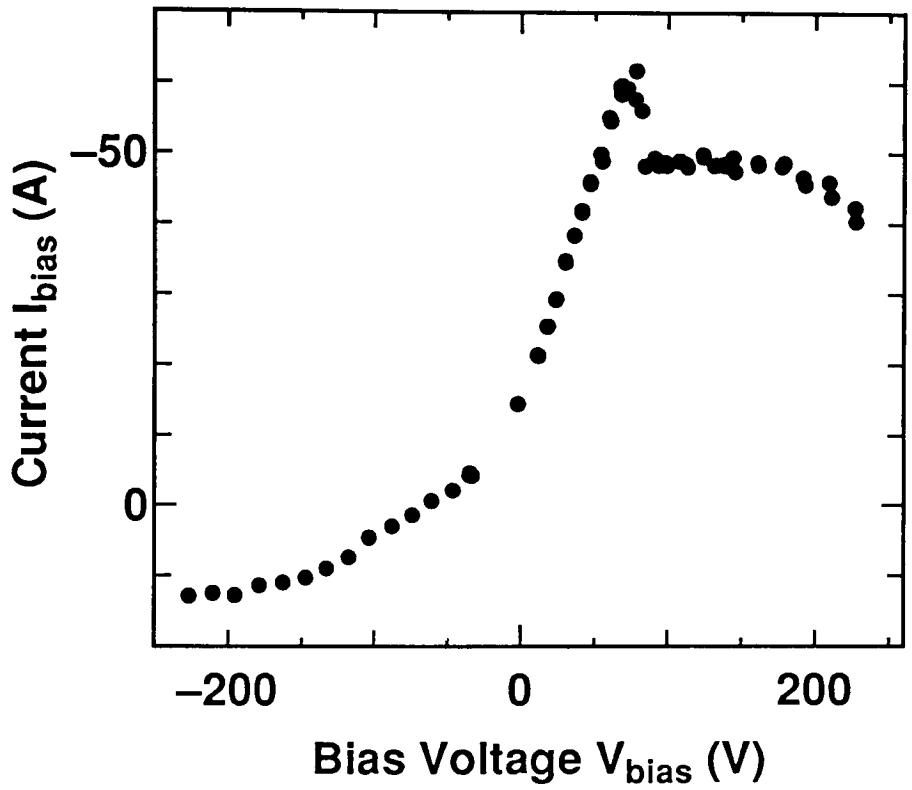

FIG. 4.2. Voltage-current characteristic of the limiter.

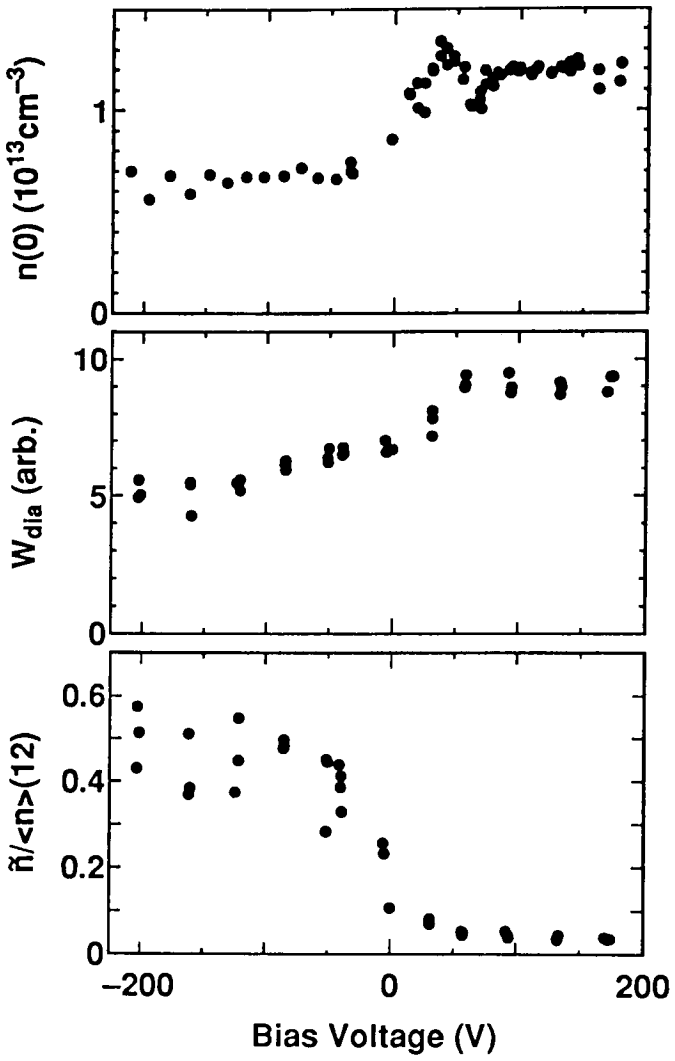

FIG. 4.3. Density at $r = 0$ cm($z = 0$ cm) $n(0)$, stored energy($z = -60$ cm) W_{dia}, and fluctuation level at $r = 12$ cm($z = 0$ cm) $\tilde{n}/ < n > (12)$ as a function of bias voltage V_{bias}.

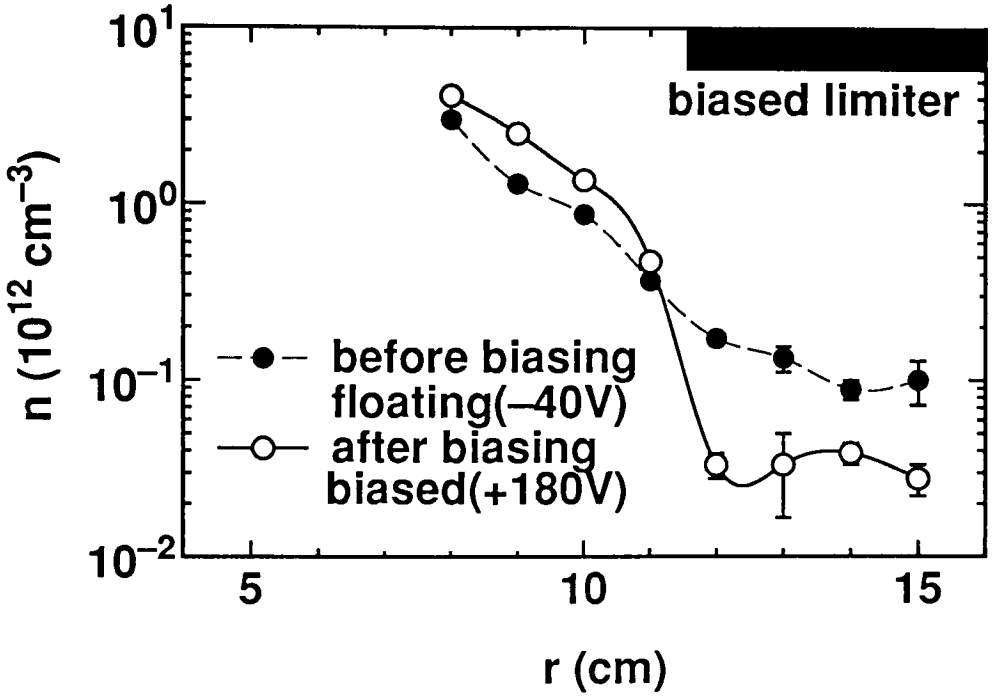

FIG. 4.4 Radial profiles of density in the edge in the cases of limiter biasing and no biasing measured at $z = -60$ cm. Bias voltage is applied from $t = 11.0$ msec in this case.

Azimuthal rotation velocity is measured by a modified Gundestrup probe, which has a smaller size than the original one [16] to be inserted into a main plasma. An insulator cap is attached to prevent radial ion flux from entering a tip. Figure 4.5 shows radial profiles of ion azimuthal rotation velocity v_θ, expressed as Mach number M_θ, in the cases of limiter biasing and no biasing. As compared with a monotonous profile in the case of no biasing, significant rotation is induced in the edge region by limiter biasing, while rotation velocity remains constant in the bulk region. Rotation velocity with $M_\theta = 0.6$ is $\sim 2 \times 10^4$ m/s, which corresponds to $E_r \times B$ rotation velocity with $E_r \sim 10$ V/cm. This value agrees with E_r measured by a Langmuir probe within one order. Furthermore, a large rotational shear is observed in the edge region. The observation of strong rotational shear distinguishes our experiments from those in other mirror devices [11, 12]. Similar features, that is, larger E_r and larger rotational shear in the periphery, have been observed in tokamak H-mode discharges [5, 6]. The reduction of fluctuations in the edge (see Fig. 4.3) is attributed to the occurrence of rotational shear, which is theoretically pointed out by Biglari *et al.* [7]

As shown in Fig. 4.1, transition from low to high confinement phase takes place rapidly in the case of step-wise biasing. Transition phenomena are investigated in Fig. 4.6 as V_{bias} is gradually increased or decreased during one discharge. When V_{bias} is gradually raised (open circles), the edge plasma parameters change monotonously, and they show simultaneous changes in a step-wise way at the threshold bias voltage ($V_{bias} \sim 103$ V); I_{bias} and HeI drop, floating potential V_f on the edge increases, and $\tilde{n}/\langle n \rangle$ decreases. On the other hand, when V_{bias} is decreased (closed circles), they change at the different threshold bias voltage($V_{bias} \sim 84$ V). The threshold values are almost constant when the rate of changing V_{bias} varies from 10 V/msec to 50 V/msec, and the possibility that hysteresis comes from time delay due to instability growth rate can be ruled out. Hysteresis phenomena are also

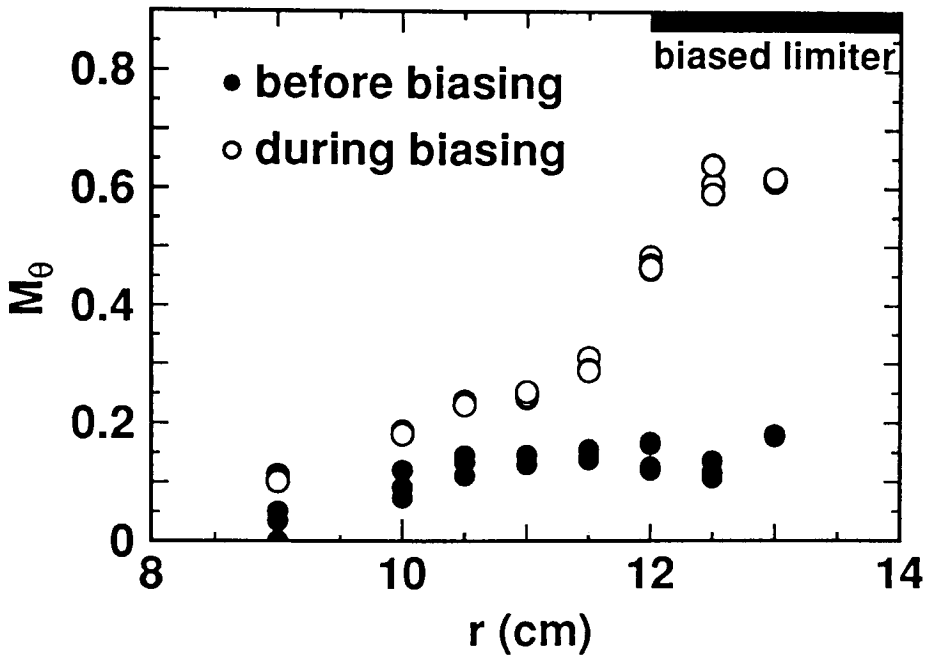

FIG. 4.5. Radial profiles of M_θ at $z = -60$ cm before(closed circles) and during(open circles) limiter biasing in the case of $V_{bias} \sim 150$ V and $I_{bias} \sim 40$ A with the projected area of the biased limiter.

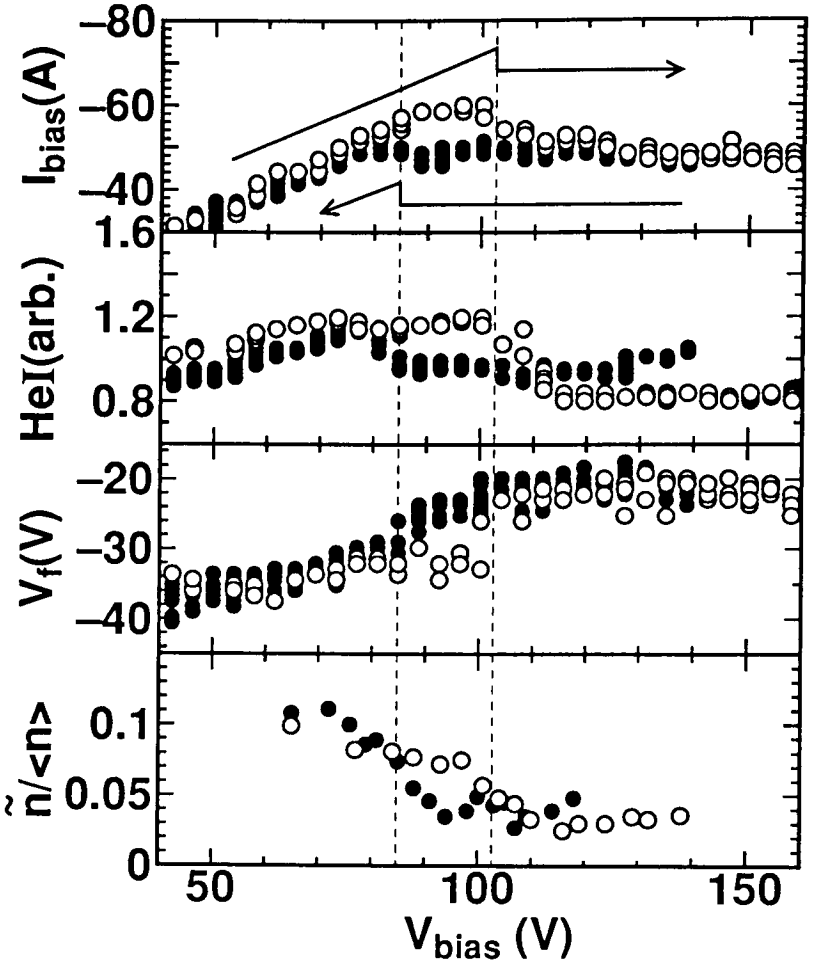

FIG. 4.6. Variation of edge plasma parameters (I_{bias}, HeI at $z = -60$ cm, V_f at $r/a \sim 1$ and $z = -60$ cm, and $\tilde{n}/\langle n \rangle$ at $r/a \sim 0.95$ and $z = 0$ cm) as V_{bias} is gradually increased (open circles) or decreased (closed circles) during one discharge. Vertical dashed lines indicate the threshold voltages.

found in the same signals as in Fig. 4.6 when plasma parameters are plotted as a function of I_{bias}. I_{bias} can take one value for different values of edge parameters such as V_{bias}, V_f, $\tilde{n}/\langle n \rangle$. Such bifurcation is also observed in the rotational velocity, that is, for one value of limiter current ($I_{bias} \sim 40$ A), M_θ is ~ 0.48 at $r/a \sim 1.0$ for $V_{bias} \sim 150$ V and M_θ is ~ 0.35 for $V_{bias} \sim 50$ V.

4.4 Discussion

4.4.1 Enhancement factor of radial confinement

Radial particle flux induced by edge turbulence [17], Γ, can be estimated by the correlation between the density fluctuations $\tilde{n}$ and the plasma potential fluctuations $\tilde{\phi}$ over the observed frequency range. The experimental parameters used for the estimations are in the following : $\tilde{n} = 6.0 \times 10^{11}$ cm^{-3}, $\tilde{\phi} \sim \widetilde{V_f} = 6$ V, $m = 2$–6 at $r = 0.13$ m($r/a \sim 0.93$) for the case of no biasing, and $\tilde{n} = 9.0 \times 10^{10}$ cm^{-3}, $\tilde{\phi} \sim \widetilde{V_f} = 1$ V, $m = 2$, for the case of biasing. Thus we obtain $\Gamma = 2.2 \times 10^{20}$ m^{-2} sec^{-1} for the case of no biasing and $\Gamma = 2.8 \times 10^{19}$ m^{-2} sec^{-1} for the case of biasing. The calculated Γ for the case of no biasing is smaller by one order than Γ predicted by the Bohm's diffusion and Γ for the case of biasing is larger by a factor of 2 than Γ predicted by the classical diffusion theory. Fluctuation-induced transport decreases with the limiter biasing by one order. Figure 4.3 shows such tendency clearly, that is, the density rise due to the reduction of outward fluctuation-induced transport is observed when positive bias voltage is applied to the limiter and the fluctuation is sufficiently suppressed. Γ is connected to the corresponding radial particle confinement time $\tau_{\perp t}$ by the relation $\Gamma \ 2\pi r = \langle n \rangle \pi r^2 / \tau_{\perp t}$. $\tau_{\perp t}$ in the case of no biasing($\tau_{\perp t}$) and biasing ($\tau'_{\perp t}$) are estimated using the calculated values of Γ, which yields $\tau_{\perp t} = 0.29$ msec and $\tau'_{\perp t} = 2.8$ msec.

nl and W_{dia} rise by the limiter biasing as shown in Fig. 4.3, and such changes represent the enhancement of particle and energy confinement in the bulk region. The enhancement of radial particle confinement is estimated as follows. The particle balance equation can be written as

$$\frac{dN}{dt} = S - \frac{N}{\tau_\perp} - \frac{N}{\tau_{||}}, \tag{4.1}$$

where N is the global density, S is the fueling rate, and τ is the particle confinement time across/along the magnetic fields. N is estimated from nl, and S is considered to be proportional to the intensity of HeI. We can obtain three equations for (a) the phase before biasing, (b) the density build-up phase just after the onset of biasing, and (c) the steady phase after the build-up phase (see Fig. 4.1). $\tau_{||}$ shows no significant variation with V_{bias} by the measurement of end loss flux. We take $({\tau_\perp}^{-1} + {\tau_{||}}^{-1})^{-1}$ before biasing $\sim$ 0.91 msec as the decay time of density after switching off the central cell ICRF injection. The value of $({\tau_\perp}^{-1} + {\tau_{||}}^{-1})^{-1}$ during HeI drop is calculated as 2.3 msec from Eq. 4.1. The density exponentiation time in the phase (b) in Fig. 4.1 is $\sim$ 1.5 msec, which also yields $({\tau_\perp}^{-1} + {\tau_{||}}^{-1})^{-1} \sim 2.3$ msec. We note that this enhancement of particle confinement time ($\sim$ 2.5) is attributed to the improved radial confinement.

The improvement on radial confinement is also verified by the drop of HeI and the shortened radial density decay length by a factor of 4. That is attributed to the reduction of fluctuation-induced transport, and the edge turbulence suppression is inferred to result from rotational shear. The observed rotational shear appears to be formed through bifurcation in rotation velocity that is related to the observed bifurcation in I_{bias}.

4.4.2 Model of bifurcated transport

In order to interpret the observation of the bifurcated feature with the induced edge rotation, we conventionally introduce an available model from tokamak H-mode analysis

[18], using a momentum balance equation

$$\rho\frac{d\boldsymbol{v}}{dt} = \boldsymbol{j}\times\boldsymbol{B} - \nabla\ \boldsymbol{\Pi} - \nabla P - \boldsymbol{R}. \tag{4.2}$$

Here $\rho(= mn)$ is the mass density, $\boldsymbol{v}$ the fluid velocity, $\boldsymbol{j}$ the current density, $\boldsymbol{B}$ the static magnetic field, and P the plasma pressure. The second term of the right hand side indicates the plasma viscosity, and $\boldsymbol{R}$ represents collision terms. For ion momentum in the azimuthal direction in a steady state, Eq. 4.2 becomes

$$-\frac{1}{r}\frac{d}{dr}(rmD\frac{dv_\theta}{dr}) - nm\nu_{i0}v_\theta = j_r B_z, \tag{4.3}$$

where

$$\Gamma = -D\frac{1}{n}\frac{dn}{dr},\ D = D_H + \frac{D_L}{1+\alpha_\Gamma\mid\frac{dv_\theta}{dr}\mid^\gamma}, \tag{4.4}$$

and ion-neutral collision frequency $\nu_{i0} = n_0\langle\sigma_{CX}v_i\rangle$ with the neutral density of n_0. Γ is the radial particle flux, and the diffusion coefficient D has the dimension of conductivity. D is assumed to be reduced by the gradient of the azimuthal rotation velocity dv_θ/dr, where D_H and D_L are the constants and α_Γ and γ determine threshold and sharpness of the nonlinear process [18]. This form of D was based on the work by Biglari *et al.* [7] and was proposed to account for the *H*- and *VH*-mode (very high confinement mode) in DIII-D [18]. Eq. 4.3 indicates that (I) radial current density j_r is a driving force of the azimuthal rotation, (II) viscosity and ion-neutral collision are decelerating forces, and (III) increase of dv_θ/dr reduces D by Eq. 4.4 [7], which leads to nonlinear effects on the first term of the left hand side. Several rotation velocity profiles are assumed and Eq. 4.3 is solved as a function of j_r, shown in Fig. 4.7. In the case of rigid rotation (a), no bifurcation is present. On the other hand, parabolic rotation (b) and localized rotation in the periphery (c) result in the bifurcated states of dv_θ/dr and D for j_r. Strong rotational shear is expected to produce transition from low to high confinement mode. In

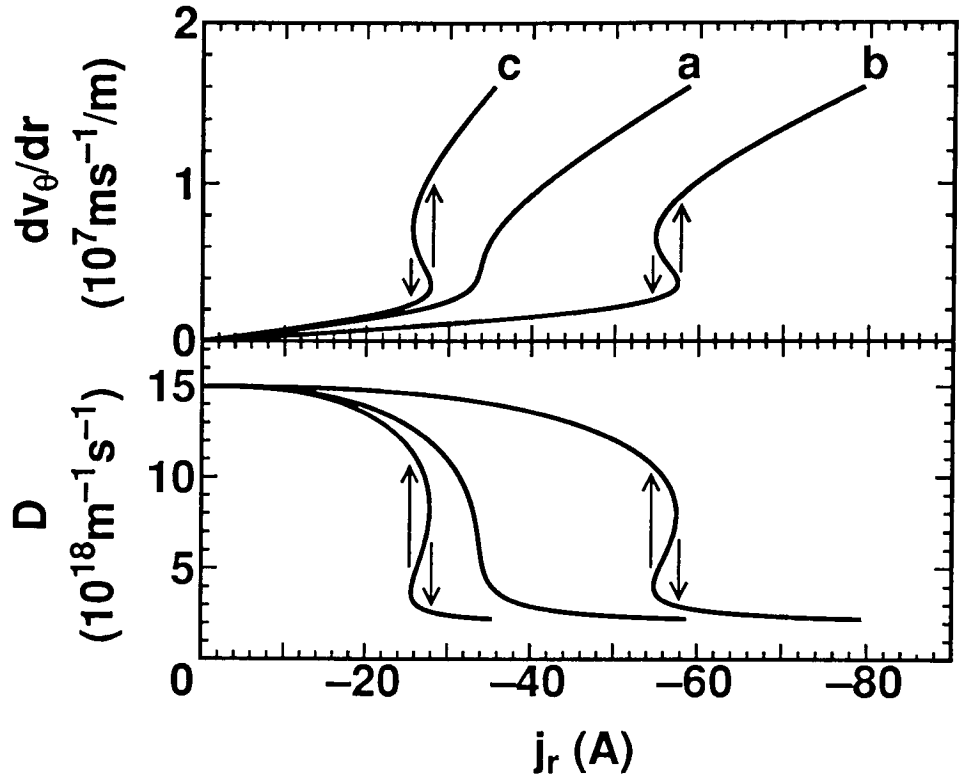

FIG. 4.7. Numerical results of transition model by Eq. 4.3 (dv_θ/dr and D as a function of j_r). Curve "a" denotes the case with $v_\theta = kr$, curve "b" with $v_\theta = kr^2$, and curve "c" with $v_\theta = k(r - r_0)$ for $r > r_0$ and $v_\theta = 0$ for $r \leq r_0$ with $r_0 = 11$ cm , where k is constant in one profile. Other parameters are as follows; He plasma with density $n_e = 10^{18}$ m^{-3} and $T_i = 30$ eV, $B = 0.06$ T, $r = 12$ cm, $\Gamma = 5 \times 10^{20}$ m^{-2}s^{-1}, $\alpha_\Gamma = 10^{-17}$, $\gamma = 2.6$, $D_L = 1.3 \times 10^{19}$ m^{-1}s^{-1}, $D_H = 2.0 \times 10^{18}$ m^{-1}s^{-1}, and $n_0 = 10^{17}$ m^{-3}

the experiment the induced rotation velocity profile is similar to (b) or (c) since rotational shear is clearly observed in Fig. 4.5.

This model is one of the good candidates for explanation of our experimental observation. The rapid change of plasma parameters, as shown in Fig. 4.1, is due to the transition to the high confinement mode with strong rotational shear and with a reduced diffusion coefficient. The bifurcated states of edge fluctuation level and rotational velocity for I_{bias} are well expressed in this model. Figure 4.8 shows the edge fluctuation level and D as a function of I_{bias} derived from Fig. 4.6 and Eq. 4.3, where in the model analysis formation of ion sheaths is assumed in the axial direction and the force balance equation is combined with Eq. 4.3 to derive the sheath potential. When fluctuation-induced diffusion is dominant on the edge, D is determined by the edge fluctuation level. Bifurcated states of $\tilde{n}/\langle n \rangle$ are qualitatively in agreement with the calculated plot of D. Application of more explicit expressions for D and viscosity term relevant to mirror configuration remains for the future work. However, basic phenomena in the experimental observation are all involved in the results of calculation: j_r is the driving force for sheared rotation, shear in plasma rotation reduces edge turbulence, and bifurcation in radial transport results in transition to the high radial confinement mode.

4.5 Conclusion

In conclusion, we have demonstrated the transition leading to the improved radial confinement induced by DC limiter biasing in the HIEI tandem mirror. As the bias voltage on the limiter is raised in the range of positive values, the fluctuation level of both density and potential in the edge region decreases and the bulk density increases up to 1.2×10^{13} cm^{-3} by a factor of 1.5–2. The particle confinement time is estimated to increase by a factor of 2.5. During this high radial confinement mode, HeI and H_α

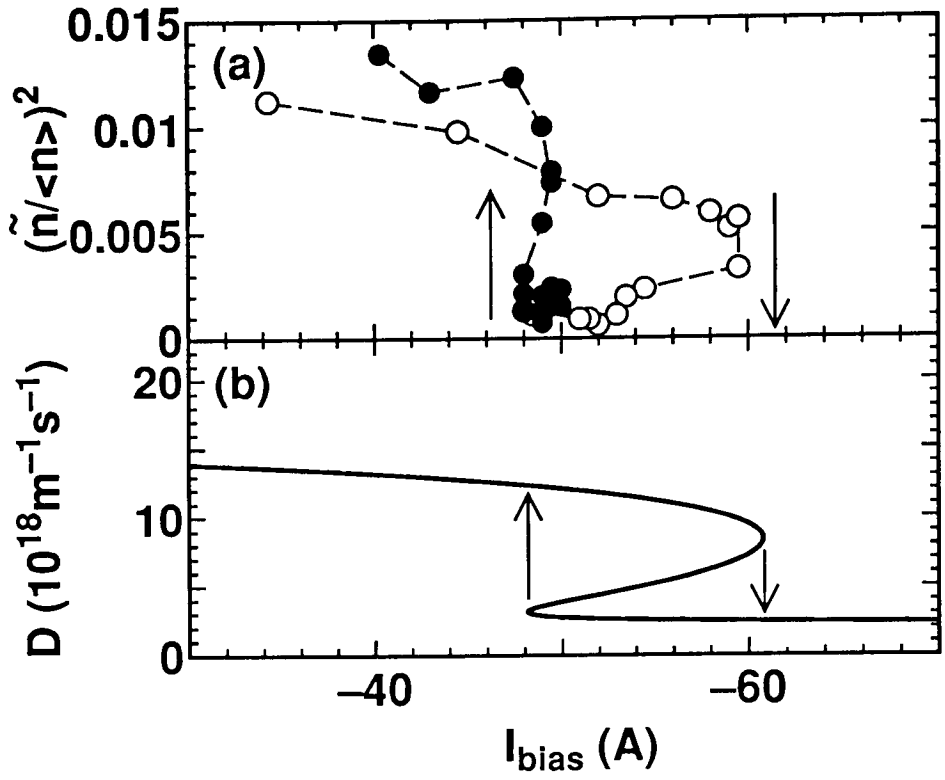

FIG. 4.8. (a) Edge density fluctuation power spectra from Fig. 3, and (b) theoretical plot of D obtained in the case of "c" in Fig. 4 with $D_L = 12.8 \times 10^{18}$ $m^{-1}s^{-1}$, $D_H = 2.2 \times 10^{18}$ $m^{-1}s^{-1}$ and $\alpha_\Gamma = 1.5 \times 10^{-18}$ as a function of I_{bias}. Formation of ion sheaths on the grounded throat wall and on the biased limiter is assumed in the axial direction, and the force balance equation is combined with Eq. 4.3 to derive sheath potential. $n_e = 10^{18}$ m^{-3} at $r = 11$ cm, and n_e at $r = 12$, which is assumed to be the radial position of the biased limiter edge, is derived from Eq. 4.4.

drop, limiter current decreases, and plasma rotation changes significantly. Radial electric field is inferred to be larger from the rotation measurement, and its shear might suppress the edge turbulence. As bias voltage is increased or decreased in one shot, edge plasma parameters change along bifurcated paths. The observed strong nonlinear phenomena, the change of the limiter currents, and the sudden drop of HeI demonstrate bifurcation feature, which is similar to that in L-H transition in tokamaks. Such transition features are basically explained by the model from the azimuthal momentum balance and the shear stabilization.

References

[1] Y Yasaka, M. Miyakita, S. Kimoto, H. Takeno, and R. Itatani, in *Plasma Physics and Controlled Nuclear Fusion Research*, (IAEA, Vienna, 1991), Vol. 2, p. 725.

[2] M. Inutake, T. Cho, M. Ichimura, K. Ishii, A. Itakura, I. Katanuma, Y. Kiwamoto, Y. Kusama, A. Mase, S. Miyoshi, Y Nakashima, T. Saito, A. Sakasai, K. Sawada, I. Wakaida, N. Yamaguchi, and K. Yatsu, Phys. Rev. Lett. **55** (1985) 939.

[3] F. Wagner, G. Becker, K. Behringer, D. Cambell, A. Eberhagen, W Engelhardt, G. Fussmann, O. Gehre, J. Gernhault, G. v. Gierke, G. Haas, M. Haung, F. Karger, M. Keilhacker, O. Kluber, M. Kornherr, K. Lackner, G. Lisitano, G. G. Lister, H. M. Mayer, D. Meisel, E. R. Muller, H. Murmann, H. Niedermeyer, W Poschenrieder, H. Rapp, H. Rohr, F Schneider, G. Siller, F Speth, A. Stabler, K. H. Steuer, G. Venus, O. Vollmer, and Z. Yu, Phys. Rev. Lett. **49** (1982) 1408.

[4] K. C. Shaing and E. C. Crume, Jr., Phys. Rev. Lett. **63** (1989) 2369.

[5] R. J. Taylor, M. L. Brown, B. D. Fried, H. Grote, J. R. Liberati, G. J. Morales, and P Pribyl, Phys. Rev. Lett. **63** (1989) 2365, R. R. Weynants and R. J. Taylor Nucl. Fusion **30** (1990) 945.

[6] R. J. Groebner, K. H. Burrell, and R. P. Seraydarian, Phys. Rev. Lett. **64** (1990) 3015, H. Matsumoto *et al.*, Plasma Phys. Contr. Fusion **34** (1992) 615.

[7] H. Biglari, P H. Diamond, and P W. Terry, Phys. Fluids B **2** (1990) 1.

[8] A. Tsushima, T. Mieno, M. Oertl, R. Hatakeyama, and N. Sato, Phys. Rev. Lett. **56** (1986) 1815.

[9] Y. Yasaka and R. Itatani, Phys. Rev. Lett. **56** (1986) 2811.

[10] G. D. Severn, N. Hershkowitz, R. A. Breun, and J. R. Ferron, Phys. Fluids B **3** (1991) 114.

[11] A. Mase, J. H. Jeong, A. Itakura, K. Ishii, M. Inutake, and S. Miyoshi, Phys. Rev. Lett. **64** (1990) 2281, A. Mase, A. Itakura, M. Inutake, K. Ishii, J. H. Jeong, K. Hattori, and S. Miyoshi, Nucl. Fusion **31** (1991) 1725.

[12] R. J. Taylor, R. W Conn, B. D. Fried, R. D. Lehmer, J. R. Liberati, P A. Pribyl, L. Schmitz, G. R. Tynan, B. C. Wells, D. S. Darrow, and M. Ono, in *Plasma Physics and Controlled Nuclear Fusion Research* (IAEA, Vienna, 1991), Vol. 1, p. 463.

[13] Y. Yasaka, H. Takeno, A. Fukuyama, T. Toyoda, M. Miyakita, and R. Itatani, Phys.Fluids B **4** (1992) 1486.

[14] L. G. Askinazi V E. Golant, S. V Lebedev, V A. Rozhanskij, M. Tendler, Nucl. Fusion **32** (1992) 271.

[15] R. R. Weynants, G. V Oost, G. Bertschinger, J. Boedo, P Brys, T. Delvigne, K. H. Dippel, F. Durodie, H. Euringer, K. H. Finken, D. S. Gray, J. D. Hey, D. L. Hillis, J. T. Hogan, L. Konen, R. Leners, A. M. Messiaen, A. Pospieszczyck, U. Samm, R. P Schorn, B. Schweer, G. Telesca, R. V. Nieuwenhove, and P E. Vandenplas, Nucl. Fusion **32** (1992) 837.

[16] C. S. MacLatchy, C. Boucher, D. A. Poirier, and J. Gunn, Rev. Sci. Instrum. **63** (1992) 3923.

[17] P C. Liewer, Nucl. Fusion **25** (1985) 543.

[18] F. L. Hinton, Phys. Fluids B **3** (1991) 696, G. M. Staebler, F L. Hinton, J. C. Wiley, R. R. Dominguez, C. M. Greenfield, P Gohil, T. K. Kurki-Suonio, and T. H. Osborne, Phys. Plasmas **1** (1994) 909.

Chapter 5

High-Beta Operation with Enhanced Axial and Radial Confinement

5.1 Introduction

In a mirror device it is well known that reduction of axial particle loss along the magnetic field lines is one of the key issues for improvement of confinement. Simultaneously, once axial confinement is enhanced, radial anomalous transport, which is commonly observed in magnetic confinement devices, becomes a dominant particle and energy loss. It is of importance that both axial and radial confinement are enhanced simultaneously to improve global confinement property.

Several methods [1–4] have been successfully used to form ion-confining potential in plug cells of tandem mirrors, and axial confinement time $\tau_{||}$ has been increased. In GAMMA 10, ECRH (Electron Cyclotron Resonance Heating) formed the ion-confining potential for the plasma with the central cell density $n_{ec} = 4.3 \times 10^{11}$ cm^{-3} and the central cell ion temperature $T_{ic} \leq 5$ keV, or for the plasma with $n_{ec} = 1.4 \times 10^{12}$ cm^{-3} and $T_{ic} \leq 5$ keV In Phaedrus, *near fields* of ICRF (Ion Cyclotron Range of Frequencies) waves in the plug cell enhanced the axial confinement for the plasma with $n_{ec} = 8.5 \times 10^{12}$ cm^{-3} and $T_{ic} \sim 55$ eV [2]. In the HIEI tandem mirror, formation of ion confining potential by ICRF

propagating waves has been investigated, and it is based on the mode conversion from the fast magnetosonic mode into an electrostatic mode at the ion-ion hybrid resonance layer [4]. The measurement of wave propagation showed that, in the case of the high-field-side injection of the fast wave, parallel wavenumber becomes large ($k_{||} = 10 - 100$ m^{-1}) at the ion-ion hybrid resonance layer enough to be resonant with bulk electrons. Simultaneously, the amplitude of electromagnetic fields turned into a small value, and it is considered to be due to mode conversion from the fast wave mode into an electrostatic mode. However, effects of the ion-ion hybrid resonance on potential formation has not been fully understood.

Radial transport will be a main loss channel in the case where axial confinement is significantly enhanced, as mentioned above. Before the prediction that high confinement mode (H mode) in tokamaks is attributed to formation of radial electric field [6, 7], radial confinement has been investigated in mirror devices in relation to radial electric field [8, 9]. In GAMMA 10 radial potential profile was controlled by end plate biasing, and change of edge fluctuation driven by the drift wave was observed in a quasi-state rigid rotation state. High radial confinement mode like H-mode discharges in tokamaks was observed using DC limiter biasing in HIEI with enhancement on the particle confinement of 2.5 [10]. Strong rotational shear was formed through transition from low to high confinement phase, and it suggested creation of the radial electric field in the edge. That is, ICRF waves and limiter biasing can change axial and radial potential profiles, which are strongly related to mirror confinement properties. Simultaneous application of axial ion-confining potential and sheared radial electric field may result in enhancement of global confinement.

To sustain such a high-beta plasma, stability against the flute interchange mode may be a critical problem. Beta limit against the flute interchange mode has been studied in several mirrors with quadrupole anchor cells. In GAMMA 10, stability limit was

experimentally clarified by the critical ratio of beta value in the central cell to that in the anchor cells [5].

However the presence of the minimum-B configuration causes additional radial loss. On the other hand, radio frequency (RF) stabilization for the flute mode has been performed in a completely axisymmetric configuration in HIEI [11] and Phaedrus in different frequency regimes [12]. Device configuration is axisymmetric with the stabilized plasma by ponderomotive force of RF fields so that no additional radial loss takes place. If the RF stabilization is found to be effective for a high-density ($> 10^{13}$ cm^{-3}) and high-beta (> 10 %) plasma, that will lead to its application in a future mirror reactor.

This chapter deals with enhancement of axial confinement by ICRF waves which is incident from the high-field side and the effects of the ion-ion hybrid resonance on formation of ion confining potential are clarified experimentally. Simultaneous enhancement on axial and radial confinement by controlled potential profiles is observed. The maximum core beta value obtained in the experiment reaches $\beta = 14\%$. The experimental results are compared with theoretical analysis of beta limit with the effects of RF stabilization above the ion cyclotron frequency against the flute interchange mode.

In Sec. 5.2, the experimental setup is described. The experimental results on axial confinement is shown in Subsec. 5.3.1, and here importance of the ion-ion hybrid resonance is clarified to create ion-confining potential. High-beta operation is presented with estimations of the enhancement factor of axial and radial confinement in Subsec. 5.3.2. The roles of ICRF waves on axial potential formation, interaction between enhanced axial and radial confinement, and beta limit in the presence of RF ponderomotive force are discussed in Sec. 5.4. Conclusions follow in Sec. 5.5.

5.2 Experimental setup

HIEI is the so-called "ICRF tandem mirror" experimental machine, that is, the tandem mirror operated by ICRF waves. The HIEI tandem mirror has a completely axisymmetric configuration, and the central cell is 1.9 m in length and 25 cm in radius with plug cells 0.7 m in length on both sides of the central cell. The production ICRF ($\omega/2\pi$ = 8 MHz, net input power = 70−90 kW, injected from dual half-turn antenna at z = −24 cm) generates the helicon/fast wave to produce a two-ion-species (He-H) plasma, where majority ions are He^+ and minority ones are H^+ The minority concentration is expressed by the puffed minority ratio (ν_{puff}) which is determined by the partial pressure of H stored in a gas tank before puffing. This value of concentration is used for determination of the position of the ion-ion hybrid resonance layer in the plug cell. To make sure that this ratio represents approximate concentration of each ions, the intensities of atomic emission lines (HeI:587.6 nm, H_α:656.2 nm) are monitored as ionization rates. Measurement in advance on these intensities as a function of density of a one-ion-species plasma enables to determine a ratio of each ion using relative intensities of two emission lines. In a range of this experimental parameter, ion ratio of H^+ in a two-ion-species plasma is estimated to be within a factor of 1.2 of gas puffing ratios for $\nu_{puff} \geq 4$ %, whereas minority ions are always involved with the ratio 2−3 % for $\nu_{puff} \leq 3$ % due to the recycling hydrogen particles from the wall. The production ICRF simultaneously stabilizes the produced plasma magnetohydrodynamically. Calculations of the propagating helicon/fast waves by the 2-dimensional ICRF code [13] show that the radial gradient of RF electric fields produce the ponderomotive force which stabilize the flute interchange mode. More detailed discussion will be held in Sec. 5.4.

The plug ICRF ($\omega/2\pi$ = 1.5 MHz, net input power < 100 kW) is injected from the dual half-turn antenna at z = +24 cm in the *central cell*. The resonance layers with the axial profile of the strength of the static magnetic field B are shown in Fig. 5.1. In

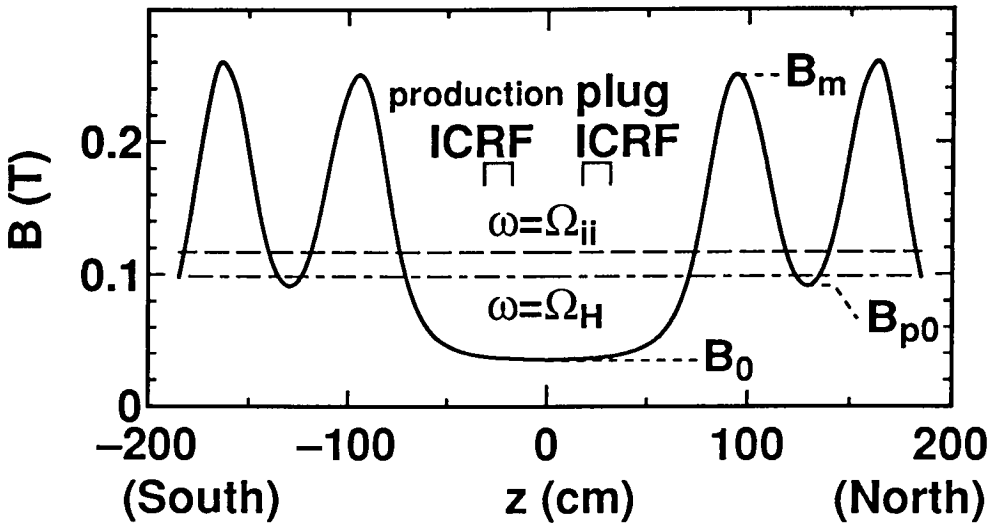

FIG. 5.1. Axial configuration of the static magnetic field B with the resonance layers of the plug ICRF waves (1.5 MHz). The central cell region is $-95 < z < 95$ cm, and the plug cell region is 95 cm $< z <$ 165 cm and -165 cm $< z < -95$ cm. B_0 is the strength of the static magnetic field in the central cell midplane, B_m is that at the mirror point, and B_{p0} is that of in the plug cell midplane. The ion-ion hybrid resonance layer ($\omega = \Omega_{ii}$) is shown for the case of the minority ion concentration = 10 %.

the central cell region the launched ICRF wave (the fast magnetosonic mode) encounters the pair of resonance layers (the minority cyclotron resonance ($\omega = \Omega_H$) and the ion-ion hybrid resonance ($\omega = \Omega_{ii}$)) from the *low-field side*, and contributes to ion heating via mode conversion into the slow ion-cyclotron wave [14, 15]. In the plug cell region the transmitting wave approaches to the ion-ion hybrid resonance from the *high-field side*, and converts into an electrostatic wave at the ion-ion hybrid resonance layer [4]. In the experiment of ref. 4, the ion-ion hybrid resonance layers are located near the mirror point between the central and the plug cells. Using the plug ICRF with $\omega/2\pi = 1.5$ MHz, the position of the ion-ion hybrid resonance layer is arranged near the midplane of the plug cell in order to create the ion-confining potential in a more efficient axial position.

The plasma radius a is limited to 14 cm by limiters in the central cell. The biased limiter is located at z = −34 cm, and the applied voltage ranges from +100 V to +200 V with respect to the grounded vessel wall. This range is considered to be appropriate to enhance the radial confinement [10]. End plates located outside both plug cells are kept floating.

5.3 Experimental results

5.3.1 Formation of ion confining potential in the presence of the ion-ion hybrid resonance layer

Formation of ion confining potential in the plug cell and its effect on axial confinement is examined using the plug ICRF The strength of the static magnetic field at the mirror point B_m is 0.25 T, that in the midplane of the plug cell B_{p0} is 0.097 T, and the mirror ratio in the central cell R_m is 7.1 in the standard operation. The parameters of the central cell plasma in typical discharges are : plasma density $n_{ec} \sim 2\text{–}3 \times 10^{12}$ cm^{-3} in the case

without injection of the plug ICRF, electron temperature $T_e = 7-15$ eV, majority (He^+) ion temperature $T_{He\perp} \sim 30$ eV, and minority (H^+) ion temperature $T_{H\perp} \sim 70$ eV in the case of the plug ICRF injection. n_{ec} is monitored by far-infrared laser interferometer, and T_{ic} for each ion is measured by Time-of-Flight neutral particle energy analyzer (TOF) located at $z = -60$ cm.

Figure 5.2(a) displays the time evolutions of electron temperature in the plug cell T_{ep}, and the maximum potential on axis $V_{s\,max}$. T_{ep} is measured from the ratio of two atomic emission lines of HeI (504.8 nm and 471.3 nm) [16]. $V_{s\,max}$ is defined as the maximum plasma potential along the static magnetic field lines, and is determined from the ion end loss flux monitored by end loss analyzer (ELA) with repeller grids. When the plug ICRF is injected, T_{ep} increases by a factor of 2, and $V_{s\,max}$ rises up to ~ 70 V T_{ic} is 30–70 eV and this potential hill is efficient for plugging the ions in the central cell. Plasma density in the central cell increases by the plug ICRF injection; n_{ec} in the case without injection is 3.5×10^{12} cm^{-3} and n_{ec} in the case with injection is 5.0×10^{12} cm^{-3}. Diamagnetic flux W_{dia} is detected by a diamagnetic loop located at $z = -60$ cm, and is found to increase as well as n_{ec}. Figure 5.2(b) shows the time evolution of the energy spectra of end loss ion flux at $r = 0$ Γ_{end}. The energy spectra $\Gamma_{end}(E)$ before the plug ICRF injection is approximately Maxwellian, and parallel ion temperature $T_{i\|}$ is estimated to be 20–30 eV During the plug ICRF injection, a significant reduction of Γ_{end} by a factor of 4–8 is found. In the low energy region (≤ 50 eV) $\Gamma_{end}(E)$ decreases greatly, or is not detected under resolution. The energy spectra are peaking at 50–70 eV, and such a value is evaluated as $V_{s\,max}$, which is shown in Fig. 5.2(a). In the high energy region (≥ 70 eV) $\Gamma_{end}(E)$ increases by the plug ICRF injection and it shows $T_{i\|} \sim 40-50$ eV This is partly because of the ion heating in the central cell by the plug ICRF. Axial profiles of plasma potential V_s is measured by an axially movable Langmuir probe. In the case with injection of the plug

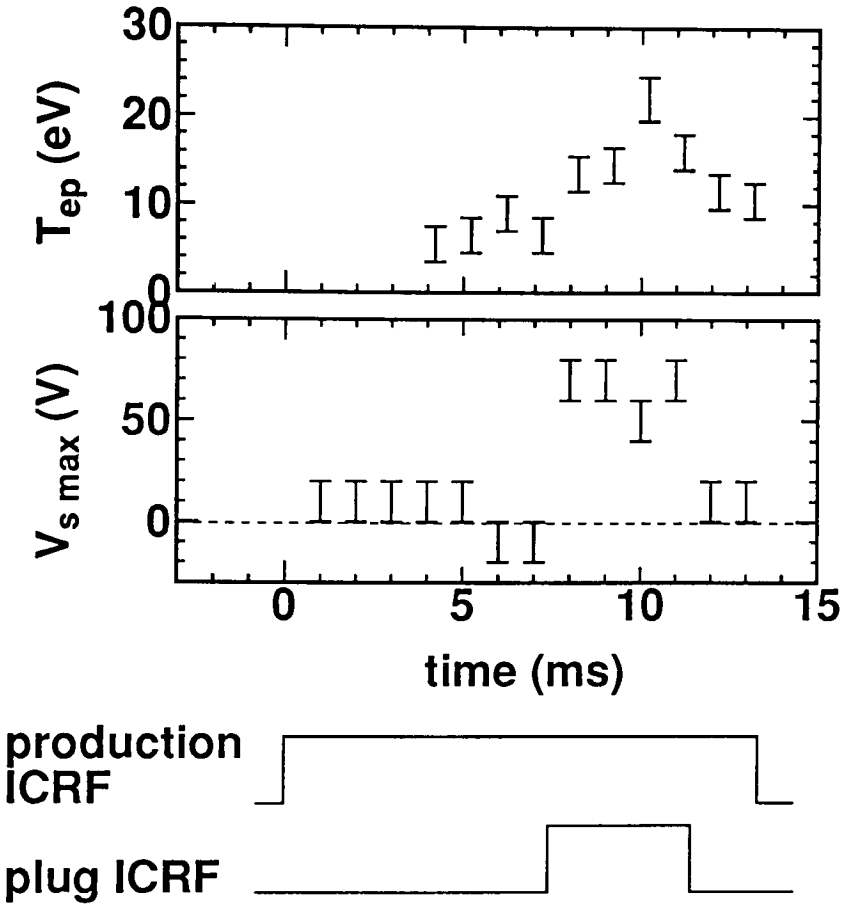

FIG. 5.2.(a) Time evolutions of electron temperature in the plug cell T_{ep} and the maximum plasma potential $V_{s\,max}$. The dotted line represents the case without plug ICRF injection. Timing chart of the ICRF injections are shown below the figure. $\nu_{puff} = 3.6$ %, $B_m = 0.25$ T, and $B_{p0} = 0.092$ T.

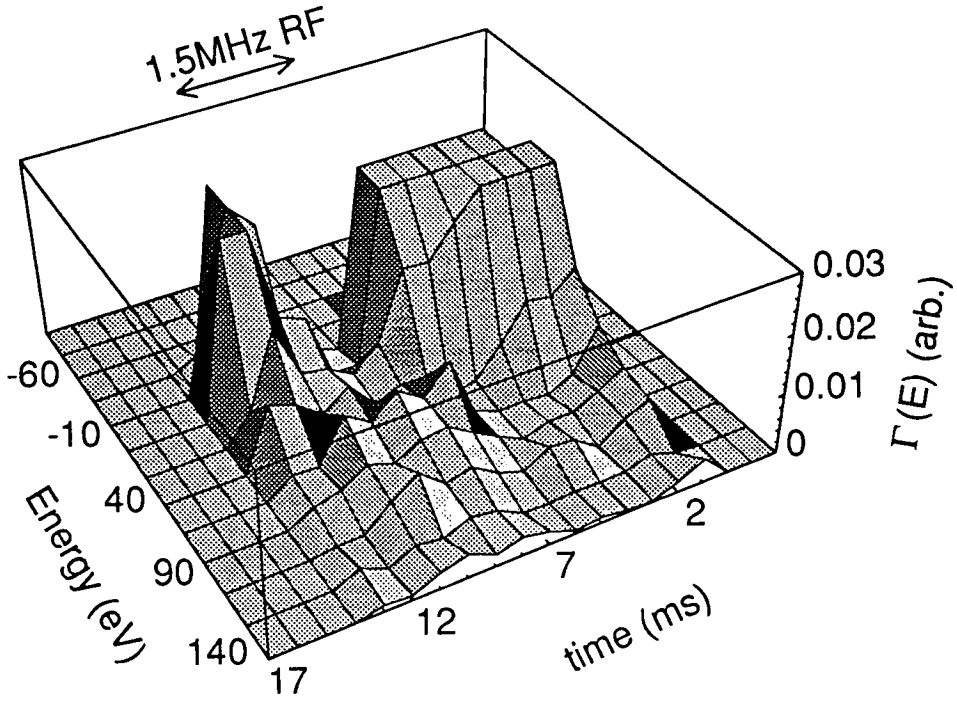

FIG. 5.2.(b) Time evolution of the energy spectra of ion end loss flux Γ_{end}. The data points for $\Gamma_{end}(E) \leq 0.03$ are enlarged. $\nu_{puff} = 3.6$ %, $B_m = 0.25$ T, and $B_{p0} = 0.092$ T.

ICRF, confining potential $\phi_c \sim 75$ V is formed, where $\phi_c = V_s$(the maximum value in the plug cell) $-V_s$(the average value in the central cell). The result of measurement of $V_{s\,max}$ from $\Gamma_{end}(E)$, as shown in Fig. 5.2(a), coincides with ϕ_c by the probe measurement.

We display the dependence of axial particle confinement factor and T_{ep} on strength of the static magnetic field in the midplane of the plug cell B_{p0} in Fig. 5.3. $\tau_{p||N}$ and $\tau_{p||S}$ are defined as $n_{ec}(z = 0)l_z/\Gamma_{end}$ (measured at $z = +210$ cm, "north end") and $n_{ec}(z = 0)l_z/\Gamma_{end}$ (measured at $z = -210$ cm, "south end"), respectively, where l_z is the axial characteristic length of HIEI in the approximation as a cylinder. $\tau_{p||N}$ or $\tau_{p||S}$ represents axial particle confinement factor at each end. The vertical dotted line in Fig. 5.3 indicates the corresponding strength of the magnetic field at the ion-ion hybrid resonance layer B_{ii} (in this case $B_{ii} = 0.104$ T). On the left side of the dotted line the ion-ion hybrid resonance layer is present in the plug cell, while on the right side it is not the case. $\tau_{p||N}$ in the case with the ion-ion hybrid resonance is larger approximately by one order than that without the ion-ion hybrid resonance. As B_{p0} is raised beyond B_{ii}, $\tau_{p||N}$ decreases to the value of the case without injection, which shows that the axial confinement is enhanced only when the ion-ion hybrid resonance is present. T_{ep} in the case with the ion-ion hybrid resonance increases by a factor of ~ 3 in comparison with the case without the plug ICRF injection, which is the direct evidence of electron acceleration by the plug ICRF When the plug electron is heated and the potential hill is formed by ICRF injection, the plug cell density decreases by a factor of ~ 3. This decrease coincides with the reduction of Γ_{end}. T_{ep} decreases when B_{p0} is beyond B_{ii}, which is the similar change to that of $\tau_{p||N}$. It is observed that increase of $\tau_{p||S}$ is limited up to a factor of $\sim$ 1.6, since propagation of the plug ICRF to the "south" plug cell is less than that to the "north" plug cell because of the axial position of the plug ICRF antenna in the central cell. Enhancement of the total axial particle confinement is estimated to be ~ 4.0.

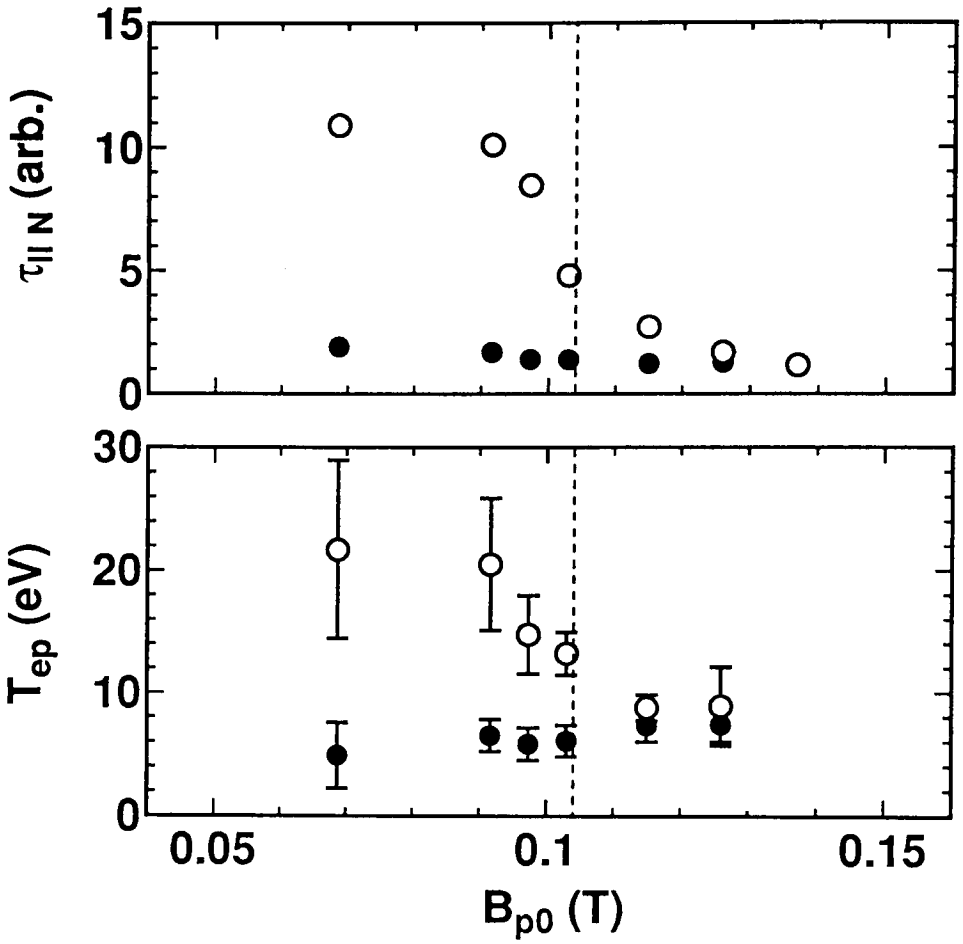

FIG. 5.3. Dependence of $\tau_{p\|N}$ and T_{ep} at $z = 130$ cm on the strength of the static magnetic field in the midplane of the plug cell B_{p0}. The open circles represent the case with plug ICRF injection, and the closed circles represent the case without plug ICRF injection. The vertical dotted line indicates the corresponding strength of the ion-ion hybrid resonance B_{ii}. $\nu_{puff} = 3.6$ %.

To clarify the role of the ion-ion hybrid resonance, critical values of B_{p0} for improved confinement and for electron heating B_{cr} are compared with B_{ii}. The critical strength B_{cr} is defined as the minimum value of B_{p0} for $\tau_{p||N} \sim \tau_{p||N0}$ or $T_{ep} \sim T_{ep0}$, where the subscript 0 indicates the case without the plug ICRF injection. In the case of Fig. 5.3, B_{cr} for $\tau_{p||N}$ is calculated as 0.115−0.120 T, and B_{cr} for T_{ep} is calculated as 0.105−0.120 T. By varying puffed minority ratio ν_{puff}, B_{cr} and B_{ii} are plotted in Fig. 5.4. When ν_{puff} is increased up to 15 % and therefore B_{ii} up to 0.125 T, good consistency is observed between B_{cr} and B_{ii} for $\nu_{puff} > 5$ %. Some discrepancy is present for $\nu_{puff} \leq 5$ %, and it would be due to the difference between ν_{puff} and minority ion concentration caused by recycling hydrogen from the vessel wall, as mentioned in Sec. 5.2.

In order to see what happens near the ion-ion hybrid resonance layer, which plays the essential role on axial confinement and electron heating as shown in Figs. 5.3 and 5.4, measurement of wave propagation is performed. Ref. 4 showed that the parallel wavenumber becomes large and electromagnetic field becomes much smaller near the ion-ion hybrid resonance layer. Figure 5.5 displays RF electric field parallel to the magnetic fields $E_{||}$ measured by a dc-biased dipole antenna. $E_{||}$ becomes large near the ion-ion hybrid resonance layer, which shows enhancement of its amplitude and sequent damping. Relation between the measured $E_{||}$ and T_{ep} will be discussed in Sec. 5.4.

Figure 5.6 shows ion-confining potential ϕ_c as a function of T_{ep}. As T_{ep} is increased, ϕ_c increases up to 0.13 kV in this parameter range. Enhancement of $E_{||}$ is observed, as shown in Fig. 5.5, and One possible interpretation is that, since electron heating via Landau damping of the observed $E_{||}$ takes place and that this increase of ϕ_c can result from the rise of T_{ep} through the modified Boltzmann relation. However, if RF field $E_{||}$ induces the velocity space diffusion and electron velocity distribution function becomes non-Maxwellian, enhancement of ϕ_c from the modified Boltzmann relation is possible.

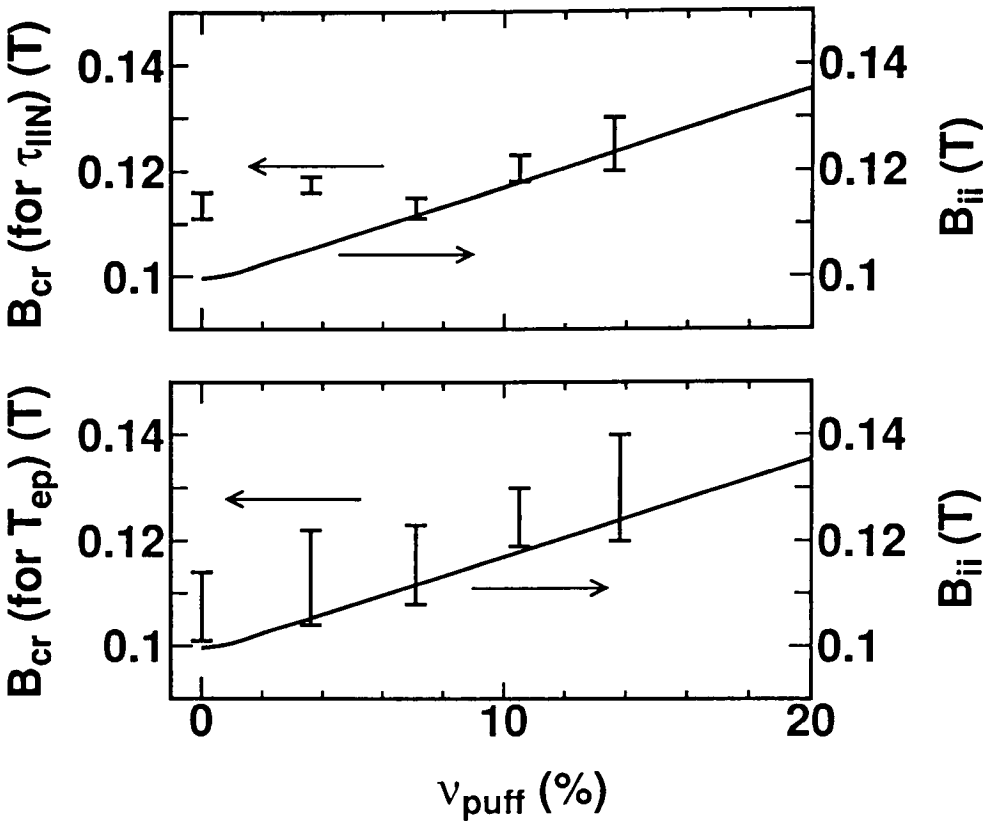

FIG. 5.4. Comparisons of B_{cr} with B_{ii} for $\tau_{p||N}$ and for T_e. The vertical error bars show B_{cr} obtained from experimental results, and the solid curve indicates B_{ii} on the assumption that ν_{puff} represents the minority ion ratio.

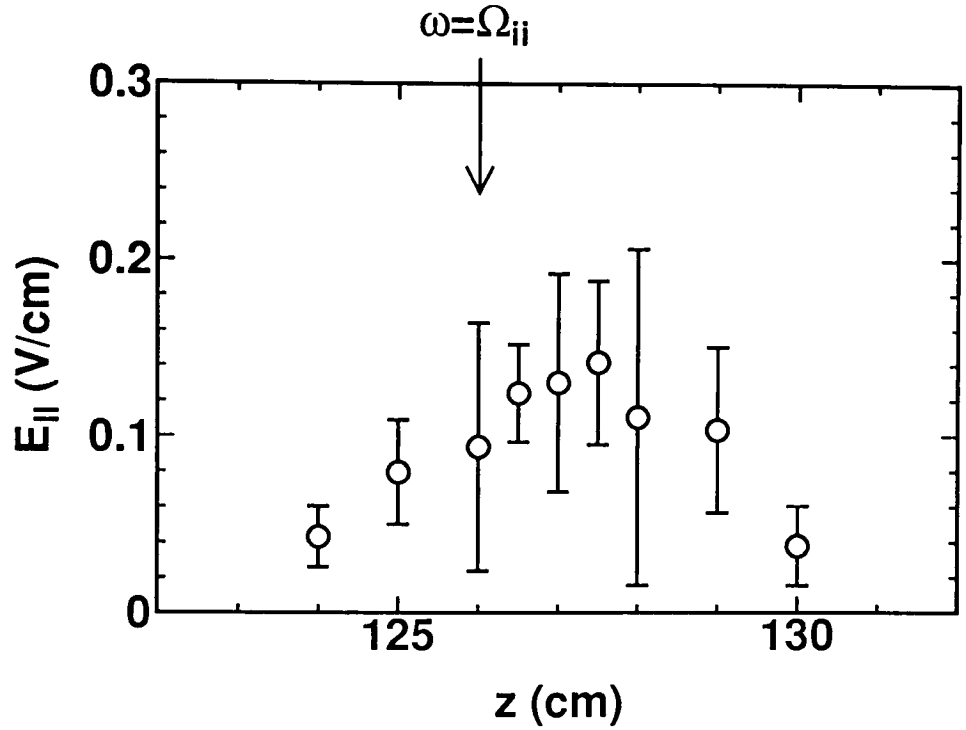

FIG. 5.5. Axial profile of $E_{||}$ measured by a dc-biased dipole antenna with a high impedance AC coupler. $\nu_{puff} = 6.0$ %, $B_m = 0.27$ T, and $B_{p0} = 0.10$ T.

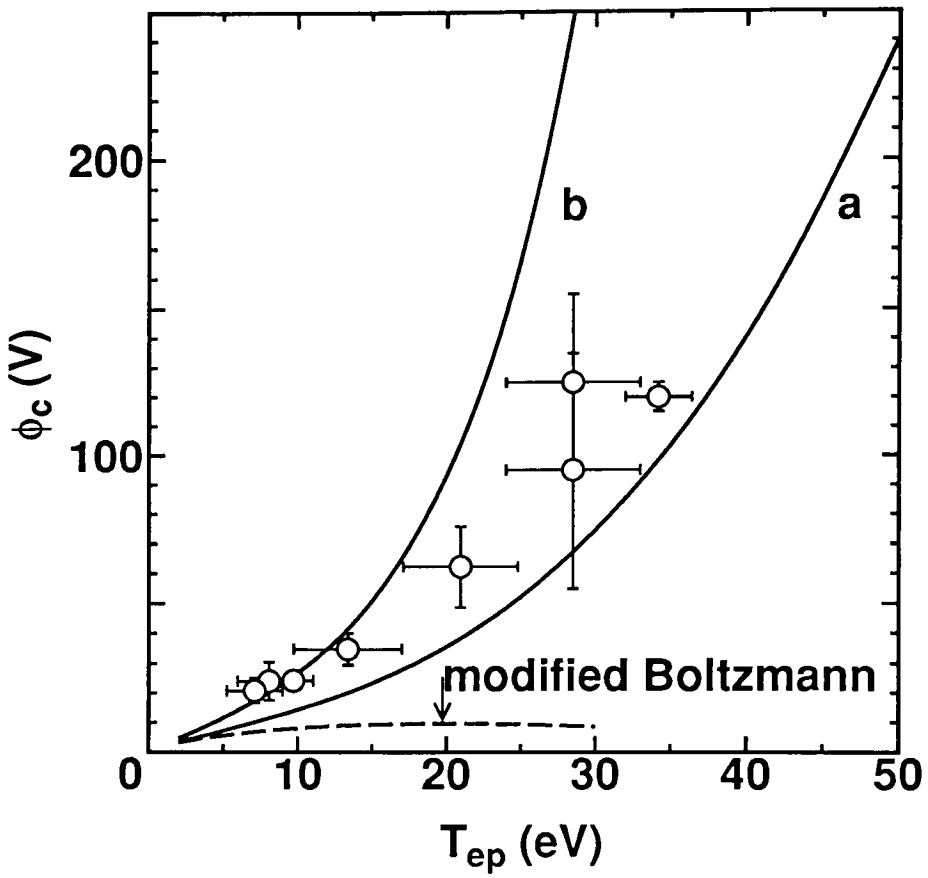

FIG. 5.6. Ion confining potential ϕ_c as a function of T_{ep} with the theoretical scaling law. The open circles are the experimental data points. Solid curves are calculated by Eq. 5.2 on ϕ_c with RF-induced electron velocity diffusion. A dotted curve indicates the modified Boltzmann relation. Used parameters are in the following. T_u = 15 eV, τ_{p0} = $\tau_{p\perp 0}$, $E_{||}$ = 0.20 V/cm at T_t = 20 eV, and n_t/n_u = 2.0 for curve (a) and n_t/n_u = 3.5 for curve (b).

Dependence of ϕ_c on T_{ep} will be discussed in detail in Sec. 5.4 in comparison with theoretical prediction.

5.3.2 High-beta plasma production with enhanced axial and radial confinement

Effects of simultaneous enhancement of axial and radial confinement are examined using the plug ICRF and limiter biasing. In this experiment, the strength of the static magnetic field at the mirror point B_m is 0.19 T with the mirror ratio 7.1 in the standard operation. The parameters of the central cell plasma in typical discharges before the plug ICRF injection and the limiter biasing are similar as those described in Sec. 5.2 and Sec. 5.3.1.

Figure 5.7 shows the time evolution of diamagnetic flux W_{dia} and beta value $\beta_\perp$ in the application of the limiter biasing and the plug ICRF After the limiter biasing ($\sim$ +120 V) is imposed, W_{dia} increases by a factor of $\sim$ 1.5. When the plug ICRF is injected, increase of W_{dia} is a factor of $\sim$ 2.5 from the value in the phase of the production ICRF only. n_{ec} produced by the production ICRF remains 2.0×10^{12} cm^{-3}, while n_{ec} increases to 1.0×10^{13} cm^{-3} in the phase of the combination of the plug ICRF and the limiter biasing. Minority heating is observed during the plug ICRF injection and $T_{H\perp}$ rises up to 70 eV by a factor of 2.5, whereas $T_{He\perp}(\sim$ 30 eV) shows no change by the plug ICRF injection. T_e in the central cell rises from 7$-$10 eV to 10$-$13 eV by the plug ICRF. As a result, the beta at the core $\beta_\perp$ is estimated to be $\sim$ 12 % in the case of the plug ICRF injection and the limiter biasing, where $\beta_\perp$ is obtained from n_e and T_e at $z = 0$ cm, and $T_{H\perp}$ and $T_{He\perp}$ at $z = -60$ cm which are converted into the values at $z = 0$ cm on the assumption of conservation of the magnetic moment.

Figure 5.8 shows $\beta_\perp$ in various conditions as a function of W_{dia}. The experimental

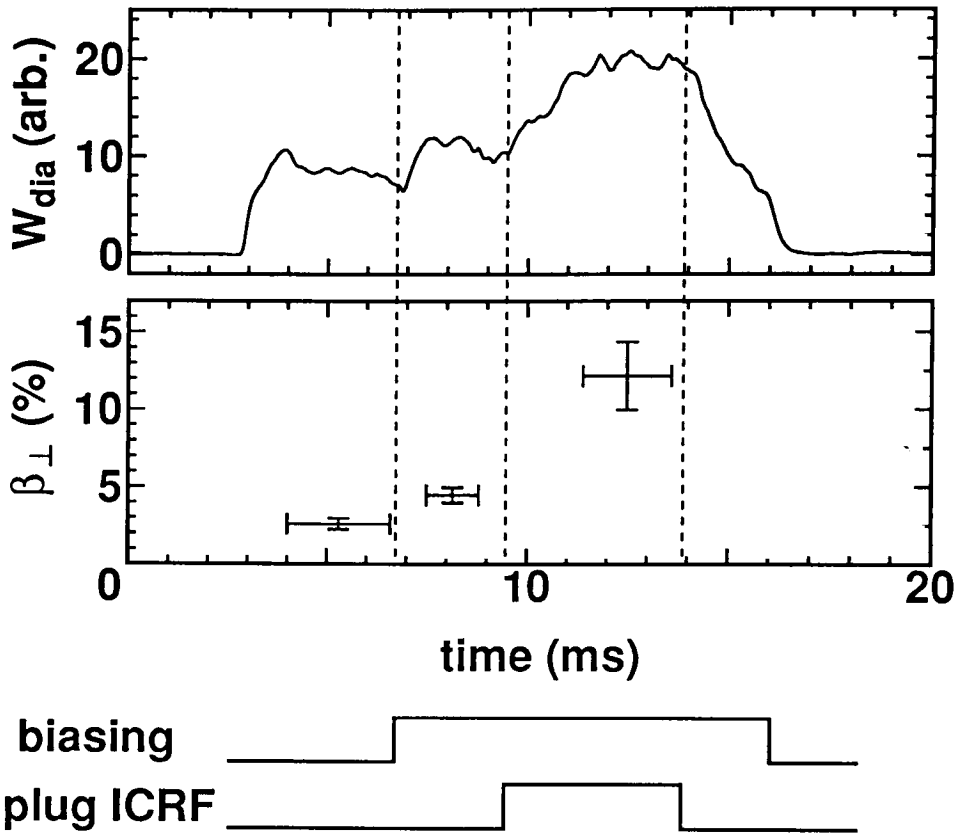

FIG. 5.7. Time evolution of W_{dia} and $\beta_\perp$ in the application of the limiter biasing and the plug ICRF The values of beta are obtained from n_e and $T_{e\perp}$ at $z = 0$ cm, and $T_{H\perp}$ and $T_{He\perp}$ measured by TOF $\nu_{puff} = 6.2$ %, $B_m = 0.19$ T, $R_m = 7.1$, and limiter bias voltage $V_{bias} \sim 120$ V.

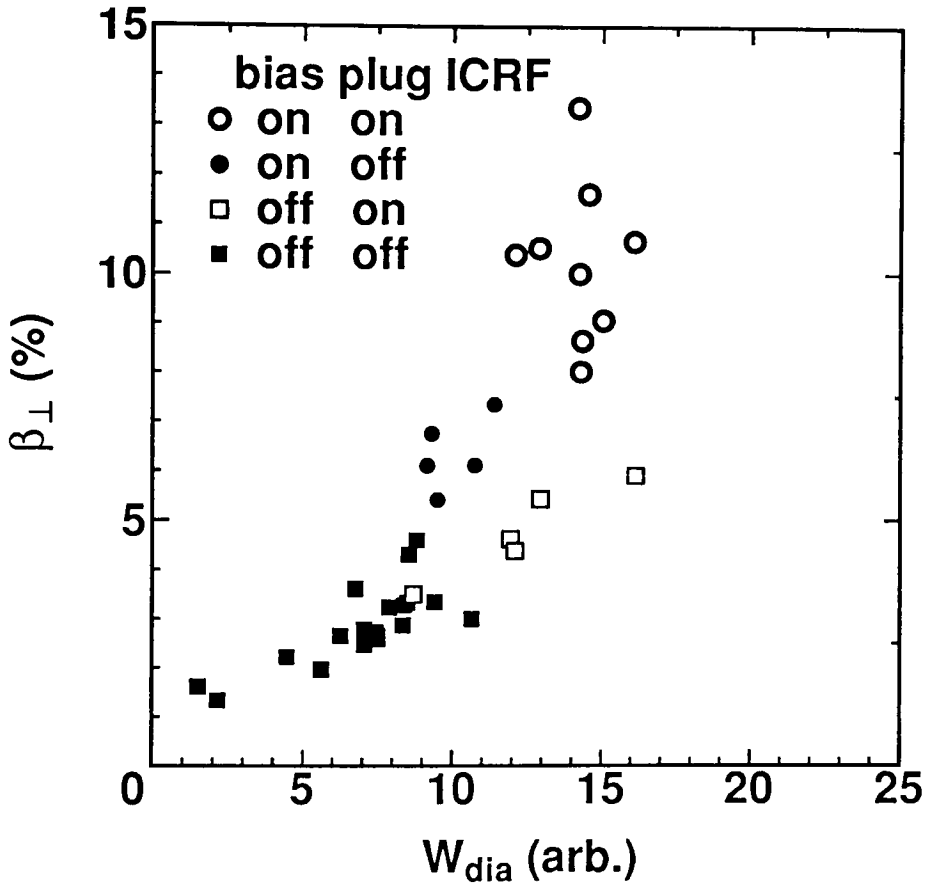

FIG. 5.8. $\beta_\perp$ in various conditions as a function of W_{dia}. ν_{puff} = 6.2 %, B_m = 0.19 T, and B_{p0} = 0.068 T.

points for the case with the production ICRF only (closed squares) are linearly changing by variation of its net input power. The data points for the plug ICRF injection without limiter biasing (open squares) are on the extrapolation of the case with the production ICRF only. By application of the limiter biasing, the data points moves to the upper side of beta, and the maximum beta value obtained is 13.6 % in the case with the plug ICRF and with the limiter biasing. Such a shift of the characteristic line is considered to be due to peaking of pressure profile by the limiter biasing. Simultaneously density profile in the edge (including the scrape-off layer) changes significantly by the limiter biasing. For radial positions inside the limiter edge, density increases by the limiter biasing. On the contrary, in the scrape-off layer (the limiter shadow), density decreases by a factor of 3–5. As a result, radial density profile in the edge is steepened by the limiter biasing. E-folding length of the radial density profile λ_n in the case with the plug ICRF and without the limiter biasing is 2.0 cm, while λ_n in the case with both the plug ICRF and the limiter biasing is 0.7 cm. This steepening is due to the enhancement of the radial particle confinement.

Change of the energy confinement time can be estimated from the time evolutions of W_{dia} in the following. It is assumed that the axial energy confinement time $\tau_{E\parallel}$ increases by the injection of the plug ICRF, and that the radial energy confinement time $\tau_{E\perp}$ increases by the application of the limiter biasing. Change of $\tau_{E\perp}$ by the plug ICRF or that of $\tau_{E\parallel}$ by the limiter biasing can be negligible since neither change of the radial density profile in the periphery by the plug ICRF nor change of the axial particle confinement factor by the limiter biasing in the previous measurements are observed. The global power balance equation is expressed as

$$\frac{dW}{dt} = P - \frac{W}{\tau_E}, \tag{5.1}$$

where W is the stored energy and P is the input power. From this equation, time

dependence of W_{dia} is estimated to be $1 - \exp(-t/\tau_E)$ and $\exp(-t/\tau_E)$ just after the plug ICRF or the limiter biasing is turned on and off, respectively. One more assumption is used that enhancement of $\tau_{E\|}$ is 4.0, which comes from the fact that enhancement factor of the total axial particle confinement is 4.0. This assumption may be valid since most of the axial energy loss in a mirror device is a convective one. Using several shots of W_{dia} and the above assumptions, the enhancement of the global energy confinement time $\tau_E = (\tau_{E\|}{}^{-1} + \tau_{E\perp}{}^{-1})^{-1}$ is estimated as 3.9 (from 0.33 msec to 1.3 msec). This enhancement is realized by the combination of the plug ICRF injection and the limiter biasing. $\tau_{E\|}$ is estimated to change from 1.1 msec to 4.4 msec, and $\tau_{E\perp}$ is enhanced by a factor of 3.8 (from 0.47 msec to 1.8 msec).

5.4 Discussion

5.4.1 Scaling of axial confinement and identification of mode conversion

The observed ϕ_c as a function of T_{ep} is displayed with the modified Boltzmann relation [17] in Fig. 5.6. Increase of ϕ_c does not agree with this theoretical prediction (dashed line). Another mechanism including an effect of RF-induced electron velocity space diffusion [18] is taken into consideration for explanation of these experimental results. Starting point of this theory is the particle transport equations for electrons in the plug cell with the effects of radial diffusion by some fluctuations and RF-induced velocity space diffusion. The relation between trapped electron density in the plug region n_t and untrapped electron density n_u (where the plug cell density $n_{ep} = n_t + n_u$) is expressed in the "improved" modified Boltzmann relation which includes the effects of RF-induced velocity space diffusion parallel to the static magnetic field. Such diffusion will take place under the presence of large parallel RF electric field $E_{\|}$ that results in Landau damping.

Dependence of ϕ_c on $T_t(\sim T_{ep}$, the electron temperature in the plug region) is derived as

$$\frac{e(\phi_c + \phi_b)}{T_t} = \frac{1}{\lambda}[\frac{n_t}{n_u}\sqrt{\frac{T_u}{T_t}}(1 + \frac{\tau_{p0}}{\tau_{p\perp 0}})]^{\lambda} - 1, \tag{5.2}$$

where τ_{p0} indicates the axial confinement time in the plug cell $\tau_{p||}$ at r = 0 cm, and the radial confinement time in the plug cell $\tau_{p\perp 0}$ is assumed to be equal to τ_{p0}. λ is the ratio of the RF-induced velocity space ($v_{||}$) diffusion to the classical one and is determined by $E_{||}$, T_t, n_t, and the applied RF frequency. The dependence of T_t on n_t experimentally was examined in advance, and obtained empirical relation is used for derivation of n_t as a function of T_t ($n_t[\mathrm{cm}^{-3}] = 1.32 \times 10^{12}(T_t[\mathrm{eV}])^{-1/2}$). Such relationship between T_t and n_t is determined by the power balance of the trapped electrons and escaping rate from the trapped region, and the escaping results from both pumping-out by acceleration with $E_{||}$ and shift into the plug cell loss cone by collisions. The calculated curves using the above equation are shown as solid lines in Fig. 5.6. Here spontaneous formation of thermal barrier ϕ_b is assumed to $0.75 \times T_{ep}/e$ in this calculation. The experimental points (open circles) are in an agreement with the theoretical curves. In these experiments $E_{||}$ (measured as 0.1−0.2 V/cm in Fig. 5.5) would be produced via mode conversion from the fast wave to an electrostatic wave at the ion-ion hybrid resonance layer. The RF-induced velocity space diffusion is considered to play a role to enhance the ion confining potential.

Electron acceleration and heating in the plug cell take place in the presence of the ion-ion hybrid resonance layer. Resonance of the injected fast wave with the plug cell electrons is examined using theoretical analysis. Fig. 5.9(a) displays the parallel dispersion relation of the cold two-ion-species cylindrical plasma [15] with the minority (H) ion concentration 5 %. Here the solid lines denote the branch of the fast magnetosonic wave, the dashed line indicates the slow ion-cyclotron wave with the lowest radial order, and the dotted region is an new emerging branch which is discussed later. In the case of the low-field side incidence, the fast magnetosonic wave converts into the slow ion-cyclotron wave via

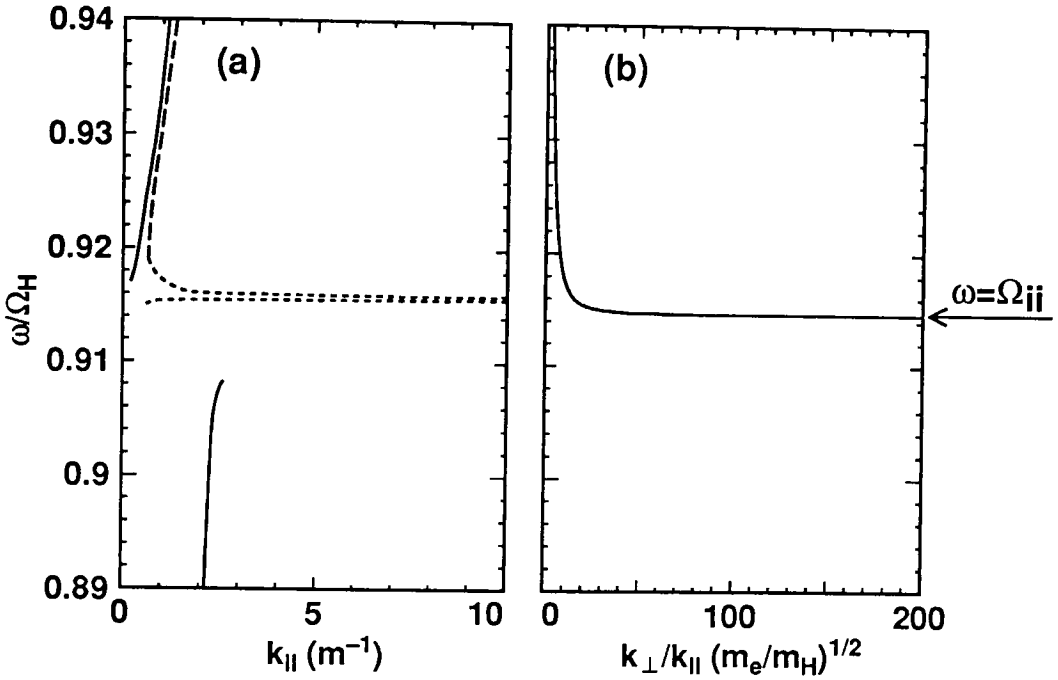

FIG. 5.9. (a) Dispersion relation of ICRF waves near the ion-ion hybrid resonance. The parameters for calculation is as follows: $m = -1$, $n_e = 5.0 \times 10^{11}$ cm^{-1}, $r_w = 25.0$ cm, and $r_p = 9.0$ cm. The solid line indicates the fast magnetosonic wave, the dashed line the slow ion-cyclotron wave with the lowest radial order, and the dotted line is the cold electrostatic ion-cyclotron wave. (b) Ratio of the parallel and perpendicular wave number near the ion-ion hybrid resonance layer calculated by Eq. 5.3. Here the parameters for calculation is as follows: $n_e = 5.0 \times 10^{11}$ cm^{-1}, $T_e = 20$ eV, and $\omega/k_{||}V_e = 3.5$.

the reflection at the ion-ion hybrid resonance layer [15]. In the case of the high-field side incidence (from the lower side in Fig. 5.9(a)), the fast wave branch shows a slight change to larger $k_{||}$ values in the vicinity of the ion-ion hybrid resonance layer. It is considered to continue to a new branch just beyond the ion-ion hybrid resonance layer through the narrow tunneling region. The new branch, which is a continuous one from the slow ion-cyclotron wave, shows some resonance just above the ion-ion hybrid resonance. Ono [19] derived the cold electrostatic ion-cyclotron wave just beyond the ion-ion cyclotron resonance theoretically. Starting from the dispersion relation in a hot plasma and using some approximations, the dispersion relation near the ion-ion hybrid resonance is written as [19]

$$1 + \left[1 + \frac{\omega}{k_{||}V_e} Z\left(\frac{\omega}{k_{||}V_e}\right)\right] \frac{{\omega_{pe}}^2}{{k_\perp}^2 + {k_{||}}^2} \frac{m_e}{T_e} + \sum_{\alpha=e,H,He} \frac{{\omega_{p\alpha}}^2}{{\Omega_\alpha}^2 - \omega^2} \frac{{k_\perp}^2}{{k_\perp}^2 + {k_{||}}^2} = 0. \qquad (5.3)$$

Here Z is the plasma dispersion function, $V_e = (2T_e/m_e)^{1/2}$, $k_\perp$ is the perpendicular wavenumber, $\omega_{p\alpha}$ and Ω_α are the plasma and the cyclotron frequencies respectively, and m_e is the electron mass. When $\omega/k_{||}V_e \gg 1.0$, Eq. 5.3 reduces to the expression of the general cold dispersion relation which is used to obtain the branches in Fig. 5.9(a). Figure 5.9(a) shows that the phase velocity of the wave on this new branch gets into the region of $\omega/k_{||}V_e \sim 1.0$ with $T_e = 20$ eV for $k_{||} \geq 3.5$ m^{-1} Figure 5.9(b) shows the ratio of the parallel and perpendicular wave number near the ion-ion hybrid resonance layer calculated by Eq. 5.3. This represents that this wave shows the electrostatic nature where the branch is close to the ion-ion hybrid resonance. The new emerging branch just beyond the ion-ion hybrid resonance is then identified as an electrostatic mode. The observed large $E_{||}$ near the ion-ion hybrid resonance layer is consistent with this theoretical analysis predicting the branch of the electrostatic wave. Ono also presented the experimental results of electron Landau damping of this wave [19].

5.4.2 Model description of enhancement of two-dimensional confinement

Simultaneous application of ICRF-enhanced potential in the plug cell and DC field in the radial edge of the central cell creates a high-beta plasma with enhancement of the global energy confinement ~4.0, where no clear interaction between changes of axial and radial confinement is observed. Here such an interaction is analyzed theoretically in two cases: without and with the plug ICRF injection.

In the case without the plug ICRF injection, which has been shown in Chap. 4, the central cell is in a positive potential with respect to the plug cell due to density difference. Assumed that axial potential is constant in one cell and potential difference ϕ_d is present near the mirror point, the condition for electron current to be zero is written as

$$n_{ec} \sin^{-1}\left(\frac{1}{R_{mc}^{1/2}}\right)\left(\frac{T_e}{m_e}\right)^{1/2} = n_{ep} \sin^{-1}\left(\frac{1}{R_{mp}^{1/2}}\right)\left(\frac{T_e + e\phi_d}{m_e}\right)^{1/2}, \qquad (5.4)$$

where T_{ec} is electron temperature in the central cell, and the mirror ratio of the central cell R_{mc} is 7.1 and that of the plug cell R_{mp} is 2.6 in the HIEI standard operation. Since there is no electron heating source and no thermal barrier, electron temperature is constant in the axial direction throughout the device. ϕ_d is determined from the Boltzmann relation as $e\phi_d = T_e ln(n_{ec}/n_{ep})$ with Eq. 5.4. Electron flux from each cell to another is balanced when $n_{ec}/n_{ep} = 2.4$, and ϕ_d is 8.5 V with T_e 10 eV

The axial particle confinement time $\tau_{p||}$ is derived with Eqs. 2.4 and 2.5, and the global particle balance is expressed by Eq. 4.1. As n_{ec} increases according to enhancement of the radial particle confinement time $\tau_{p\perp}$ that can be assumed to be proportional to a^2/D with the radial diffusion coefficient D, $\tau_{p||}$ decreases gradually with constant T_e. Such tendency is displayed in Fig. 5.10, where production source S is assumed to be linearly changed with radial loss flux ($n_{ec}/\tau_{p\perp}$). $\tau_{p\perp}$ jumps up to the higher branch at the transition point, whereas $\tau_{p||}$ gradually decreases. However, its degradation is too small to be detected in experiments, and almost no effect to the global confinement. As a result, n_{ec} increases by

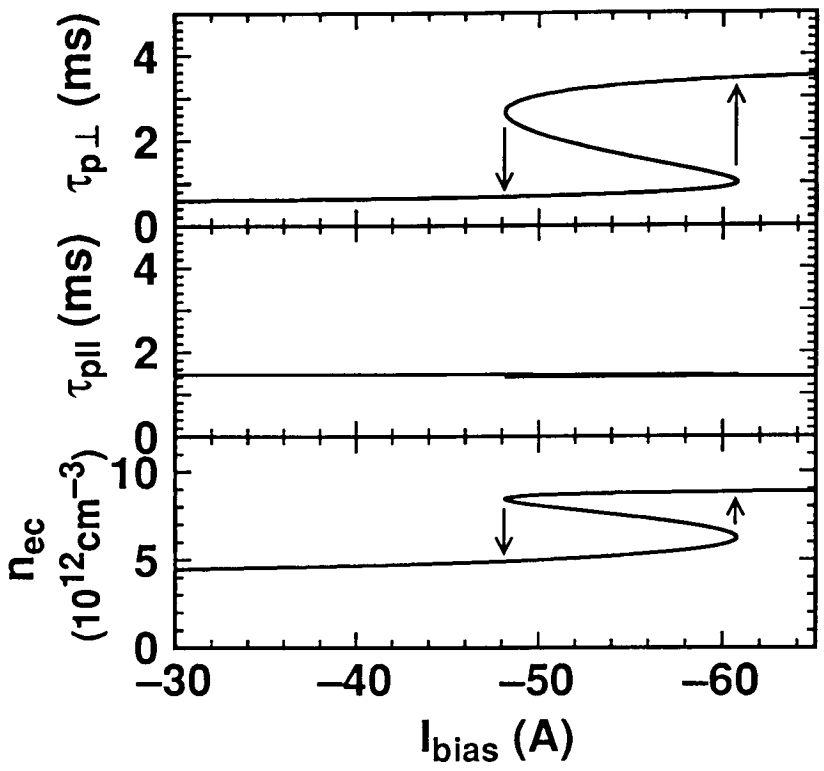

FIG. 5.10. Analytical result of changes of $\tau_{p\perp}$, $\tau_{p||}$, and n_{ec} as a function of biased limiter current I_{bias}. The same parameters are used as in Fig. 4.8(b). The potential difference between the central and the plug cells ϕ_d is assumed to be 8.5 V Other parameters are as follows: $T_{ic} = 30$ eV, $T_{ec} = 10$ eV, and $S \sim 1 \times 10^{16}$ cm^{-3} and is changed linearly with $n_{ec}/\tau_{p\perp}$.

a factor of 1.5−2.0, which was observed experimentally.

When n_{ec} increases, ion diamagnetic drift velocity, which is proportional to dn_{ec}/dr with constant T_{ec}, becomes large, so that it may affect dv_θ/dr in the edge. However its contribution of v_θ is approximately by one order smaller than that of $E \times B$ drift velocity induced by limiter biasing in the experiment, and is neglected in the above calculation. If the end plate is grounded, axial potential profile (ϕ_d) is strongly linked to radial potential profile (dv_θ/dr), and confinement in each direction affects each other, although the end plates are completely floating in this experimental regime.

In the case of the plug ICRF injection, thermal barrier is spontaneously formed in the vicinity of the mirror point between the central and the plug cells, and values of electron temperature are different in both cells. If n_{ec} increases, ϕ_b becomes large for electron current to be zero, where $\phi_c + \phi_b$ is constant. In this case electron flux from each cell is derived from the integration of velocity distribution function in the loss cone of the electron velocity space with the energy above zero at the bottom of thermal barrier. When ϕ_b increases, ϕ_c decreases and axial confinement is degraded. Formation of ϕ_c or ϕ_b does not affect radial profile of potential in the central cell since no significant radial electric field in the plug cell in the scheme of ICRF-induced potential.

Figure 5.11 shows such tendency schematically, where $\phi_c + \phi_b$ is according to the improved modified Boltzmann relation with $n_t/n_u = 3.0$. ϕ_b is assumed to be $0.75 \times T_{ep}/e$ with $n_{ec} = 5.0 \times 10^{12}$ cm^{-3} and to change proportionally to $\ln(n_{ec})$. As I_{bias} is increased and consequently $\tau_{p\perp}$ gradually increases, transition from A to B takes place due to jump of dv_θ/dr with rapid enhancement of radial confinement and drop of $\tau_{p\parallel}$ to 70 % of the initial value. However no degradation of axial confinement was observed in the previous experiment, and some effect included in the transition may enhance axial confinement (B to C, or A to C). Bifurcation of radial transport might reinforce axial confinement, for

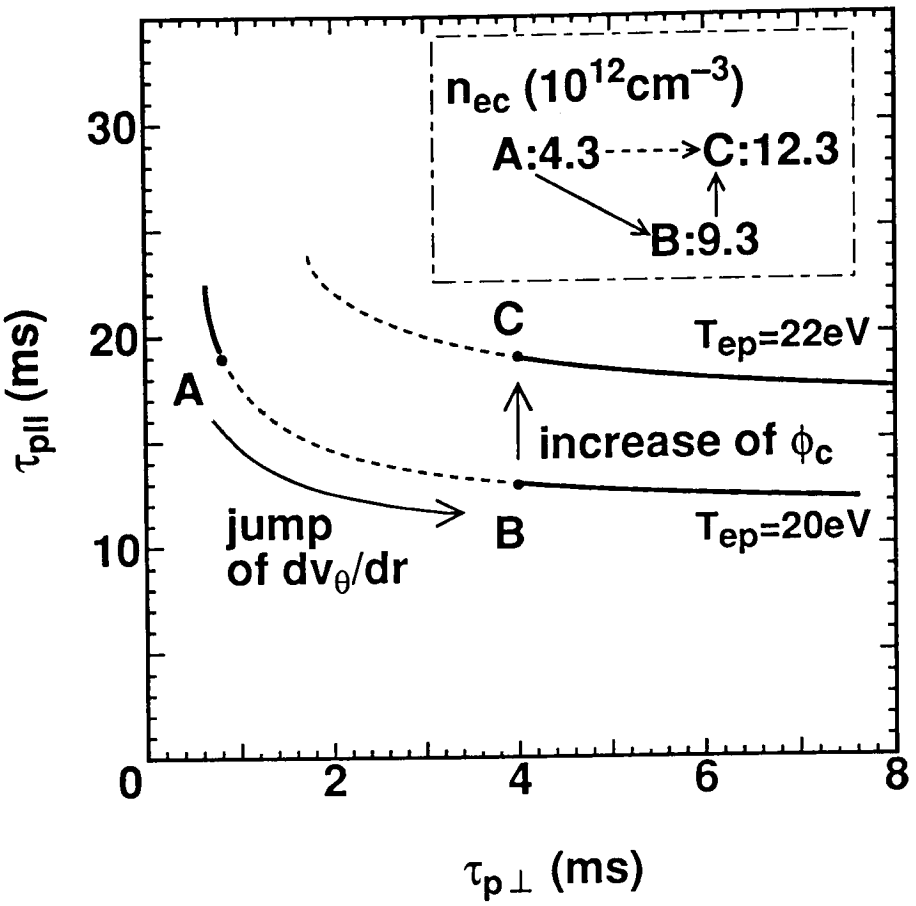

FIG. 5.11. Relation between $\tau_{p\parallel}$ and $\tau_{p\perp}$ as a function of n_{ec} with constant T_{ep}. Two cases are shown: T_{ep} = 20 eV and T_{ep} = 22 eV The values of n_{ec} at three points (A, B, C) are shown in the inset of the figure. Used parameters are as follows: T_{ic} = 30 eV, T_{ec} = 15 eV, and $S \sim 5 \times 10^{15}$ cm^{-3} and is changed linearly with $n_{ec}/\tau_{p\perp}$.

instance, by further plug electron heating due to increase of mode conversion rate to the electrostatic mode, or due to enhancement of the fast wave propagation, with the change of n_{ec}.

5.4.3 Beta limit against the flute mode instability

The simultaneous enhancement of the axial and radial confinement realizes a high-beta ($\beta \geq 10$ %) plasma production. Here beta limit against the flute interchange mode [20, 21] is derived for this experimental parameter, and it is compared with the experimental results. Stability condition against the flute interchange mode is expressed as

$$\int_{-l}^{l} \frac{dz}{B} \kappa_\psi P(z) \geq 0, \tag{5.5}$$

where l is the length from the midplane to the mirror point of the central cell, $\boldsymbol{\kappa} = (\boldsymbol{b} \cdot \boldsymbol{\nabla})\boldsymbol{b} = \kappa_\psi \boldsymbol{\nabla}\psi + \kappa_\theta \boldsymbol{\nabla}\theta$, the external static magnetic field $\boldsymbol{B} = B\boldsymbol{b} = \boldsymbol{\nabla}\psi \times \boldsymbol{\nabla}\theta$, and $P(z)$ is the plasma pressure. In the case of HIEI, $\kappa_\psi(z)$ includes the effect of the ponderomotive force F_p ($\kappa_{\psi Fp}$) as well as curvature of the magnetic field itself ($\kappa_{\psi 0}$). F_p for electrons (F_{pe}) is much larger than that for ions in this experimental regime, that is, the applied ICRF frequency for stabilization ($\omega/2\pi = 8$ MHz) and the magnetic field strength in the central cell. F_{pe} by rotating fields is obtained as

$$\boldsymbol{F}_{pe} = -\frac{e^2}{m_e \omega} \left(\frac{\boldsymbol{\nabla}|\boldsymbol{E}_-|^2}{(\omega + \Omega_e)} + \frac{\boldsymbol{\nabla}|\boldsymbol{E}_+|^2}{(\omega - \Omega_e)} \right), \tag{5.6}$$

where $|\Omega_e|$ is the electron cyclotron frequency and $\Omega_e \leq 0$. The contribution of the axial component of RF electric field $\boldsymbol{E}_z$ is neglected since it is much smaller than the right-circularly-polarized field $\boldsymbol{E}_-$ and the left-circularly-polarized field $\boldsymbol{E}_+$ in this frequency range. When the m $= -1$ (right-rotating) fast magnetosonic wave propagates, amplitude of E_- prevails that of E_+ approximately by a factor of 3. $\kappa_{\psi Fp}$ is derived as

$$F_p \sim qT\kappa_{\psi Fp}, \tag{5.7}$$

where $T = T_{ec} + T_{ic}$. Figure 5.12 shows the axial profiles used for derivation of the stability criteria. The profile of the pressure $P(z)$ is calculated from the axial density profile measured in the central cell and the temperature profile derived from T_{ec} and T_{ic} measured at $z = 0$ cm and $z = -60$ cm on the assumption of the conservation of the magnetic moment. $F_p(= F_{pe})$ is calculated using a two-dimensional ICRF code [13] with the antenna current of the production ICRF $I_A = 60$ A, and κ_ψ along the magnetic field line through r = 6 cm at z = 0 cm is derived. Calculation of Eq. 5.5 reveals that these profiles are in the stable region against the flute mode. The critical value of I_A for stability is $\sim$ 30 A, whereas I_A in the experiment ranges 100−150 A. It can be concluded that the produced high-beta plasma is below the beta limit against the flute interchange mode.

5.5 Conclusion

The enhanced axial confinement of a two-ion-species plasma by ICRF waves have been presented. With the injection of the plug ICRF in the central cell, the ion confining potential is formed in the plug cell and the ion end loss flux is significantly reduced. Simultaneously the rise of the electron temperature in the plug cell and the increase of the density in the central cell were observed. The enhancement factor of the axial particle confinement is estimated to be 4.0. The regime of the improved axial confinement has been observed in the case with the ion-ion hybrid resonance layer in the plug cell. The ICRF wave (the fast magnetosonic mode) transmitting to the plug cells encounters the ion-ion hybrid resonance from the high-field side, and it would convert into an electrostatic mode which gives rise to a large $E_{\|}$. One candidate of this electrostatic mode is the cold electrostatic ion-cyclotron wave which is enhanced near the ion-ion hybrid resonance. The experimental results are in an agreement with the theory on the potential enhancement by RF-induced velocity space diffusion.

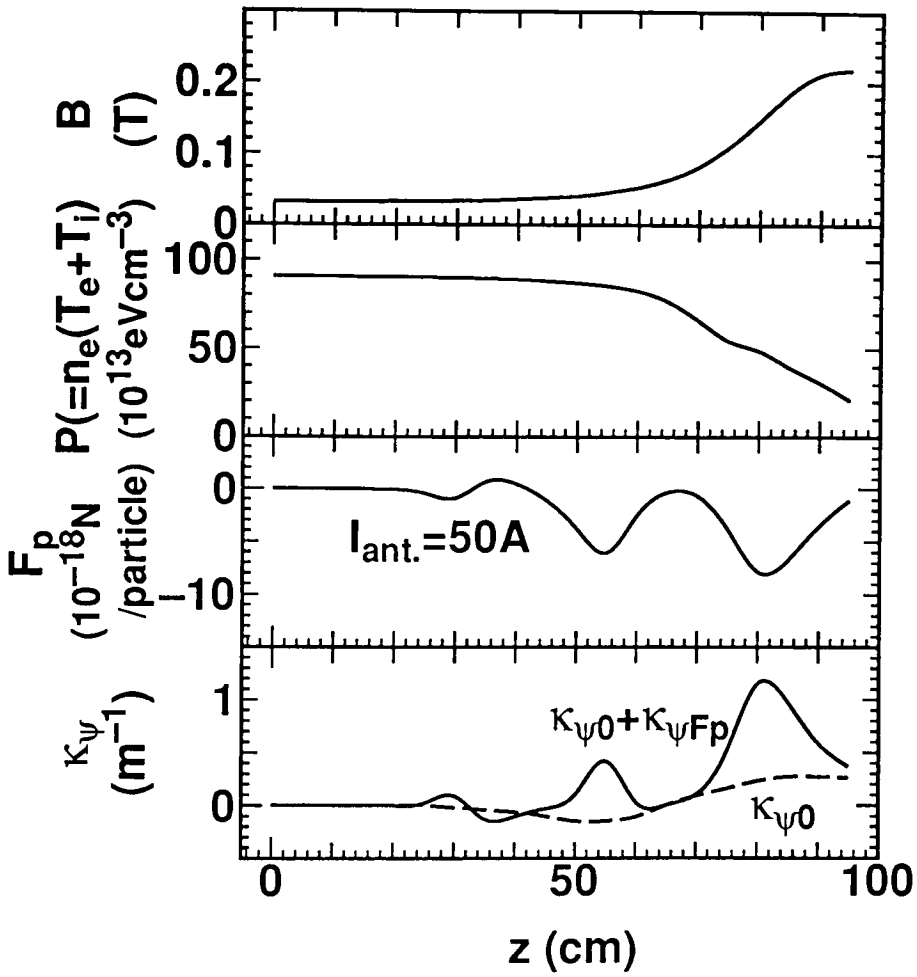

FIG. 5.12. Axial profiles of B, the plasma pressure P, the RF ponderomotive force F_p, and effective curvature κ_ψ. F_p is calculated by the 2-dimensional ICRF code [13] with $I_A = 60$ A.

In the experiment using both the plug ICRF and the limiter biasing, we have demonstrated a high-beta operation in which $\beta \geq 10$ % in the central cell. The radial energy confinement is enhanced by a factor of 4 using the limiter biasing, and the global energy confinement is estimated to be enhanced by a factor of 4 due to the applications of the plug ICRF and the limiter biasing. Simple model for description of simultaneous enhancement regime is proposed, and interaction between axial and radial confinement is discussed. The calculation of the stability criteria against the flute interchange mode shows that such a high-beta plasma is in the stable region with the effects of the ponderomotive force of propagating ICRF waves.

References

[1] M. Inutake, T. Cho, M. Ichimura, K. Ishii, A. Itakura, I. Katanuma, Y Kiwamoto, Y Kusama, A. Mase, S. Miyoshi, Y. Nakashima, T. Saito, A. Sakasai, K. Sawada, I. Wakaida, N. Yamaguchi, and K. Yatsu, Phys. Rev. Lett. **55** (1985) 939.

[2] N. Hershkowitz, B. A. Nelson, J. Johnson, J. R. Ferron, H. Persing, C. Chan, S. N. Golovato, and J. D. Callen, Phys. Rev. Lett. **55** (1985) 947, J. R. Ferron, R. Goulding, B. A. Nelson, T. Intrator, E. Y Wang, G. Severn, N. Hershkowitz, D. Brouchous, J. Pew, R. A. Breun, and R. Majeski, Phys. Fluids **30** (1987) 2855.

[3] D. Smith, K. Brau, P Goodrich, J. Irby, M. E. Mauel, B. D. McVey, R. S. Post, E. Sevillano, and J. Sullivian, Phys. Fluids **29** (1986) 902.

[4] Y Yasaka, O. Sakai, H. Takeno, and H. Hojo, Nucl. Fusion **34** (1994) 1263.

[5] M. Inutake, T. Tamano, T. Cho, M. Hirata, H. Hojo, M. Ichimura, K. Ichii, A. Itakura, I. Katanuma, Y. Kiwamoto, A. Mase, S. Miyoshi, Y Nakashima, T. Saito, N. Yamaguchi, K. Yatsu, Y. Yasaka, O. Sakai, M. Shima, H. Yoshida, and R. Itatani, in *Plasma Physics and Controlled Nuclear Fusion Research*, (IAEA, Vienna, 1993), Vol.2, p.651.

[6] S. I. Itoh and K. Itoh, Phys. Rev. Lett. **60** (1988) 799.

[7] K. C. Shaing and E. C. Crume, Jr, Phys. Rev. Lett. **63** (1989) 2369.

[8] A. Mase, J. H. Jeong, A. Itakura, K. Ishii, M. Inutake, and S. Miyoshi, Phys. Rev. Lett. **64** (1990) 2281.

[9] G. D. Severn, N. Hershkowitz, R. A. Breun, and J. R. Ferron, Phys. Fluids B **3** (1991) 114.

[10] O. Sakai, Y. Yasaka, and R. Itatani, Phys. Rev. Lett. **70** (1993) 4071.

[11] Y. Yasaka and R. Itatani, Phys. Rev. Lett. **56** (1986) 2811.

[12] J. R. Ferron, N. Hershkowitz, R. A. Breun, S. N. Golovato, and G. Goulding, Phys. Rev. Lett. **51** (1983) 1955.

[13] A. Fukuyama, A. Goto, S. -I. Itoh, K. Itoh, Jpn. J. Appl. Phys. **23** (1984) L613.

[14] Y. Yasaka, H. Takeno, A. Fukuyama, T. Toyoda, M. Miyakita, and R. Itatani, Phys. Fluids B **4** (1992) 1486.

[15] O. Sakai and Y Yasaka, Phys. Plasmas **1** (1994) 3896. T.Hirayama,

[16] I. D. Latimer, J. I. Mills, and R. A. Day, J. Quant. Spectros. Radiat. Transfer. **10** (1970) 629.

[17] R. H. Cohen, I. B. Bernstein, J. J. Dorning, and G. Rowlands, Nucl. Fusion **20** (1980) 1421.

[18] H. Hojo, T. Hatori, and S. Miyoshi, J. Phys. Soc. Jpn., **59** (1990) 789, H. Hojo, J. Phys. Soc. Jpn., **62** (1993) 4148.

[19] M. Ono, Phys. Rev. Lett. **42** (1979) 1267.

[20] W. A. Newcomb, J. Plasma Phys. **26** (1981) 529.

[21] H. Hojo, M. Inutake, M. Ichimura, R. Katanuma, and T. Watanabe, Jpn. J. Appl. Phys. **32** (1993) 2116.

Chapter 6

Conclusion

This study on tandem mirror plasmas controlled by ICRF waves and DC fields is summarized in the following conclusion.

Theoretical background of this study has been reviewed in Chap. 2. In Sec. 2.2, starting from the dispersion relation on ICRF waves, various resonance and mode conversion features have been derived for the configuration of a mirror device, where axial inhomogeneity is a key issue. In the regime of the helicon wave propagation, it contributes to efficient plasma production. Two mode conversions occur in a two-ion-species in the range of the fast wave propagation near the ion-ion hybrid resonance layer. Mode conversion into the slow wave gives rise to the ion heating, and that into the electrostatic mode contributes to electron heating. In Sec. 2.3, confinement in a mirror device has been discussed. Axial confinement of a tandem mirror strongly depends on the axial potential formation, as mentioned in Subsec. 2.3.1, and electron heating discussed in Sec. 2.2 can be beneficial on the ion-confining potential formation in the plug cell. Radial confinement properties related to magnetohydrodynamic stability has been described in Subsec. 2.3.2, and it is shown that stabilization by ICRF waves is effective against the flute mode instability, which is inherent in a mirror device. That is, ICRF waves can play various roles

to control a tandem mirror plasma. Radial confinement determined by anomalous transport is an important issue in general magnetic confinement systems, and possibility for improvement of radial confinement related to tokamak H mode, which is characterized by bifurcated states of edge plasma and edge localized sheared rotation, has been mentioned in Subsec. 2.3.3. Bifurcation phenomenon can be explained by the transport equation with the effect of shear stabilization. That is, improvement of radial confinement via L-H transition mainly observed in tokamaks is possible in all the magnetic confinement devices in which radial confinement is degraded by edge turbulence.

One of the promising features of the ICRF waves is resonance with ions and electrons, and ion heating in the central cell and electron heating in the plug cell are indispensable points for ignition in a mirror device. The experimental results shown in Chap. 3 have represented skillful method which realizes such situations simultaneously using only one ICRF wave. If the fast magnetosonic wave is excited in the midplane of the central cell and the minority cyclotron and ion-ion hybrid resonance layers are located in the region with gradient of the magnetic field strength in both cells, then the fast wave converts into the slow ion-cyclotron wave in the central cell and into the electrostatic wave in the plug cell. The wave dispersion relation derived in the experiment with the new measurement technique (described in Sec. 3.3) is in good agreement with the one-dimensional and two-dimensional theoretical analysis, and it is verified that the ion-ion hybrid resonance layer plays the essential roles on both mode conversions. Consequently such mode-converted waves contribute to ion heating or electron heating in each cell. That is, two mode conversions are completely discrete, and selective heating of ion or electron in each cell is controllable. The empirical scaling law of the ion heating quality factor shows no degradation of that factor in the parameter range of the experiment, so that, for instance, input ICRF power with 10 MW will produce a plasma with $n_e \times T_i = 10^{15}$ cm^{-3}keV,

which is close to ignition condition of a D-T reactor. If the scale of a machine is enlarged and energy confinement is enhanced, required input power per volume will be reduced, and this heating method can contribute to a future mirror reactor.

Improvement of radial confinement in a tandem mirror plasma has been investigated in Chap. 4. Using DC limiter biasing, *H*-mode-like discharge via hard transition has been observed, for the first time, in a mirror device. Transition features are similar to those in tokamaks; atomic line emission drops, density and stored energy in the bulk rise, density in the SOL decreases, edge turbulence is reduced, and edge-localized plasma rotation is induced. Enhancement factor of the global particle confinement is estimated to be $\sim$ 2.5. This is explained with effect of shear stabilization. That is, DC biasing induces edge plasma rotation through localized $\boldsymbol{E} \times \boldsymbol{B}$ drift, and edge turbulence quenches, resulting in decrease of fluctuation-induced transport and good radial confinement. The new experimental result throughout magnetic confinement systems is the clear observation of bifurcated states of edge confinement. When bias voltage is increased or decreased in one discharge, edge plasma parameters change along the different paths with hysteresis. Such a strong nonlinear feature in radial transport is predicted by several theories for tokamak geometry, and this experimental result suggests that radial transport in a mirror includes similar characteristics to tokamaks and stellarators. One simple model has been proposed, which is based on transport equation with the effect of shear stabilization.

Enhancement of axial confinement has been examined using ICRF waves, and the experimental results have been demonstrated in Chap. 5. The mode conversion into the electrostatic wave, described in Chap. 3, has been utilized for formation of ion-confining potential. The potential hill in the plug cell which can confine ions in the central cell has been created, and ion end loss flux is significantly reduced. Axial particle confinement is enhanced by a factor of $\sim$ 4. The importance of the mode conversion has

been emphasized with the change of electron temperature in the plug cell and with axial confinement factor due to presence of the ion-ion hybrid resonance layer. The propagating wave resulting from the mode conversion in the vicinity of the ion-ion hybrid resonance layer is considered to be the cold electrostatic ion-cyclotron wave, and axial electric field of the wave would accelerate plug cell electrons via Landau damping. The experimental results on the ion-confining potential and electron temperature is in good agreement with the theoretical scaling law with the RF-induced velocity space diffusion rather than that from the modified Boltzmann relation. The extension of this scaling law predicts that the ion-confining potential of 10 kV is created with the electron temperature in the plug cell several keV

Complete operation of an ICRF tandem mirror produces a high-beta and stable plasma, as shown in Chap. 5. Plasma is produced with the helicon wave, axially confined with the mode-converted ICRF wave (the electrostatic wave), radially confined with DC biasing, heated with the mode-converted ICRF wave (the slow wave), and stabilized with RF ponderomotive force. Such methods of control of a plasma are simultaneously applied, and no degradation coming from their combination has been observed. The beta value in the central cell reaches 14 %, and the global energy confinement time is increased by a factor of $\sim$ 4, where both the axial and radial confinement are enhanced by a factor of $\sim$ 4 with a controlled two-dimensional potential profile. Such a high beta plasma is sustained magnetohydrodynamically by the RF ponderomotive force, which is confirmed using two-dimensional ICRF code. This experimental result has verified the operation of the ICRF tandem mirror, which will be one candidate of tandem mirror configuration for a neutron source and a future reactor.

Acknowledgements

I would like to acknowledge sincerely all the people listed below who are remarkable for establishment of this work.

First, I would like thank Professor R. Itatani at Niihama College of Technology for encouraging me to be engaged in this work. His profound advises and vision for my study were very appreciated.

I would like to express my highest gratitude to Assistant Professor Y. Yasaka at Kyoto University, who have conducted me to do this continuous work from the beginning to the end. His advises to the details were indispensable to this achievement.

I also thank Professors I. Kimura, T. Obiki, H. Matumoto, and K. Yoshikawa at Kyoto University for their comments for finishing this study. Especially the continuous support by Professor I. Kimura was quite helpful.

I am very grateful to Dr. A. Fukuyama at Okayama University for supply of the 2-dimensional ICRF code for mirror geometry. That code gave meaningful theoretical analysis on propagation of the ICRF waves.

I wish to express my gratitude to Dr. G. M. Staebler at General Atomics and Dr. K. Itoh at National Institute for Fusion Science for discussions on the analysis of the high radial confinement mode. The model of shear stabilization by Dr. G. M. Staebler and the analysis dealing with mirror geometry by Dr. K. Itoh were very suggestive to construction

of the model for the transition phenomenon in HIEI.

I also wish to express my gratitude to the members of the GAMMA 10 group at University of Tsukuba, especially Professor T. Tamano, Professor K. Yatsu, Dr. Y. Kiwamoto, Dr. T. Saito, Dr. H. Hojo, Dr. T. Cho, Dr. A. Mase, Dr. M. Ichimura, and Dr. N. Yamaguchi. A great number of discussions with Professor T. Tamano are meaningful to my study, and their contributions to collaborative presentation in the 15th International Conference on Plasma Physics and Controlled Nuclear Fusion Research (IAEA, Sevilla, 1994) and their hospitality during my stay at University of Tsukuba were highly appreciated.

I thank Professor N. Sato, Dr. R. Hatakeyama, Professor M. Inutake at Tohoku University, Dr. H. Zushi at Kyoto University, and Dr. S. Okada at Osaka University for their meaningful discussions and their encouragement for me.

I wish to acknowledge Professor K. Tachibana, Dr. M. Kubo, Dr. I. Takahashi, Dr. H. Takeno (present address : at Kobe University), Dr. A. Hatta (present address : at Osaka University), Mr. M. Shima, Dr. M. Jinno (present address : at Ehime University), Mr. H. Yoshida, Mr. K. Iwami, and Mr. Y. Ohe at Kyoto University for their advises and their practical support for my operation of experiments and my theoretical analysis.

Finally, I would express my gratitude to Dr. K. Tomita, Dr. Y. Yamamoto, Dr. H. Taniguchi, and Dr. K. Nomoto at Sharp Corporation for their encouragement of my finishing this study.